COMPUTATIONAL SIMULATIONS OF ULTRAVIOLET RADIATION PENETRATION INTO HUMAN SKIN

Isla Rose Mary Barnard

A Thesis Submitted for the Degree of PhD
at the
University of St Andrews

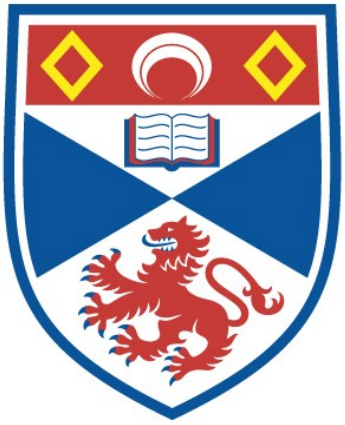

2021

Computational simulations of ultraviolet radiation penetration into human skin

Isla Rose Mary Barnard

University of
St Andrews

FOUNDED
1413

This thesis is submitted in partial fulfilment for the degree
of Doctor of Philosophy (PhD)
at the University of St Andrews

December 2020

Declarations

Candidate's declaration

I, Isla Rose Mary Barnard, do hereby certify that this thesis, submitted for the degree of PhD, which is approximately 30,000 words in length, has been written by me, and that it is the record of work carried out by me, or principally by myself in collaboration with others as acknowledged, and that it has not been submitted in any previous application for any degree. I confirm that any appendices included in my thesis contain only material permitted by the 'Assessment of Postgraduate Research Students' policy. I was admitted as a research student at the University of St Andrews in September 2016. I received funding from an organisation or institution and have acknowledged the funder(s) in the full text of my thesis.

Date 03/11/2021 Signature of candidate

Supervisor's declaration

I hereby certify that the candidate has fulfilled the conditions of the Resolution and Regulations appropriate for the degree of PhD in the University of St Andrews and that the candidate is qualified to submit this thesis in application for that degree. I confirm that any appendices included in the thesis contain only material permitted by the 'Assessment of Postgraduate Research Students' policy.

Date Signature of supervisor

Date 03/11/2021 Signature of supervisor

Permission for Publication

In submitting this thesis to the University of St Andrews we understand that we are giving permission for it to be made available for use in accordance with the regulations of the University Library for the time being in force, subject to any copyright vested in the work not being affected thereby. We also understand, unless exempt by an award of an embargo as requested below, that the title and the abstract will be published, and that a copy of the work may be made and supplied to any bona fide library or research worker, that this thesis will be electronically accessible for personal or research use and that the library has the right to migrate this thesis into new electronic forms as required to ensure continued access to the thesis. I, Isla Rose Mary Barnard, confirm that my thesis does not contain any third-party material that requires copyright clearance. The following is an agreed request by candidate and supervisor regarding the publication of this thesis:

Printed Copy

No embargo on print copy.

Electronic Copy

No embargo on electronic copy.

Date 03/11/2021 Signature of candidate

Date Signature of supervisor

Date 03/11/2021 Signature of supervisor

Underpinning Research Data or Digital Outputs

Candidate's declaration

I, Isla Rose Mary Barnard, understand that by declaring that I have original research data or digital outputs, I should make every effort in meeting the University's and research funders' requirements on the deposit and sharing of research data or research digital outputs.

Date 03/11/2021 Signature of candidate

Permission for publication of underpinning research data or digital outputs

We understand that for any original research data or digital outputs which are deposited, we are giving permission for them to be made available for use in accordance with the requirements of the University and research funders, for the time being in force. We also understand that the title and the description will be published, and that the underpinning research data or digital outputs will be electronically accessible for use in accordance with the license specified at the point of deposit, unless exempt by award of an embargo as requested below. The following is an agreed request by candidate and supervisor regarding the publication of underpinning research data or digital outputs: No embargo on underpinning research data or digital outputs.

Date 03/11/2021 Signature of candidate

Date Signature of supervisor

Date 03/11/2021 Signature of supervisor

Funding

This work was supported by an UK EPRSC PhD studentship [EP/N509759/1] and Medi-Lase, the Medical Laser Research Fund (Registered Charity SC037390).

Research Data/Digital Outputs access statement

Research data underpinning this thesis are available at:
https://doi.org/10.17630/b379c3f3-cc1c-497b-bd28-6c7dc0cc209d
Research code underpinning this thesis is available at:
https://doi.org/10.5281/zenodo.5651209

Publications and Presentations

Publications

- *Quantifying direct DNA damage in the basal layer of skin exposed to UV radiation from sunbeds*, **I R M Barnard**, P Tierney, C L Campbell, L McMillan, H Moseley, E Eadie, C T A Brown, and K Wood. *Photochemistry and photobiology 94(5), 2018*

- *Could psoralen plus ultraviolet A1 ('PUVA 1') work? Depth penetration achieved by phototherapy lamps*, **I R M Barnard**, E Eadie, L McMillan, H Moseley, C T A Brown, K Wood and R Dawe. *British Journal of Dermatology, 182(3), 2020*

- *Development of a Predictive Monte Carlo Radiative Transfer Model for Ablative Fractional Skin Lasers*, L McMillan, P O'Mahoney, K Feng, K Zheng, **I R M Barnard**, C Li, S Ibbotson, E Eadie, C T A Brown, and K Wood. *Lasers in Surgery and Medicine (Accepted, Early View), 2020*

- *Further evidence that far-UVC for disinfection is unlikely to cause erythema or premutagenic DNA lesions in skin*, **I R M Barnard**, E Eadie, and K Wood. *Photodermatology, Photoimmunology & Photomedicine (2020)*

- *Extreme exposure to filtered far-UVC: a case study*, E Eadie, **I R M Barnard**, S Ibbotsen and K Wood, *Photochemistry and Photobiology (submitted, special issue research article)*

- *φMC, a phase-tracking algorithm for Monte Carlo radiation transfer codes to model light propagation and interference in a turbid media*, L McMillan, S Reidt, C McNicol, **I R M Barnard**, C T A Brown, M P Macdonald and K Wood. *Biomedical Optics Express (in prep)*

Prizes and Awards

- The Arthur Maitland Prize, School of Physics & Astronomy, University of St Andrews (2018)
- The PDT Prize, British Medical Laser Association (BMLA) Conference (2017)

Conferences & Presentations

- *Simulating DNA damage in the basal layer of skin*, British Medical Laser Association (BMLA) Annual Conference, Manchester, UK, 2017
- *MCRT in medical physics (II)*, St Andrews Monte Carlo Summer School (invited speaker), St Andrews, UK, 2017
- *Ultraviolet radiation, DNA damage and Sunscreen*, Laser Europe (invited speaker), Rotterdam, NL, 2018
- *Psoriasis Treatment: Can we go deeper? The emerging role a simulation in clinical phototherapy practice*, International Conference on Biophotonics (invited speaker), St Andrews, UK, 2019
- Poster: *Phototherapy: spectrally and spatially resolved depth penetration achieved by phototherapy lamps*, International Conference on Biophotonics, St Andrews, UK, 2019
- *Performance of handheld light meter for measuring erythemally effective UVR output from sunbeds*, British Medical Laser Association (BMLA) Annual Conference, London, UK, 2019
- *In silico simulation of the effect of sunscreen on direct DNA damage in different skin types*, Light & Life- 17^{th} International Congress of Photobiology, 18^{th} Congress of the European Society for Photobiology (contributed oral communication), Barcelona 2019

Courses Attended

- Hands on intro to HPC and Message-passing programming with MPI, Edinburgh 2018
- Software Carpentry Instructors Course, UK, 2018
- Photobiology Journal Club (weekly, Photobiology Unit, Ninewells Hospital & Medical School, Dundee
- Digital Health Seminar (monthly, University of St Andrews)

Abstract

This thesis concerns the development of numerical modelling simulations to predict how ultraviolet radiation (UVR) penetrates into human skin in a wavelength dependent manner. UVR has biological effects; for example, UVR causes damage to DNA within skin cells, and these effects are wavelength dependent. A Monte Carlo Radiative Transfer (MCRT) model was developed in order to simulate the transport of UVR from different radiation sources through the upper layers of human skin. Using the results of these simulations, the depth to which different wavelengths of UVR penetrate can be examined, and then resulting biological effects can be predicted.

The research presented here quantifies DNA damage occurring due to sunbed use, investigates the protective effects of melanin and sunscreen, investigates potential novel lamps for psoriasis treatment and examines the safety of UVR sterilisation devices. In addition, research is presented from practical work, evaluating the performance of a handheld UVR meter when used to measure UVR output from commercial sunbeds.

Acknowledgements

When I started this PhD in 2016, I had no idea how many people would help me along the way. I'm now going to try to thank everyone, knowing these are those I have forgotten.

A profound thank you to Tom, Kenny, Ewan and Harry. I owe you all an unrepayable debt for your supervision and guidance over this PhD and through my time at St Andrews.

Thank you to Lewis for being a mentor and companion from the start through to the end of this journey.

Thanks to our extended MCRT family including Tim, Freddy, Laura, Louise, Louise, Patrick and Ronan (and hopefully more to come!).

A special thanks to my examiners Janet & Antony for providing me with thoughtful and interesting feedback.

I'd like to thank staff and students at the school of Physics & Astronomy at the University of St Andrews. In no particular order, and with apologies to anyone I miss, thanks to Poppy Nicholson, Cameron Rae, Aly Gillies, Michael Mazilu, Bruce Sinclair, Ian Bonnell, Jonathan Keeling, Lesley Aitken, Dimali Vithanage, Paul Donaldson, Sebastian Schultz, Brendon Lovett, Kristin Lund, Paul Cruickshank, Natalia Korolkova, Keith Horne, Tom Edwards, Jonny Terry, Ian Taylor, Duncan Robertson, Marcel Schubert, Malte Gather, Vivienne Wild, Janet Lovett, Irina Leonhardt, Rita Tojero, Anne-Marie Weijmans, Fran Bartolic, Hongsheng Zhao, Peter Woitke, Christiane Helling, Fiona Bairstow, Antje Kohnle, Charlie Bailey, Chris Hooley, Vicky, Scott Johnston, Stephen King. In other schools at the University of St Andrews, I'd like to thank Silvia Paracchini, David Harris-Birtill, Alexander Konovalov and Patrick McCann for encouragement when I needed it most. I'd also like to thank everyone at Ninewells Photobiology Unit and Dermatology Department, with special thanks to Sally Ibbotson, Lynn Fullerton, Nicki Traynor, Robert Dawe, Vicky McGuire and Paul O'Mahoney.

I'd like to thank some amazing friends; I'm so lucky. Karys, Mary, Lucy, Vairi, Gabi, Yuchen, Thomas, Joel, David, Danny, Aedan, Scott, Gemma, David, Kaitlin, Oz and Annie. A huge thank you to Bob, Laureen and Phil Merriman for welcoming me into your family.

And lastly, thank you to my family. To my Dad, for supporting this dive into academia in my late 20s. To my Mum for always being there and keeping me grounded. Thanks always to Theo. And Pepi; you & Theo's beautiful music has powered me through many evenings. Now I have time to learn an instrument, so I can take my rightful place as the fourth member of the Barnard-Emmerichs-Merriman Family Band Solution.

Most of all, thank you to Callum. I did the work for myself, but I wrote this up for us. Let's never speak of it again. We don't have time to anyway, there's a house to build.

For Doff, Mary
and Maude.

All models are wrong, but some are useful

GEORGE BOX

Contents

List of Figures

List of Tables

List of Abbreviations

8-MOP 8-Methoxypsoralen.

BCC Basal cell carcinoma.

CDF Cumulative distribution function.

CPD Cyclobutane pyrimidine dimer.

DNA Deoxyribonucleic acid.

FWHM Full width at half maximum.

HCEH Highland Council Environmental Health.

NB-UVB Narrowband ultraviolet B.

PDF Probability density function.

PUVA Psoralen + Ultraviolet A.

PUVA1 Psoralen + Ultraviolet A1.

RTE Radiative transfer equation.

SCC Squamous cell carcinoma.

SSR Solar simulated radiation.

UV Ultraviolet.

UVA Ultraviolet A.

UVA1 Ultraviolet A1.

UVB Ultraviolet B.

UVC Ultraviolet C.

UVR Ultraviolet radiation.

Chapter 1

Introduction

Over-exposure to ultraviolet radiation (UVR) is a major cause of all types of skin cancer [1, 2, 3]. There are over 16,000 new cases of melanoma skin cancer, and over 150,000 new cases of keratinocyte skin cancers, diagnosed annually in the UK [4]. Skin cancer is caused by mutations in DNA, and these DNA mutations can be induced by UVR [3].

By quantifying the amount of potentially mutagenic radiation reaching into the skin, it is possible to quantify risks around exposure to different sources of UVR (such as sunbathing and sunbed use). This information can be used to communicate risks to the public, and to aid development of strategies for prevention by understanding of the formation of skin cancers [5].

However, *in vivo* experiments to quantify mutagenic radiation reaching into skin tissue can be harmful to an individual, and difficult to perform. For example, trials involving humans or animals require subjects to be exposed to UVR, and invasive biopsies may be taken. Clinical trials are expensive and labour intensive, and ethical considerations necessitate strict definition of the scope of experiments at the outset. All of these issues also apply to *in vivo* experiments involving animals.

One solution is to use computational simulations of radiation transfer to quantify the amount of UVR penetrating into the skin. Computational simulations allow a wide variety of scenarios to be explored without the practical barriers of fulfilling ethical considerations associated with experiments on people or animals. Once the code has been written, simulations can be designed quickly. The time taken to perform simulations and gather initial results can be under an hour. The scope of the simulations that can be performed is only limited by computation time and available input data. If simulation results require further investigation, parameters can be altered and results examined quickly without the need to formally approve alterations to experimental procedure.

This thesis describes the application of Monte Carlo Radiative Transfer algorithm to simulate the transfer of UVR through the upper layers of the skin. This will rely on simulating interactions between UVR and skin tissue, such as scattering (e.g., by keratin in the stratum corneum, for example) and absorption (e.g., by melanin or DNA). The resulting data on the transmission of UVR, used in conjunction with existing data from *in vitro* experimental work, allows photobiological processes within the skin to be simulated. Comparison against existing *in vivo* results provides a method of validating results produced via simulation. The codes and approach used were initially developed for astrophysical simulations of radiation transfer through galactic dust and gas [6], and have been adapted for use in simulating radiation transfer through skin tissue [7, 8].

1.1 The skin

The skin is the largest organ in the human body, with an average surface area of $2\,m^2$ [9]. The outermost layer of the skin is called the epidermis, and provides the first line of defence against environmental stressors such as pathogens, friction and UVR. The epidermis also protects against moisture and nutrient loss. The epidermis is subdivided into layers, and constituent cells are illustrated in Figure 1.1.

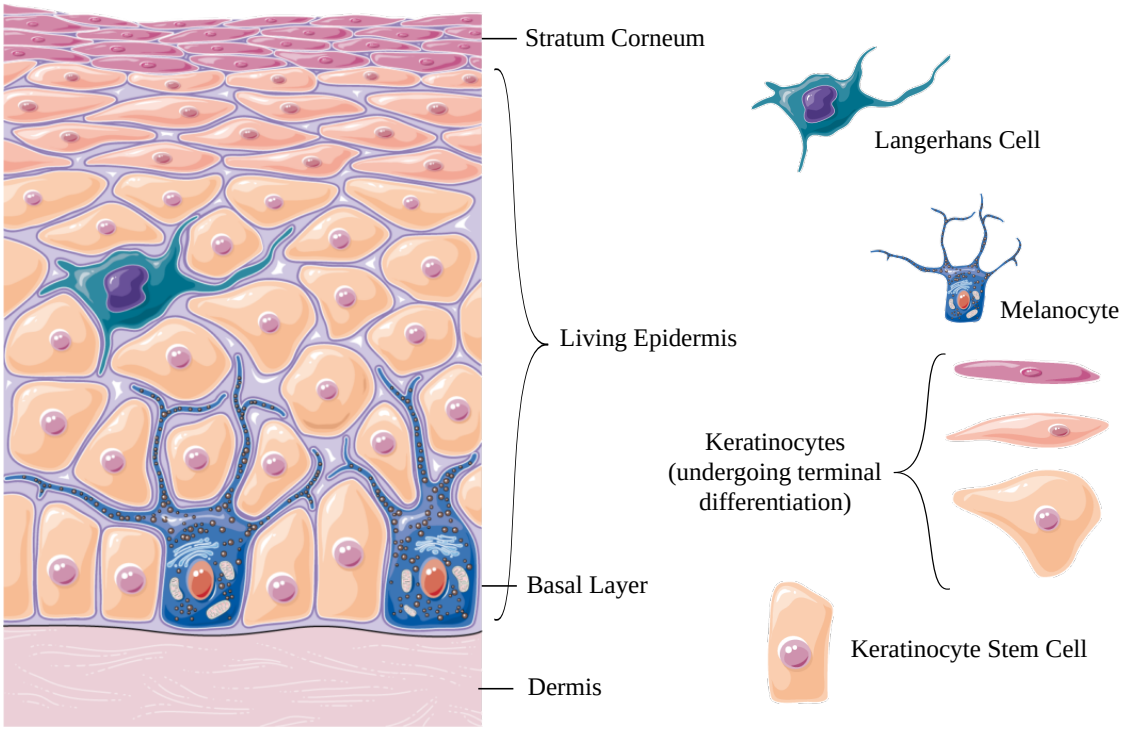

Figure 1.1: *An illustration of the cellular constituents of the epidermis, showing the the top layer (stratum corneum), the living epidermis (containing the bulk of the keratinocytes), and the basal layer (the keratinocyte stem cell layer) where new keratinocytes are produced. The living epidermis is further stratified into the stratum lucidium, stratum granulosum, and stratum spinosum. These layers are visible in the image, as the epidermis is illustrated by layers of keratinocytes at different stages of flattening. This figure was created using images from Servier Medical Art (http://smart.servier.com), which are licensed under a Creative Commons 3.0 Unported License.*

As Figure 1.1 shows, the majority of cells in the epidermis are keratinocytes. Keratinocyte stem cells are located in the basal layer. Here, new keratinocytes are produced. Occasionally a new stem cell will be produced (which remains in the basal layer) but most new keratinocytes leave the basal layer and move towards the surface, becoming part of the living epidermis. There, the cell undergoes changes (these are illustrated Figure 1.1), becoming keratinised and more tightly packed against its neighbours, in a process known as terminal differentiation. Eventually the cells become completely keratinised and die, locking together to form the protective stratum corneum at the surface of the skin. In healthy skin, dead cells from the surface of the stratum corneum are continuously shed at the same rate that the cells arrive at the base of the stratum corneum. Cells produced by the basal layer reach the base of the stratum corneum in about 14 days, and shed after about 50 days

[10], though this takes longer with increased age [11]. Below the basal layer is the dermis, which is primarily a layer of irregular connective tissue, interspersed by capillaries (blood vessels with a wall one cell thick).

In addition to keratinocytes, Figure 1.1 shows Langerhans cells, which are part of the immune system, and melanocytes, which both produce the skin pigment melanin, and distribute melanin to surrounding keratinocytes.

1.2 Biological effects of UVR on skin

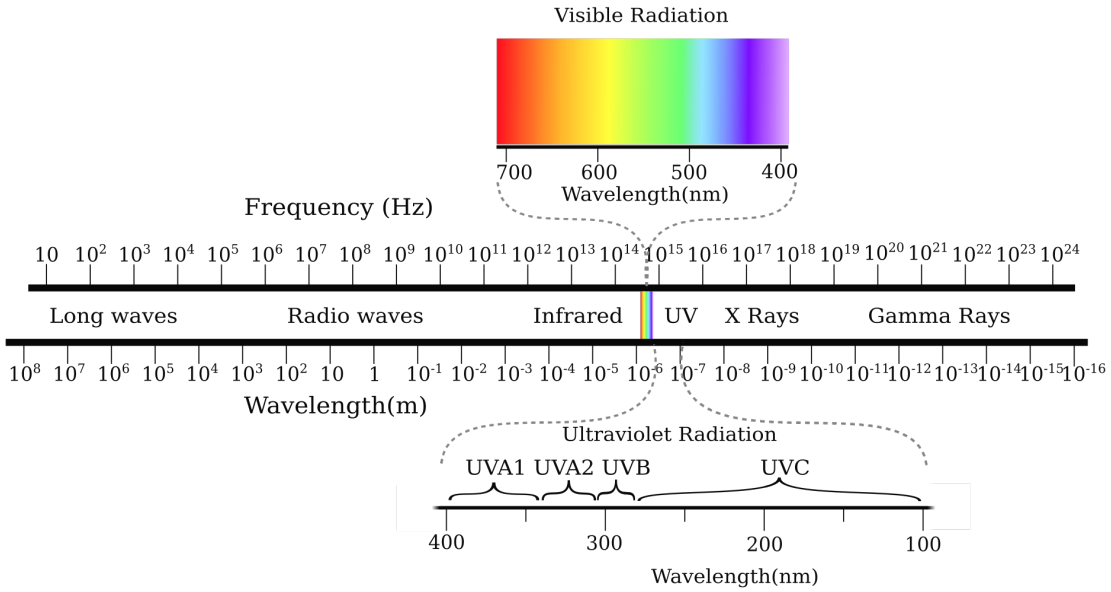

Figure 1.2: *UVR in the context of the of electromagnetic spectrum.*

UVR describes a band of radiation, comprised of radiation with wavelengths between 100 nm and 400 nm. Figure 1.2 places UVR in the context of the electromagnetic spectrum and visible radiation. UVR is further classified into bands, named Ultraviolet A (UVA) from 315 nm to 400 nm, Ultraviolet B (UVB) from 280 nm to 315 nm, and also Ultraviolet C (UVC) from 100 nm to 280 nm. These bands are not absolutes, but are useful categorisations when describing different biological effects of UVR [12, 13].

Most human exposure to UVR is from terrestrial solar UVR, which comprises mostly UVA and a small amount of UVB (Figure 1.3). In addition to this, there are artificial sources of UVR, such as artificial tanning units (sunbeds), medical UVR units, and sterilisation devices. Ultraviolet sterilisation devices can be a source of UVC, which is not present within terrestrial solar radiation. Within this text, the terminology UVA, UVB and UVC refer strictly to wavelength bands, and not to sources.

In literature, a 'UVA source' may also emit a small yet biologically significant amount of UVB radiation, and a 'UVB source' may emit a small but significant amount of UVA radiation.

UVR can affect living things in several ways. In biology, a chromophore is defined as a molecule (or part of a molecule) that undergoes a structural change after absorbing energy from UVR or

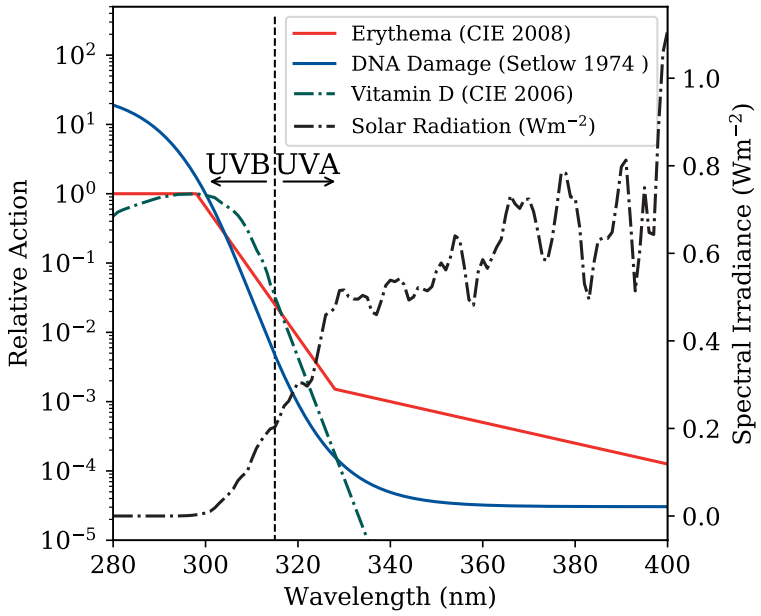

Figure 1.3: *Mediterranean midday, midsummer solar spectrum [14] in black (measured in Wm^{-2}), CIE (International Commission on Illumination) erythema action spectrum [15], normalised CIE vitamin D induction spectrum [16], and a generalised normalised DNA damage action spectrum [17], giving the wavelength dependent damage for DNA in vitro (not in skin). Action spectra describe the wavelength dependent efficiency of a radiation induced biological process. The image also shows the UVA and UVB bands.The action spectra of most biological effects of UVR with significant impact on human health peak in the UVB band; but there are significant effects into the UVA.*

visible light. This structural change may or may not be permanent. Examples of chromophores in human skin are DNA and melanin. Chromophore activation can have direct consequences, or could signal the start of physiological responses. For example, as a physiological response to UVR, melanocytes produce and distribute melanin.

1.2.1 DNA damage and photocarcinogenesis

DNA is a chromophore. Although photons in the UVR band do not carry enough energy to ionise atoms or molecules, UVR does contain enough energy to alter the structure of DNA [3]. Primary DNA damage occurs when energy imparted by a UV photon is absorbed by DNA, and directly alters the structure of the DNA molecule. Secondary DNA damage occurs when absorption of a UV photon generates reactive oxygen species (ROS), leading to a cascade of damage, including damage to DNA, as well as to the cell as a whole. Via these pathways, UVR is a known cause of keratinocyte skin cancers. Most epidermal keratinocytes have a short lifetime, and cannot accrue enough DNA damage to lead to cancer. The exception to these are the long lived stem cells in the basal layer, where new keratinocytes are produced. As such, the process of photocarcinogenesis necessarily relies upon the transfer of radiation from the surface of the skin to the basal layer. Figure 1.3 shows the generalised DNA action spectrum (normalised to 300 nm), indicating that DNA is most susceptible to damage from higher energy UVB radiation. However the skin itself filters UVR, meaning a proportion of this higher energy radiation is removed before it reaches the basal layer.

1.2.2 Skin Cancers

UVR exposure is a known cause of all types of skin cancer [1, 2, 3]. Melanoma skin cancers are the cause of most skin cancer deaths [1], and keratinocyte cancers do not usually display a systemically aggressive disease course. The keratinocyte skin cancers are squamous cell carcinoma (SCC) and basal cell carcinoma (BCC). Despite these being having a low mortality rate [1], they are extremely common, and treatment of these cancers represents a large financial burden for healthcare systems globally.

In fair skinned populations, skin cancer is, by far, the most common type of cancer [1]. In darker skinned populations, skin cancer is less common. This is due to the protective effects of skin pigmentation, in the form of melanin.

1.2.3 Erythema and skin types

Erythema describes reddening of the skin caused by increased blood flow in dermal capillaries. This is induced by injury or inflammation, and examples include wounds, insect bites, contact allergies, or irradiation with UVR. The extent to which UVR is able to induce erythema is wavelength dependent, with more energetic UVB causing more erythema than the longer wavelength UVA. The erythema action spectrum $E(\lambda)$ [15] (where wavelength λ is given in nm), is shown in Figure 1.3 and is described by,

$$E(\lambda) = \begin{cases} 1 & 250\,\text{nm} \leq \lambda < 298\,\text{nm} \\ 10^{0.094(298-\lambda)} & 298\,\text{nm} \leq \lambda < 328\,\text{nm} \\ 10^{0.015(140-\lambda)} & 328\,\text{nm} \leq \lambda < 400\,\text{nm} \end{cases} \tag{1.1}$$

DNA damage is thought to be the chromophore for erythema [5]. The skin's response to UVR depends on the melanin content of the skin, and the different responses are described by the Fitzpatrick skin type, detailed in Table 1.1.

Skin Phototype [18]	Features	Response to Sun Exposure
I	Pale white skin	Always burns, never tans
II	Fair skin	Burns often, tans poorly
III	Darker white/ olive skin	Average tanning (after initial burn)
IV	Light brown skin	Minimal burns, tans
V	Brown skin	Rarely burns, tans darkly easily
VI	Dark brown or black skin	Almost never burns

Table 1.1: *Fitzpatrick skin type classifications [18]. A lower skin type corresponds to a stronger reaction to UVR exposure, as the additional skin pigmentation present in higher skin types imparts protection.*

1.2.4 Benefits of UVR

Solar UVR does have some positive effects on human health, such as the production of vitamin D, and improved mood [19]. Recently evidence has emerged that UVR may have a beneficial effect on cardiovascular health by releasing nitric oxide (NO) [20]. NO generated by UVR may also positively affect the microbiome, and may and act as a neurotransmitter [21]. UVR also has immunosuppressive effects. These mechanisms can be harnessed to use UVR in a range of medical treatments, called phototherapy. UVC radiation is germicidal, and has widespread applications in sterilisation of air and surfaces [22], which is of great interest due to the current COVID-19 pandemic.

1.3 Radiation transfer

Skin photobiology involves radiation travelling into the skin, and the biological effects are due to chromophore absorption at some location within the skin. UVR travels through the skin in a wavelength dependent manner, and the biological effects of UVR absorption are also wavelength dependent.

To experimentally quantify biological effects of UVR *in vivo*, studies are labour, time, and cost intensive, and in addition are subject to strict ethical constraints.

Photochemical and photobiological processes can be investigated *in vitro* (for example, elucidating the DNA damage spectrum as shown in Figure 1.3). The resulting data cannot be automatically applied to *in vivo* processes, as *in vitro* procedures are unlikely to reproduce the transfer of UVR through the skin.

In silico simulations attempt to address these issues. By simulating the radiation transfer from almost any source into skin tissue, and quantifying resulting expected biological effects of the radiation transfer, all without direct harm to any experimental subject.

Quantifying the biological effects of UVR within the skin necessitates quantifying the transfer of UVR through the skin. It is proposed that if the UVR transfer through the skin can be simulated, then resulting biological effects could also be simulated.

In order to accurately simulate UVR propagation through a scattering medium such as skin tissue, the transfer of radiation through the skin must be represented by a suitable theoretical model.

1.3.1 The radiative transfer equation

The radiative transfer equation (the RTE) describes the propagation of radiation in any medium. The RTE can be derived by framing radiation transfer in terms of a particle-like description of radiation travelling through a collection of scatterers and absorbers. Interactions between a photon and the medium occur randomly, but the probability of interactions is specified. The RTE can be derived from energy conservation rules. Simplistically, this looks at losses and gains of the number of photons within a volume element ($\mathrm{d}V$). The following derivation is adapted from Quantitative Biomedical Optics by Bigio & Fantini [23].

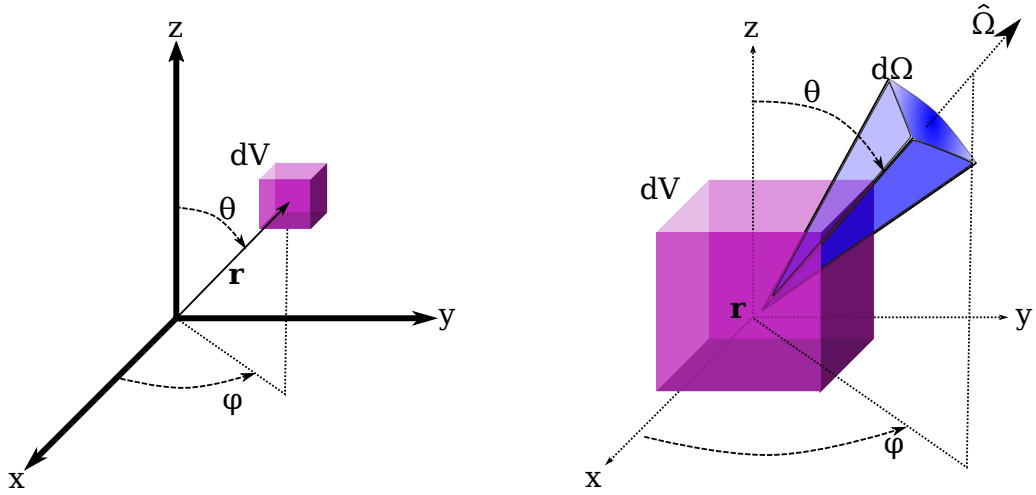

Figure 1.4: *The left image gives position of differential volume element* $\mathrm{d}V$ *in Cartesian and polar systems as referred to in the derivation of the radiative transfer equation (the RTE). The right image shows volume element* $\mathrm{d}V$ *at position* $\boldsymbol{r}$*, and the differential directional element* $\mathrm{d}\Omega$*.*

The energy conservation principles applied to the volume element $\mathrm{d}V$ can be thought of as the sum of the gains in photons within $\mathrm{d}V$ due to sources, the gains and losses due to scattering, the losses due to absorption, and the losses due to divergence of the photon beam. Consider the angular energy density $u(\boldsymbol{r}, \hat{\boldsymbol{\Omega}}, t)$. This is the energy per unit volume, per unit solid angle, travelling in direction $\hat{\boldsymbol{\Omega}}$ at position $\boldsymbol{r}$ at time t; and is measured in units of $\mathrm{Jm}^{-3}\mathrm{sr}^{-1}$. As Equation 1.2 shows, the angular energy density $u(\boldsymbol{r}, \hat{\boldsymbol{\Omega}}, t)$ (propagating about direction $\hat{\boldsymbol{\Omega}}$ at position $\boldsymbol{r}$ at time t) is directly proportional to the number of photons per unit volume and per unit solid angle that are

propagating about direction $\hat{\boldsymbol{\Omega}}$ at position $\boldsymbol{r}$ at time t),

$$N_{\mathrm{dV,t}} = \frac{u(\boldsymbol{r}, \hat{\boldsymbol{\Omega}}, t)\lambda_{\mathrm{n}}}{hc_{\mathrm{n}}} \tag{1.2}$$

where λ_{n} is the wavelength in a medium of refractive index n, and c_{n} the speed of light in a medium of refractive index n, and the individual photon energy is given by hc/λ.

Using energy conservation principles across the volume element $\mathrm{d}V$ (as shown in Figure 1.4); the total rate of change of angular energy density $u(\boldsymbol{r}, \hat{\boldsymbol{\Omega}}, t)$ is the sum of the losses due to divergence and extinction, and the gains due to any sources within the volume or scattering into the volume. This is made explicit in Equation 1.3,

$$\frac{\partial}{\partial t}u(\boldsymbol{r}, \hat{\boldsymbol{\Omega}}, t) = \frac{\partial}{\partial t}u(\boldsymbol{r}, \hat{\boldsymbol{\Omega}}, t)_{\mathrm{div}} + \frac{\partial}{\partial t}u(\boldsymbol{r}, \hat{\boldsymbol{\Omega}}, t)_{\mathrm{ext}} + \frac{\partial}{\partial t}u(\boldsymbol{r}, \hat{\boldsymbol{\Omega}}, t)_{\mathrm{scatt}} + \frac{\partial}{\partial t}u(\boldsymbol{r}, \hat{\boldsymbol{\Omega}}, t)_{\mathrm{src}} \tag{1.3}$$

The divergence term

The first term in Equation 1.3, $\frac{\partial}{\partial t}u(\boldsymbol{r}, \hat{\boldsymbol{\Omega}}, t)_{\mathrm{div}}$, describes loss (or gain) of photons in the volume element $\mathrm{d}V$ (at position $\boldsymbol{r}$, travelling in direction $\hat{\boldsymbol{\Omega}}$, at time t) due to divergence of the photon beam. This can be interpreted as the spatial rate of change of $u(\boldsymbol{r}, \hat{\boldsymbol{\Omega}}, t)$ in the direction $\hat{\boldsymbol{\Omega}}$; and can represent a rate of change with respect to time by multiplying by the speed of light c_{n} (the distance travelled by light in medium of refractive index n in an infinitesimal time $\mathrm{d}t$),

$$\frac{\partial}{\partial t}u(\boldsymbol{r}, \hat{\boldsymbol{\Omega}}, t)_{\mathrm{div}} = c_{\mathrm{n}}\hat{\boldsymbol{\Omega}} \cdot \nabla u(\vec{\boldsymbol{r}}, \hat{\boldsymbol{\Omega}}, t)_{\mathrm{div}} \tag{1.4}$$

The extinction term

The second term in Equation 1.3, $u(\boldsymbol{r}, \hat{\boldsymbol{\Omega}}, t)_{\mathrm{ext}}$, describes the loss of photons from volume element $\mathrm{d}V$ (at position $\boldsymbol{r}$, travelling in direction $\hat{\boldsymbol{\Omega}}$, at time t) due to either absorption, or from scattering out of the direction $\hat{\boldsymbol{\Omega}}$ (represented in Equation 1.5 by μ_{a}, the absorption coefficient, and μ_{s}, the scattering coefficient),

$$\frac{\partial}{\partial t}u(\boldsymbol{r}, \hat{\boldsymbol{\Omega}}, t)_{\mathrm{ext}} = c_{\mathrm{n}}(\mu_{\mathrm{a}} + \mu_{\mathrm{s}})u(\boldsymbol{r}, \hat{\boldsymbol{\Omega}}, t) \tag{1.5}$$

These losses are illustrated in Figure 1.5. The speed of light in a medium of refractive index n is c_{n}, and can also be thought of as the distance travelled by a photon per unit time. Thus $c_{\mathrm{n}}(\mu_{\mathrm{a}} + \mu_{\mathrm{s}})u(\boldsymbol{r}, \hat{\boldsymbol{\Omega}}, t)/hf$ (see Equation 1.2) gives the number of photons per solid angle $\mathrm{d}\Omega$ in volume element $\mathrm{d}V$ that are absorbed or scattered, per unit time. As the distance light travels in time $\mathrm{d}t$ is given as $c_{\mathrm{n}}\mathrm{d}t$; then the quantities μ_{a} and μ_{s} can be interpreted as probabilities of absorption or scattering over the infinitesimal distance $c_{\mathrm{n}}\mathrm{d}t$. The sum $\mu_{\mathrm{a}} + \mu_{\mathrm{s}}$ can be interpreted as the probability of interaction, and is often denoted $\mu_{\mathrm{t}} = \mu_{\mathrm{a}} + \mu_{\mathrm{s}}$,

$$\frac{\partial}{\partial t}u(\boldsymbol{r}, \hat{\boldsymbol{\Omega}}, t)_{\mathrm{ext}} = c_{\mathrm{n}}\mu_{\mathrm{t}}u(\boldsymbol{r}, \hat{\boldsymbol{\Omega}}, t) \tag{1.6}$$

This treatment of μ_{a} and μ_{s} as mutually exclusive probabilities of interaction is a vital part of the Monte Carlo Radiative Transfer method, and Chapter 2 details the application of this concept to the simulation of skin optics.

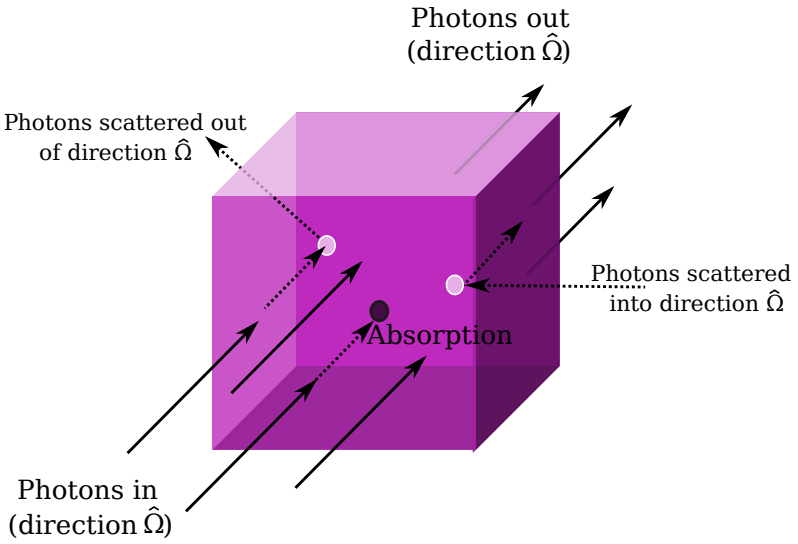

Figure 1.5: *This image indicates losses and gains within the volume element* $\mathrm{d}V$ *by showing the effects of absorption and scattering within the volume element* $\mathrm{d}V$*. For clarity the figure shows the photons scattered into direction* $\hat{\boldsymbol{\Omega}}$ *as originating outside volume element* $\mathrm{d}V$ *(and the photons scattered out of direction* $\hat{\boldsymbol{\Omega}}$ *as ending up outside volume element* $\mathrm{d}V$*). However photons remaining within volume element* $\mathrm{d}V$ *that have also changed direction are counted as a loss or gain.*

The scattering term

The third term in Equation 1.3, $u(\boldsymbol{r}, \hat{\boldsymbol{\Omega}}, t)_{\mathrm{scatt}}$, is the scattering term. This represents the gain of photons in volume element $\mathrm{d}V$ (at time t) that have been scattered at $\boldsymbol{r}$ into direction $\hat{\boldsymbol{\Omega}}$ from any direction $\hat{\boldsymbol{\Omega}}'$ other than $\hat{\boldsymbol{\Omega}}$,

$$\frac{\partial}{\partial t} u(\boldsymbol{r}, \hat{\boldsymbol{\Omega}}, t)_{\mathrm{scatt}} = c_{\mathrm{n}} \mu_{\mathrm{s}} \int_{4\pi} u(\boldsymbol{r}, \hat{\boldsymbol{\Omega}}, t) P(\hat{\boldsymbol{\Omega}}', \hat{\boldsymbol{\Omega}}) \mathrm{d}\hat{\Omega}' \tag{1.7}$$

The integral in Equation 1.7 is over the whole solid angle $\int_{4\pi} \mathrm{d}\hat{\Omega}'$; so as to include the gain of photons from scattering from any direction. The scattering coefficient μ_{s} is the probability that over infinitesimal distance $c_{\mathrm{n}}\mathrm{d}t$, a scattering event will take place. In addition there is another term, $P(\hat{\boldsymbol{\Omega}}', \hat{\boldsymbol{\Omega}})$, known as the scattering phase function. $P(\hat{\boldsymbol{\Omega}}', \hat{\boldsymbol{\Omega}})$ is a function that describes the probability of a photon travelling in direction $\hat{\boldsymbol{\Omega}}'$ being scattered into direction $\hat{\boldsymbol{\Omega}}$. The gains of photons across volume element $\mathrm{d}V$ are illustrated in Figure 1.5.

The source term

The fourth term in Equation 1.3, $u(\boldsymbol{r}, \hat{\boldsymbol{\Omega}}, t)_{\mathrm{src}}$, represents the gain of photons (at position $\boldsymbol{r}$, travelling in direction $\hat{\boldsymbol{\Omega}}$, at time t) due to any photon sources present in the volume $\mathrm{d}V$. Equation 1.8 represents this in terms of $q(\boldsymbol{r}, \hat{\boldsymbol{\Omega}}, t)_{\mathrm{src}}$, which is the energy radiated by a source per unit time, per unit solid angle, per unit volume (at position $\boldsymbol{r}$, travelling in direction $\hat{\boldsymbol{\Omega}}$, at time t).

$$\frac{\partial}{\partial t} u(\vec{\boldsymbol{r}}, \hat{\boldsymbol{\Omega}}, t)_{\mathrm{src}} = q(\vec{\boldsymbol{r}}, \hat{\boldsymbol{\Omega}}, t)_{\mathrm{src}} \tag{1.8}$$

Sources can include primary radiation sources (e.g., a point source radiating), or secondary sources (e.g. emission following absorption at a point in space).

The RTE

The constituent parts can be inserted into Equation 1.3 to yield,

$$\frac{\partial}{\partial t}u(\boldsymbol{r},\hat{\boldsymbol{\Omega}},t) = c_{\mathrm{n}}\hat{\boldsymbol{\Omega}}\cdot\nabla u(\boldsymbol{r},\hat{\boldsymbol{\Omega}},t)_{\mathrm{div}} + c_{\mathrm{n}}\mu_{\mathrm{t}}(\boldsymbol{r},\hat{\boldsymbol{\Omega}},t) + c_{\mathrm{n}}\mu_{\mathrm{s}}\int_{4\pi} u(\boldsymbol{r},\hat{\boldsymbol{\Omega}},t)P(\hat{\boldsymbol{\Omega}}',\hat{\boldsymbol{\Omega}})\mathrm{d}\hat{\Omega}' + q(\boldsymbol{r},\hat{\boldsymbol{\Omega}},t) \quad (1.9)$$

Equation 1.9 was derived using the concept that the energy in a volume element $\mathrm{d}V$was directly proportional to the number of photons contained within that volume (see Equation 1.2). Losses and gains of photons within a volume is relatively easy to quantify. However the more recognisable form of the RTE recasts Equation 1.9 in terms of radiance $L(\boldsymbol{r},\hat{\boldsymbol{\Omega}},t)$, which is the radiant angular intensity per unit area travelling in direction $\hat{\boldsymbol{\Omega}}$, at position $\boldsymbol{r}$ at time t. The radiance $L(\boldsymbol{r},\hat{\boldsymbol{\Omega}},t)$ has SI units of $\mathrm{Wm}^{-2}\mathrm{sr}^{-1}$. The radiance is directly proportional to the energy, as shown by Equation 1.10.

$$u(\boldsymbol{r},\hat{\boldsymbol{\Omega}},t) = \frac{L(\boldsymbol{r},\hat{\boldsymbol{\Omega}},t)}{c_{\mathrm{n}}} \quad (1.10)$$

Substituting Equation 1.10 into into Equation 1.9 yields the more familiar form of the RTE,

$$\frac{1}{c_{\mathrm{n}}}\frac{\partial}{\partial t}L(\boldsymbol{r},\hat{\boldsymbol{\Omega}},t) = \hat{\boldsymbol{\Omega}}\cdot\nabla L(\boldsymbol{r},\hat{\boldsymbol{\Omega}},t) + \mu_t L(\boldsymbol{r},\hat{\boldsymbol{\Omega}},t) + \mu_s\int_{4\pi} L(\boldsymbol{r},\hat{\boldsymbol{\Omega}},t)P(\hat{\boldsymbol{\Omega}}',\hat{\boldsymbol{\Omega}})\mathrm{d}\hat{\Omega}' + q(\boldsymbol{r},\hat{\boldsymbol{\Omega}},t) \quad (1.11)$$

The radiance $L(\boldsymbol{r},\hat{\boldsymbol{\Omega}},t)$ can also be thought of as representing the number of photons travelling in direction $\hat{\boldsymbol{\Omega}}$, at position $\boldsymbol{r}$ at time t, passing through a differential surface element $\mathrm{d}S$,

$$N_{\mathrm{dS,t}} = \frac{L(\boldsymbol{r},\hat{\boldsymbol{\Omega}},t)}{hf} \quad (1.12)$$

The radiance yields quantities useful in photobiology, such as the fluence rate (the energy delivered by radiation per unit time, per unit area from any direction),

$$\Phi(\boldsymbol{r},t) = \int_{4\pi} L(\boldsymbol{r},\hat{\boldsymbol{\Omega}},t)\mathrm{d}\Omega \quad (1.13)$$

Where $\Phi(\boldsymbol{r},t)$ is measured in Wm^{-2}.

1.3.2 Approximate solutions to the RTE

Even for simple media, solving the RTE analytically is difficult. For a complex structure such as the skin, given gradients in absorption and scattering properties, calculation of an exact analytic solution to the RTE is currently effectively impossible. Given the importance of elucidating radiation transfer through skin tissue, several methods exist as approximate solutions to the RTE. The most straightforward approximations will assume either scattering or absorption dominates within the system.

The Diffusion Approximation

If scattering dominates within a system, the diffusion approximation can be used. This involves expanding the radiance in the RTE in terms of spherical harmonics [23]. This approach is more valid for isotropic scattering (where the factor $P(\hat{\mathbf{\Omega}}', \hat{\mathbf{\Omega}})$ is the same for all $\hat{\mathbf{\Omega}}'$). This approximation can have merit in tissue where scattering could be approximated as isotropic. However the upper layers of the skin is highly forward scattering, so the diffusion approximation is not suitable.

Absorption

Another approximation neglects scattering entirely, and and only takes absorption into account, as described by the Beer-Lambert law,

$$\frac{I_t}{I_i} = 10^{-\varepsilon l c_{\text{conc}}} = e^{-\mu_a l} \tag{1.14}$$

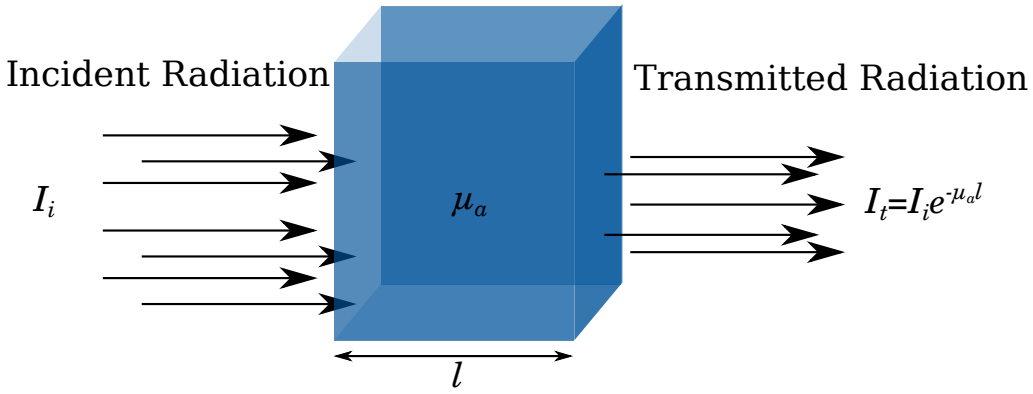

Figure 1.6: *If the optical behaviour of a medium is dominated by absorption, the Beer-Lambert law is a suitable description of the attenuation of incident radiation.*

In Equation 1.14 (illustrated in Figure 1.6), I_i and I_t are incident and transmitted intensity respectively. The first form of the Beer-Lambert Law in Equation 1.14 is usually used in chemistry and biochemistry, where ε is the molar extinction coefficient (or molar absorptivity) of the medium, and is usually measured in units of $\text{M}^{-1}\text{cm}^{-1}$. The molar concentration of the medium is c_{conc}, usually measured in units of M, and l is the path length of radiation through the medium (measured in cm). The Beer-Lambert law assumes scattering is negligible, so treats absorption as the sole cause of any extinction. The second form of the Beer-Lambert Law in Equation 1.14 is usually used in physics, meteorology and astronomy, where l is also the path length as above, and the absorption coefficient for a medium μ_{a} is defined as the probability, per unit path length, that a photon will be absorbed by the medium.

In the upper layers of the skin, scattering dominates, so the Beer-Lambert law is not suitable for simulating UVR transport though skin.

Monte Carlo Radiative Transfer

The term 'Monte Carlo Method' describes a class of algorithms that use random numbers to sample from probability distributions in order to obtain numerical results. The term 'Monte Carlo' was the codename given to the method for modelling random walks of neutrons during the Manhattan Project [24], where the first nuclear weapons were developed. The algorithm was computerised by von Neumann using the first general purpose electronic computer, the ENIAC (Electronic Numerical Integrator and Computer), built in 1945 [24].

In general, Monte Carlo methods involve finding all possible outcomes of an event, and ascribing the probability of each outcome occurring. The outcome of an event could be other events, which also have a set of outcomes, and so on. As long as the probabilities are known, a simulation can be built based on repeatedly randomly sampling these outcomes. Monte Carlo methods thus provide a way to model complicated stochastic processes, as long as the probabilities involved are known. Monte Carlo methods are widely used in physics [25], biophysics and medicine [7, 8, 26, 27] and beyond, for example in financial modelling [28], predicting election outcomes [29], and modelling the impact of a pandemic [30].

Monte Carlo Radiative Transfer (MCRT) uses random sampling of the mean free path of a photon, along with the optical properties of the skin (the absorption and scattering coefficients) to simulate the transfer of radiation through tissue. MCRT is able to consider the varying absorption and scattering in all directions within the skin, and as such is a good approach to use over the diffusion approximation or the Beer-Lambert law, as the numerical Monte Carlo algorithm should reproduce the results of an analytical solution of radiative transfer. MCRT models of human skin have been developed for applications in biomedical optics before [7, 8, 26, 31], however the work presented here forms the first comprehensive MCRT model of human skin built to simulate UVR transport [32, 33].

1.4 Thesis aims and summary

This thesis aims to present the development of an MCRT model capable of simulating the transfer of UVR through human skin. Chapter 2 provides a detailed description of the Monte Carlo Radiative Transfer (MCRT) algorithm used throughout this thesis. Chapter 3 describes the application of this algorithm to create a model capable of simulating UVR transport through the upper layers of the skin. The thesis aims to present a variety of applications of the model, along with details of data analysis methods used to both validate the model against published experimental results, and to examine predictions made by the model. Chapter 4 uses the model to quantify UVR induced DNA damage occurring in the basal layer of human skin. Chapter 5 builds on the work in Chapter 4 by extending the model to darker skin types. Chapter 6 again extends the model by the addition of a layer of sunscreen to the simulations. Chapter 7 describes the application of the code to theoretically determine whether a new treatment protocol for a specific type of psoriasis might be beneficial. Chapter 8 further extends the model to the UVC band, in order to theoretically assess the safety of UVC sterilisation lamps.

The final experimental chapter of this thesis, Chapter 9, is a departure from computational simulation, and details the assessment of the suitability of a commercially available hand held UVR

meter in measuring the UVR output of sunbeds in beauty salons and gyms within the Highland Council area.

Chapter 2

Monte Carlo radiative transfer

2.1 Monte Carlo radiative transfer

Monte Carlo radiative transfer (MCRT) simulates the transport of radiation through a highly scattering medium. Using the probabilistic nature of photon propagation, the random walk of photons through the medium are simulated. By repeating this many times, the result provides a numerical approximation to the solution to the RTE.

MCRT is well optimised to model a complex 3 dimensional (3D) structure such as the skin. In MCRT it is possible to model localised optical properties, and multiple physical quantities can be recorded simultaneously, with desired spatial resolution limited only by the computational power available. The input parameters for an MCRT simulation can easily reproduce experimental set-ups, providing opportunity to validate results from the simulation against those obtained by experiment [7, 31, 34, 35]. In addition, MCRT simulations can be designed to simulate situations that would be difficult to test experimentally.

The code used to develop the MCRT model presented here was, in its original form, developed for Astronomy research [36]. In order to simulate UVR transport through skin tissue, the code has been extensively altered. All code developed for this thesis is available at the DOI `https://doi.org/10.5281/zenodo.5651209`.

2.2 Random sampling

Monte Carlo (MC) methods are founded on randomly sampling from known probability distributions. Each sample must be random and independent, and collectively the samples must reproduce the probability distribution in question. During the simulation of the propagation of a photon, at every point where an interaction event occurs (scattering or absorbing), an independent random sample must be taken from the relevant probability distributions which represent the underlying physical process. The two random sampling methods used in this thesis are described here.

Rejection method

The rejection method involves mapping the outcomes of a uniform distribution, $U(0,1)$, to the outcome of interest. Then a value ξ is randomly sampled from the uniform distribution, $U(0,1)$. If ξ doesn't map to the outcome of interest, the sample is rejected.

A simple example could be the coin toss, as in Equation 2.1. An outcome is either heads, or not heads (tails). Each outcome must be random and independent. Assuming the coin is fair, the outcomes of heads or tails are equally likely; so these outcomes are mapped to the uniform distribution $U(0,1)$ by assigning half of the distribution to heads, and half to tails. Results for the 'coin toss' are shown for different numbers of samples in Figure 2.1, to illustrate that by increasing the number of samples, convergence to the probability distribution sampled is obtained.

$$P_{\text{heads}} = \begin{cases} 1 & \text{if } 0 < \xi \leq 0.5 \\ 0 & \text{if } 0.5 < \xi \leq 1.0 \end{cases} \tag{2.1}$$

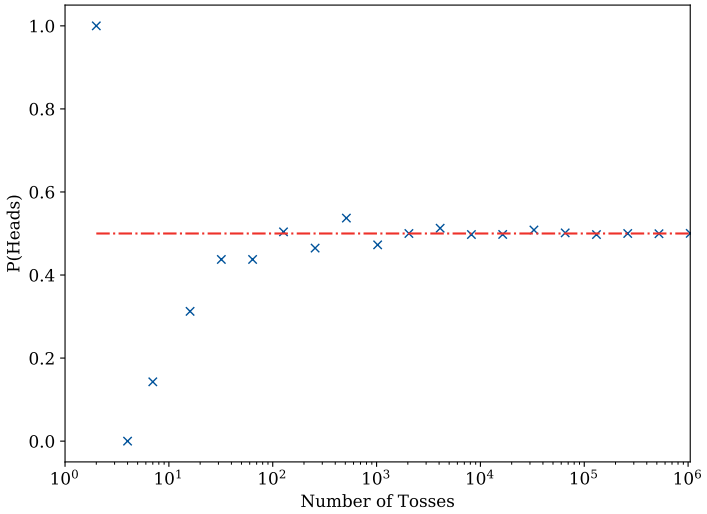

Figure 2.1: *Plot showing the number of heads in a simulated coin toss against number of throws (2^1 to 2^{20} tosses). As the number of throws increases, the $N_{\text{heads}}/N_{\text{throws}}$ converges on 0.5, as expected for a fair coin.*

Simulating the toss of an unfair coin, for example, one that only returned heads 10% of the time, could be achieved by sampling,

$$P_{\text{heads,unfair}} = \begin{cases} 1 & \text{if } 0 < \xi \leq 0.1 \\ 0 & \text{if } 0.1 < \xi \leq 1.0 \end{cases} \tag{2.2}$$

Within the research presented here, this technique is used when deciding whether a power packet will be absorbed or scattered, as discussed in the following sections.

Inverse transform sampling

Rejection sampling is computationally inefficient, as a proportion of the samples produced are always rejected. Inverse transform sampling ensures only samples fitting the probability distribution in question are produced.

The probability density function (PDF), usually denoted $f(x)$, gives the relative likelihood that a random variable would equal a given value at x. The cumulative distribution function (CDF) is usually denoted $F(x)$. The CDF can be thought of as the area under the PDF curve at x, and the CDF evaluated at X, $F(X)$, gives the odds of measuring any value up to and including X. The CDF is obtained from the PDF via Equation 2.3.

$$F(x) = \int_{x'\min}^{x} f(x')\mathrm{d}x' \tag{2.3}$$

where $f(x)$ is normalised from $x = x_{\min}$ to $x = x_{\max}$. Equation 2.4 details the method used to obtain an independent random sample X from the PDF $f(x)$. By setting the CDF $F(X)$ equal to a random number ξ (randomly sampled from the uniform distribution $U(0,1)$), then inverting the function such that $F^{-1}(\xi)$, the independent random sample X is obtained,

$$\xi = \int_{x_{\min}}^{X} f(x)\mathrm{d}x = F(X) \Rightarrow X = F^{-1}(\xi) \tag{2.4}$$

where the standard notation F^{-1} denotes the functional (not arithmetic) inverse of F, such that if $F : V \to W$ then $F^{-1} : W \to V$.

Given that ξ is a random number drawn from the uniform distribution $U(0,1)$, Equation 2.4 will return a random independent variable X. When the number of samples is very large, the distribution of the random variables X_i will reproduce the PDF. A practical example of inverse transform sampling of the exponential distribution function, $f(x) = e^{-x}$, and the effects of sampling size are detailed in Figure 2.2.

The method described above assumes the CDF $F(x)$ can be obtained analytically. If this is not possible (e.g., if the desired sampling distribution is an experimental dataset) then the CDF can be obtained numerically. Consider a discrete dataset represented by $g(x_i)$. First the area under the curve of the dataset is computed using the trapezoidal rule,

$$\int_a^b g(x)\mathrm{d}x \approx \sum_{k=1}^{N} \frac{g(x_{k-1}) + g(x_k)}{2} \Delta x_k \tag{2.5}$$

Where $[a, b]$ are respectively the start and endpoint of the dataset of interest. This interval $[a, b]$ is divided into N subintervals of size Δx_k (the separation between data points). By setting this area equal to 1, the PDF $f(x)$ is found,

$$\int_a^b f(x)\mathrm{d}x \approx \sum_{k=1}^{N} \frac{f(x_{k-1}) + f(x_k)}{2} \Delta x_k = 1 \tag{2.6}$$

To convert this to the CDF $F(x)$, the area under the curve up to and including each data point

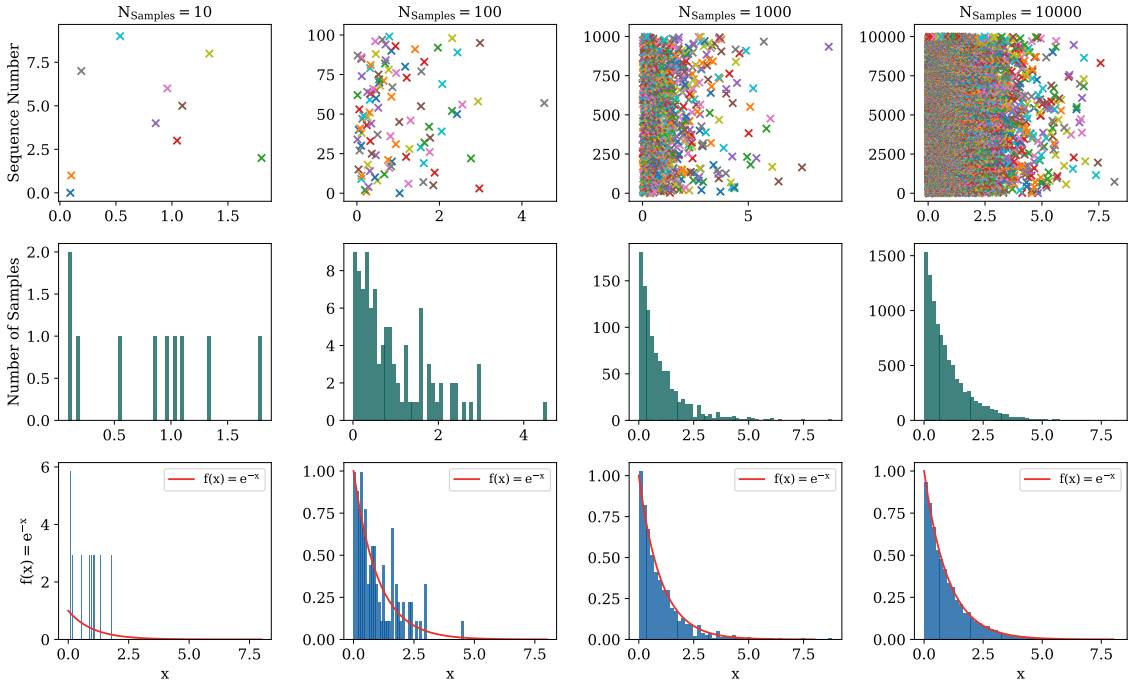

Figure 2.2: *Each column of plots shows results for a different number of random samples ($N_{samples}$ =10, 100, 1000 & 10000) using inverse transform sampling of the probability distribution $f(x) = e^{-x}$. In this case, $F(x)$ can be analytically determined as $F(x) = 1 - e^{-x}$. The CDF is inverted to obtain a random sample X_i, where $X_i = -\log_e(1-\xi)$. The first row is a scatter plot of the random samples, with the value of X_i on the x-axis, and point in the sequence the sample occurred on the y-axis. The second row shows a histogram of these samples (using 50 bins). The third row shows both a normalised histogram (the sum of the histogram area is normalised to 1), and the original probability distribution $f(x) = e^{-x}$. It is clear from the bottom row that the more samples, the more accurately the histogram reproduces the original function $f(x) = e^{-x}$.*

must be found, which can be inverted to obtain a random independent sample,

$$F(X) \approx \sum_{k=1}^{X} \Delta x_k F(X) \Rightarrow X = F^{-1}(\xi) \tag{2.7}$$

If this is repeated many many times, the distribution of the random independent samples will eventually match the PDF. An example of the process of turning a dataset into a PDF and CDF is shown in Figure 2.3, and of inverse transform sampling in practise in Figure 2.4.

Figure 2.4 shows the importance of obtaining enough samples to reproduce the desired function. Even for 10,000 samples, the spectrum from Figure 2.4 is not perfectly reproduced. The inverse transform sampling method is used extensively in the research presented here to randomly select a wavelength from an experimentally obtained spectrum, and in these cases sampling numbers range from 10^8 to 10^9.

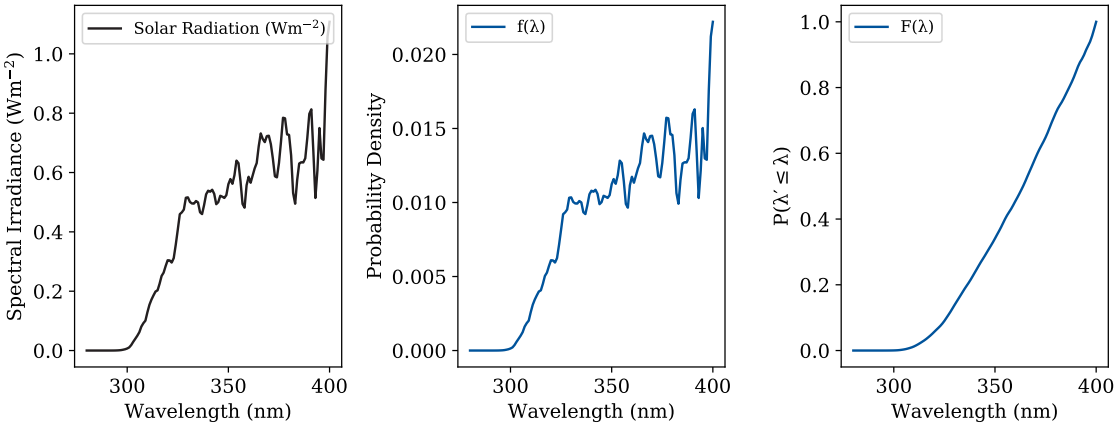

Figure 2.3: *The left plot shows a terrestrial UVR solar spectrum. The central panel shows the same data transformed into a PDF using Equation 2.5 (the area under the curve is equal to 1). The right panel shows the resulting CDF, the cumulative probability, taken from summing the area under $f(\lambda)$ up to each point λ_i, and it is this CDF which is inverted to obtain random independent samples (Equation 2.7).*

Pseudorandom numbers

Monte Carlo methods rely heavily on random numbers. Generation of true random numbers is slow, and to do a Monte Carlo simulation correctly, every random number must be independent. Pseudorandom numbers are produced by an algorithm (from a 'seed' supplied within the program), and have a list length, or period, within which they behave like random numbers. To optimise speed in a Monte Carlo simulation, a long list of pseudorandom numbers is used to represent the uniform distribution $U(0, 1)$, and ξ is drawn from this list.

The numeric simulations for this code are written in Fortran 90, and use the in-built random number function (`call random_number()` [1]). This inbuilt function has a period of $2^{256} - 1$, which

[1] See online GCC documentation: https://gcc.gnu.org/onlinedocs/gfortran/RANDOM_005fNUMBER.html

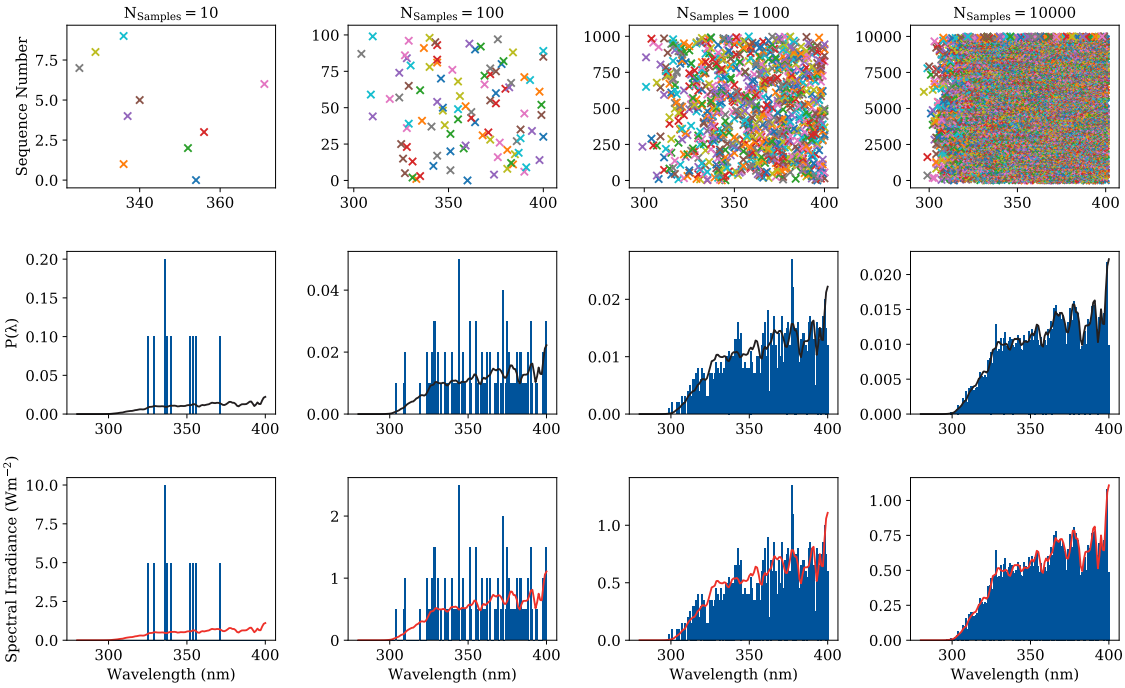

Figure 2.4: *Example of inverse transform sampling using a numerical rather than analytical inversion of the PDF. The probability distribution is generated from a terrestrial UVR solar spectrum (Figure 2.3). The bottom row indicates the importance of sampling in large quantities to reproduce the input spectrum, as the number of samples increases, the error between the sampled spectrum and the input spectrum reduces.*

is adequate for the simulations performed. Early versions of the codes developed tested both the inbuilt random number function and an external generator (e.g. `ran2` from Numerical Recipes [37]), and no difference was found in results.

2.3 The random walk

MCRT simulations should yield a solution to the radiative transfer equation by utilising the probabilistic nature of photon propagation. This is done via simulation of the random walk of a photon through a turbid medium. There are two components to the random walk: travelling between interaction points, and what happens at the interaction points.

2.3.1 Optical depth sampling

The easiest way to simulate the random walk is to find out how far a photon is likely to travel before it either scatters or is absorbed. This can be thought of as finding the probability that a photon will reach a distance S without interacting.

As discussed during the derivation of the radiative transfer equation (in Equations 1.5 and 1.6), the probability per unit path length that a photon will interact (either scatter or absorb) is given by,

$$\mu_\mathrm{t} = \mu_\mathrm{a} + \mu_\mathrm{s} \tag{2.8}$$

where μ_t is the probability of interaction per unit path length, which is the sum of μ_a (the probability of the photon being absorbed per unit path length) and μ_s (the probability of the photon being scattered per unit path length).

This can be used to find the probability of an interaction occurring over the infinitesimal distance $\mathrm{d}S$, which is defined in terms of the distance S divided into N segments, where N is very large,

$$\mathrm{d}S = \frac{S}{N} \tag{2.9}$$

Given Equations 2.8 and 2.9, the probability of the photon interacting over the infinitesimal distance $\mathrm{d}S$ can be expressed by,

$$P_\text{interaction}(\mathrm{d}S) = \mu_\mathrm{t}\mathrm{d}S \tag{2.10}$$

Over the infinitesimal distance $\mathrm{d}S$ the photon either interacts, or does not interact, meaning $P_\text{interaction}(\mathrm{d}S) + P_\text{no interaction}(\mathrm{d}S) = 1$.

Therefore the probability of no interaction occurring over the infinitesimal distance $\mathrm{d}S$ (the quantity of interest, from now on referred to as P) is,

$$P(\mathrm{d}S) = P_\text{no interaction}(\mathrm{d}S) = 1 - \mu_\mathrm{t}\mathrm{d}S \tag{2.11}$$

Given Equation 2.11, the probability of no interaction occurring over a second element $\mathrm{d}S_2$ is also $P(\mathrm{d}S_2) = 1 - \mu_\mathrm{t}\mathrm{d}S_2$ (where $\mathrm{d}S = \mathrm{d}S_2$), and the same for a third element $\mathrm{d}S_3$. Using the identity,

$$\lim_{N\to\infty}\left(1-\frac{x}{N}\right)^N = e^{-x} \tag{2.12}$$

the probability of not interacting over the entire distance $S = N\mathrm{d}S$ is given by,

$$P(S) = (1-\mu_\mathrm{t}\mathrm{d}S)_1(1-\mu_\mathrm{t}\mathrm{d}S)_2(1-\mu_\mathrm{t}\mathrm{d}S)_3....(1-\mu_t\mathrm{d}S)_N = \lim_{N\to\infty}\left(1-\mu_\mathrm{t}\frac{S}{N}\right)^N \tag{2.13}$$

Equation 2.13 (the probability of a photon reaching distance S without interaction) can be rewritten as,

$$P(S) = e^{-\mu_\mathrm{t}S} = e^{-\tau} \tag{2.14}$$

The average distance between events is the mean free path, $\frac{1}{\mu_\mathrm{t}}$. The value $\mu_\mathrm{t}S$ is the number of mean free paths travelled to reach S, and is defined as the optical depth, $\tau = \mu_\mathrm{t}S$.

Equation 2.14 is also the the PDF describing the likelihood that a photon will reach a distance S. Given this, inverse transform sampling can be employed to obtain independent random samples of the optical depth τ.

In order to randomly sample the optical depth, the inverse of the CDF must be found,

$$\xi = \int_0^{\tau_i} e^{-\tau}d\tau = F(X) \Rightarrow \tau_i = -\log_e(1-\xi) \tag{2.15}$$

Inversion of Equation 2.15 yields an independent and randomly sampled optical depth,

$$\tau_i = -\log_e(1-\xi) = -\log_e(\xi) \tag{2.16}$$

where $\xi - 1$ is replaced with ξ (as ξ is a random sample from the uniform distribution $U(0,1)$, it is also correct to say that $(1-\xi)$ is a random sample from the uniform distribution $U(0,1)$). The optical depth is then converted into a physical distance S_i by solving the integral,

$$\tau_i = \int_0^{S_i} \mu_t\mathrm{d}s \tag{2.17}$$

2.3.2 Interactions: scattering & absorption

When the photon reaches the randomly sampled optical depth, the photon has reached the interaction point. At this point, the photon must either scatter or absorb. The likelihood of either outcome happening is determined by the mean albdeo, $a = \frac{\mu_\mathrm{s}}{\mu_\mathrm{s}+\mu_\mathrm{a}}$, where μ_s and μ_a are the local scattering and absorption coefficients (known as the optical properties). The rejection method is used to determine whether the photon scatters,

$$P_\mathrm{scatter} = \begin{cases} 1 & \text{if } 0 < \xi \leq a \\ 0 & \text{if } a < \xi \leq 1.0 \end{cases} \tag{2.18}$$

If the photon is absorbed (not scattered), the random walk of that photon is terminated, and another photon starts the process of the random walk from the source position. So in this model, an absorption event means termination of that photon, and there is no further emission simulated

from the point of absorption (e.g. fluorescence is not taken into account in this model).

If the photon is scattered, and so is continuing on a random walk, a new direction and a new optical depth must be randomly sampled, and the photon progresses from the scattering location to the next interaction point.

Scattering

When a photon is scattered, the path of the photon changes. In skin tissue, most scattering is considered to be elastic (the kinetic energy of the photon is conserved, meaning there is no change in the wavelength of the scattered photon), and in the model presented here only elastic scattering is considered. However inelastic (Raman) scattering does occur in tissue, where the scattered photon exhibits a change in wavelength. This occurs at a rate of about 1 in 10^9 of scattered photons, which has been successfully modelled using MCRT methods [27].

Scattering is determined with respect to the reference frame of the travelling photon (illustrated in Figure 2.5).

With reference to the scattering term of the RTE (reproduced here as Equation 2.19), scattering into the entire solid angle is possible ($0 < \theta \leq \pi$ and $0 < \phi \leq 2\pi$).

$$\frac{\partial}{\partial t} u(\boldsymbol{r}, \hat{\boldsymbol{\Omega}}, t)_{\text{scatt}} = c_{\text{n}} \mu_{\text{s}} \int_{4\pi} u(\boldsymbol{r}, \hat{\boldsymbol{\Omega}}, t) P(\hat{\boldsymbol{\Omega}}', \hat{\boldsymbol{\Omega}}) d\hat{\Omega}' \tag{2.19}$$

As the scattering direction is considered an independent random variable, this requires random sampling. In isotropic scattering, all possible scattering angles are equally likely. However skin is highly forward scattering [38], and to reproduce this, inverse transform sampling from a phase function $P(\hat{\boldsymbol{\Omega}}', \hat{\boldsymbol{\Omega}})$ is required.

When taken in the reference frame of the travelling photon (see Figure 2.5), in skin, scattering into the azimuthal angle ϕ is equally likely, and so the following equation is used to obtain an independent random sample of ϕ,

$$\phi_i = 2\pi\xi \tag{2.20}$$

where, as before, ξ is randomly sampled from the uniform distribution $U(0, 1)$.

The Henyey-Greenstein phase function

The Henyey-Greenstein function,

$$P_{\text{HG}}(\theta) = \frac{1 - g^2}{4\pi\sqrt{(1 + g^2 - 2g\cos(\theta))^3}} \tag{2.21}$$

was originally used to describe diffuse dust scattering in space, and was also identified as a suitable function for modelling scattering in biological tissues [34].

The key parameter in the Henyey-Greenstein phase function is the anisotropy factor g,

$$g = \langle \cos(\theta) \rangle \tag{2.22}$$

defined as the expectation value of $cos(\theta)$, where θ is the angle between the direction of incidence and the direction of scattering. The g value varies between $-1 \leq g < 1$, where $g \approx -1$ indicates a

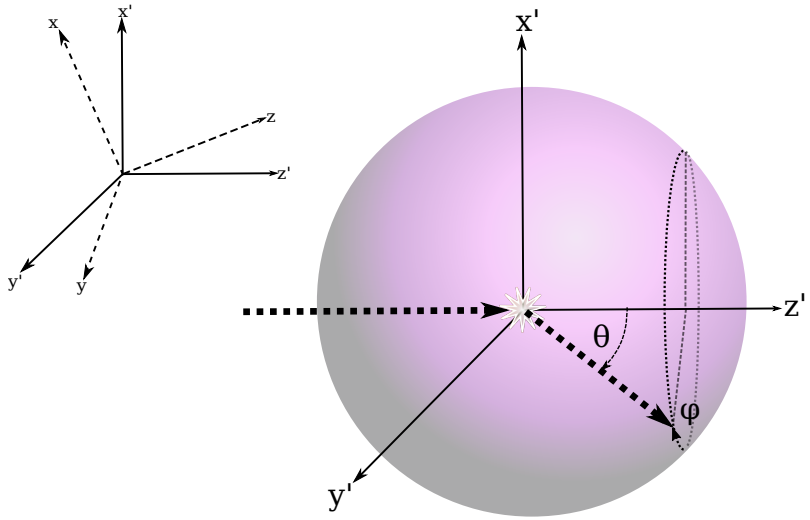

Figure 2.5: *Illustration of the geometry of the scattering direction in the frame of reference of the scattered photon (as indicated by x', y' and z'). In isotropic scattering, after an impact, scattering into each solid angle (or direction) θ and ϕ are equally likely. Skin tissue is highly forward scattering. In the reference frame of the photon, the azimuthal angle ϕ is equally likely, and the polar angle θ determined by inverse transform sampling of the Henyey Greenstein function (Equation 2.21). The scattering directions can be converted into the lab frame, indicated by the axes marked x, y and z, using the transforms in Equation 2.26.*

highly back scattering medium, $g \approx 1$ a highly forward scattering medium, and $g = 0$ an isotropically scattering medium.

In order to obtain random independent samples of the polar scattering angle θ, the inverse transform sampling method is used. To generate the CDF, Henyey-Greenstein phase function is integrated over the whole solid angle, and set equal to 1,

$$\int_{\phi=0}^{2\pi}\int_{\theta=0}^{\pi} P_{\mathrm{HG}}(\theta)\sin\theta \mathrm{d}\theta\mathrm{d}\phi = 2\pi\int_{\theta=0}^{\pi} P_{\mathrm{HG}}(\theta)\sin\theta\mathrm{d}\theta = 1 \tag{2.23}$$

Using this, the CDF can be found. The CDF of the Henyey-Greenstein phase function gives the odds of measuring a scattering angle θ up to and including θ_i,

$$2\pi\int_{\theta=0}^{\theta_i} P_{\mathrm{HG}}(\theta)\sin\theta\mathrm{d}\theta = \xi \tag{2.24}$$

This CDF can be inverted, allowing random sampling of $\cos\theta_i$,

$$\cos\theta_i = \frac{1}{2g}\left(1+g^2+\left(\frac{1-g^2}{1-g+2g\xi}\right)\right) \tag{2.25}$$

where, as before, ξ is drawn from the uniform distribution $U(0,1)$. As stated previously, this randomly sampled $\cos\theta_i$ is in the reference frame of the incident photon (Figure 2.5). To convert back to the lab frame, the transformations shown in Equation 2.26 [39] are applied, where n_x^{new}, n_y^{new}

and n_z^{new} are the new scattering directions in the lab frame, and n_x, n_y and n_z the old directions in the lab frame (θ and ϕ are in the reference frame of the photon, see Figure 2.5).

$$\begin{aligned} n_x^{\text{new}} &= \frac{\sin\theta(n_x n_z \cos\phi - n_y \sin\phi)}{\sqrt{1-n_z^2}} + n_x \cos\theta \\ n_y^{\text{new}} &= \frac{\sin\theta(n_y n_z \cos\phi + n_x \sin\phi)}{\sqrt{1-n_z^2}} + n_y \cos\theta \\ n_z^{\text{new}} &= \sqrt{1-n^2}\sin\theta\cos\phi + n_z\cos\theta \end{aligned} \tag{2.26}$$

2.4 Coding implementation of MCRT

In an ideal simulation, it would be possible to track the progression of every photon through a continuous medium. In practice, computer memory and speed set limit what can and cannot be simulated (and on how much data can be gathered at what resolution). To implement MCRT into code that will run efficiently, the medium is discretised by a grid, creating voxels, and individual photons are bundled into packets.

2.4.1 Power packets

Although it would be ideal to simulate the progression of every single photon through the medium, in practise when simulating levels of radiation of interest in photobiology, to do so would take too long using standard desktop levels of computing power. To simulate every photon incident on 1 mm^2 of skin from midday equatorial sunlight in one second would require simulation of about 10^{15} photons[2].

To overcome this, photons are bundled into packets [40], and the progression of a power packet is tracked through the medium. The number of 'real' photons of wavelength λ (N_λ) represented by a power packet is given by,

$$N_\lambda = E_{i,\lambda}\lambda\frac{1}{hc} \tag{2.27}$$

where h is Planck's constant, c the speed of light, and $E_{i,\lambda}$ is the energy per MCRT power packet. $E_{i,\lambda}$ is given by,

$$E_{i,\lambda} = \frac{I_\lambda A \Delta t}{N_{\text{pkt},\lambda}} \tag{2.28}$$

Where I_λ is the irradiance of the source at wavelength λ, A the area illuminated and $N_{\text{pkt},\lambda}$ the number of packets simulated at wavelength λ. Power packets can be converted into an 'energy packet' by multiplication of an illumination time Δt.

Typically in the MCRT simulations presented in this thesis, the total number of packets simulated (over all wavelengths) ranges from 10^7 to 10^9. When a power packet is initialised, a random and independent wavelength is selected from the input spectrum using the methods detailed in Figures 2.3 and 2.4. This thesis does not cover tissue fluorescence or Raman scattering, so all power packets keep the same wavelength throughout the random walk, and absorption is modelled by termination of the power packet.

[2] In the simulations performed here, simulating 10^8 takes about 20 minutes, so without considerable speed up attempts, simulating 10^{15} photons would take about 380 years.

2.5 3D grid code

The MCRT simulations presented in this thesis take place in a 3D grid of voxels (volumetric pixels). The voxels discretise the medium. This provides an easy way to set optical properties, to track the progression of power packets through the medium, and most importantly to record results. The specifics of setting up the grid with the correct optical properties to model the upper layers of skin will be described in the next chapter.

Packet progression

When a power packet (with a randomly selected wavelength) is launched into the grid, it does so with a randomly sampled optical depth τ (Equation 2.16). The initial direction of the power packet will be determined by the source being simulated. The power packet will travel the distance S (Equation 2.15), which is determined by the local optical properties. In the 3D grid model, these optical properties are discretised to a voxel, such that

$$\tau = \sum_i \mu_{\mathrm{t},i} \Delta s_i \tag{2.29}$$

where $\mu_{\mathrm{t},i} = \mu_{\mathrm{a},i} + \mu_{\mathrm{s},i}$, the local optical depth to voxel i, and Δs_i the distance across voxel i travelled by the power packet.

With reference to Figure 2.6, Equation 2.30 describes how the power packet is progresses through the grid, voxel by voxel, until it reaches the randomly selected optical depth τ.

$$\tau = \sum_i \mu_{\mathrm{t},i} \Delta s_i = \mu_{\mathrm{t}'} \Delta s_1 + \mu_{\mathrm{t}'} \Delta s_2 + \mu_{\mathrm{t}''} \Delta s_3' \tag{2.30}$$

When a new voxel is reached, the distance to the nearest voxel along the direction of travel is calculated (in Figure 2.6, this distances are labelled by Δs_1, Δs_2 and Δs_2). This distance is added to a running total of accrued optical depth τ_{tot}. If this accrued running total $\tau_{\mathrm{tot}} > \tau$, then the interaction point will be within the current cell. The distance within that cell to the interaction point is calculated (in Figure 2.6, $\Delta s_3'$). When the power packet reaches the interaction point, it either scatters or absorbs.

Every voxel contains a wavelength resolved running total of the path lengths accrued within that voxel,

$$S_{\mathrm{vox},\lambda} = \sum_i \Delta s_{i,\lambda} \tag{2.31}$$

These are used to estimate absorbed energy and fluence.

Path length counters

In skin tissue, scattering events vastly outnumber absorption events, however, it is absorption events that initiate photobiological processes. To gain good signal to noise, and reduce simulation runtime, estimators are used to calculate the energy absorbed within a voxel. Estimators are also used to calculate the fluence rate within a voxel.

The path length estimators employed here in the context of photon transport were introduced

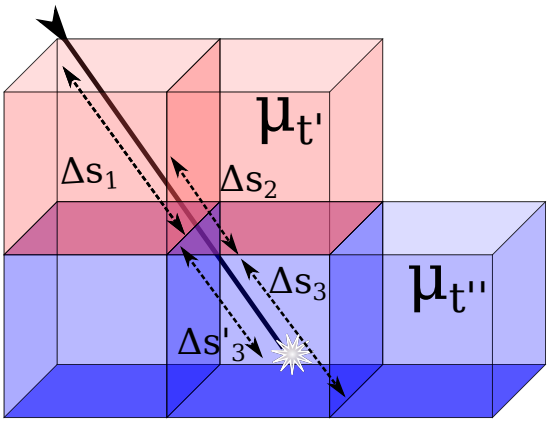

Figure 2.6: *Illustration of how the power packet progresses through the 3D grid. The coloured voxels represent different optical properties. The white star is the interaction point, located within a voxel. If the power packet were to progress across the whole final voxel, the optical depth travelled would be further than the randomly sampled τ; so the distance to the true interaction point is calculated within that voxel*

.

by Lucy [40]. These utilise the distance a power packet travels within a voxel (Δs from the packet progression algorithm, as described above in Figure 2.6 and Equation 2.30) to estimate the energy absorbed within a voxel, and the fluence through a voxel.

In order to estimate the total energy absorbed by a voxel, first the contribution from a single power packet is considered. The estimated energy absorbed within a voxel is proportional to the probability of the power packet being absorbed over the distance travelled within that voxel, $\mu_a(\lambda)\Delta s$. A single power packet of wavelength λ that travels a distance Δs in a voxel representing a medium of absorption coefficient $\mu_a(\lambda)$, will contribute an amount of energy $E_{\text{vox},i}$,

$$E_{\text{vox},i} = E_i \mu_{\text{a}}(\lambda) \Delta s_\lambda \tag{2.32}$$

recalling from Equation 2.28 that the energy carried by an individual power packet is given by,

$$E_{i,\lambda} = \frac{I_\lambda A \Delta t}{N_{\text{pkt},\lambda}} \tag{2.33}$$

where A is the area illuminated and $N_{\text{pkt},\lambda}$ the number of packets simulated at wavelength λ. Every voxel contains a wavelength resolved running total of the path lengths accrued within that voxel,

$$S_{\text{vox},\lambda} = \sum_i \Delta s_{i,\lambda} \tag{2.34}$$

Over all wavelengths, within each voxel, this sums to,

$$S_{\text{vox}} = \sum_\lambda \sum_i \Delta s_{i,\lambda} \tag{2.35}$$

Given this, the total estimation of the energy per volume per second absorbed within the voxel

of volume ΔV from the contributions of all packets from all wavelengths over time Δt is given by

$$Q_{\text{vox}} = \frac{E_i}{\Delta V \Delta t} \sum_i \mu_{\text{a}} \Delta s = \frac{IA}{N \Delta V} \sum_i \mu_{\text{a}} \Delta s \tag{2.36}$$

A useful quantity in photobiology is the spectrally resolved fluence rate. When radiation penetrates into tissue, the direction of the radiation is not important in mediating photobiological processes, but the relative intensities of the wavelengths are.

Similarly to the derivation of the RTE, to determine the spectrally resolved fluence (energy flow per unit area, per unit time), the starting point is the energy density u (Jcm^{-3}), the energy per unit volume,

$$u_\lambda = \frac{\psi_\lambda}{c} \tag{2.37}$$

where c is the speed of light.

The energy contributed by a power packet to a voxel is directly proportional to the time the power packet spends in that voxel,

$$\delta t = \frac{\Delta s}{c} \tag{2.38}$$

So as a proportion of the total illumination time,

$$E_{\lambda,\text{vox},i} = E_{i,\lambda} \frac{\delta t}{\Delta t} = \frac{E_{i,\lambda}}{\Delta t} \frac{\Delta s_\lambda}{c} \tag{2.39}$$

where again $E_{i,\lambda}$ is the energy of a power packet. Summing all the contributions of the power packets (of wavelength λ) within the grid cell (Equation 2.34), and using the identity in Equation 2.33, the energy density (Jcm^{-3}) is obtained,

$$\begin{aligned} u_\lambda &= \frac{1}{\Delta V} \sum_i E_{\lambda,\text{vox},i} = \frac{1}{\Delta V} \frac{\delta t}{\Delta t} \sum_i E_{i,\lambda} \\ &= \frac{I_\lambda A \Delta t}{N_{\text{pkt},\lambda}} \frac{1}{\Delta t \Delta V c} \sum_i \Delta s_\lambda = \frac{I_\lambda A}{\Delta V N_{\text{pkt},\lambda} c} \sum_i \Delta s_\lambda \end{aligned} \tag{2.40}$$

Using the identity in Equation 2.37, the spectrally resolved fluence rate can be written as,

$$\psi_\lambda = \frac{I_\lambda A}{\Delta V N_{\text{pkt},\lambda}} \sum_i \Delta s_\lambda \tag{2.41}$$

Equation 2.41 is used extensively in the research presented here to quantify the spectral attenuation of UVR as it penetrates into skin tissue. By keeping a running total of the wavelength resolved path lengths in each voxel (Equation 2.34), Equation 2.41 can be used to extract the estimated fluence reaching any voxel in the model.

2.5.1 Simulating an infinite layer of skin

To simulate a layer of skin, repeating boundaries are implemented on the vertically oriented faces of the grid, as illustrated in Figure 2.7. A power packet leaving the grid from a vertical face rejoins the grid on the opposing vertical face, with all properties pertaining to the power packet other than

position retained. Any packets leaving by the bottom of the grid are terminated. This simulates an infinitely repeating medium in the horizontal directions, and so approximates a 1 mm^2 section of a large area of skin of depth 1 mm.

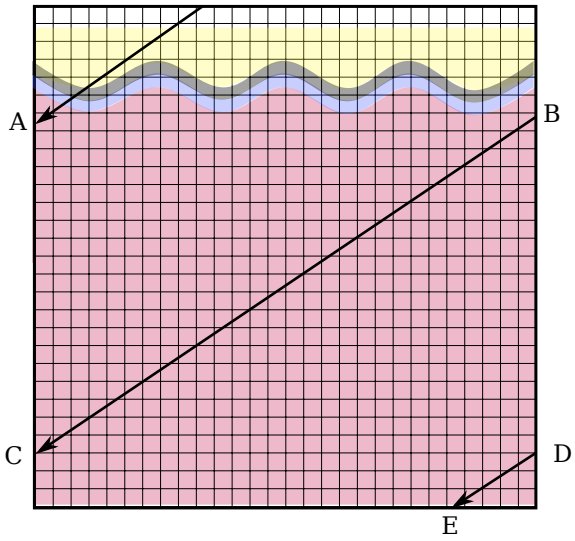

Figure 2.7: *Illustration of the implementation of repeating boundaries. Consider a power packet, which on initialisation has a randomly sampled path length that happens to be much larger than any of the grid dimensions. If the power packet leaves the grid at position A, the power packet is immediately restated at position B (retaining all properties except position). if the power packet then leaves the grid again at position C, the power packet is again restarted at position D. If the packet then progresses and leave the grid at position E, the packet is terminated.*

2.5.2 Reflections and refraction

All tissue, including the skin, has a different refractive index to the air. As such, reflections and refraction at the air-skin boundary must be accounted for in the model (Figure 2.42). If a power packet is incident at angle θ_i from the normal, then the reflected angle (θ_r) will be equal to the angle of incidence ($\theta_i = \theta_r$). The angle of refraction θ_t is given by Snell's law,

$$n_i \sin i = n_t \sin \theta_t \tag{2.42}$$

where n_i and n_t are the refractive indices of the air and the skin (as shown in Figure 2.42.

For unpolarised light, the probability that a photon incident on a refractive index boundary will reflect, R, is given by the Fresnel Equations,

$$R(\theta_i, \theta_t) = \frac{1}{2}\left[\left|\frac{n_i \cos\theta_i - n_t \cos\theta_t}{n_i \cos\theta_i + n_t \cos\theta_t}\right|^2 + \left|\frac{n_i \cos\theta_t - n_t \cos\theta_i}{n_i \cos\theta_t + n_t \cos\theta_i}\right|^2\right] \tag{2.43}$$

R is calculated for a given incident direction, and randomly sampled using the rejection method to decide whether the power packet will enter the medium and refract, or reflect,

$$P_{\text{refract}} = \begin{cases} 1 & \text{if } 0 < \xi \leq R(\theta_i, \theta_t) \\ 0 & \text{if } R(\theta_i, \theta_t) < \xi \leq 1 \end{cases} \tag{2.44}$$

where again, ξ is a random sample from the uniform distribution $U(0, 1)$. If the packet enters the medium, then the random walk simulation begins. If the packet reflects, the packet is terminated and another randomly sampled. Capturing the photons that reflect is an important part of MCRT, as this is the physical behaviour of radiation incident on tissue.

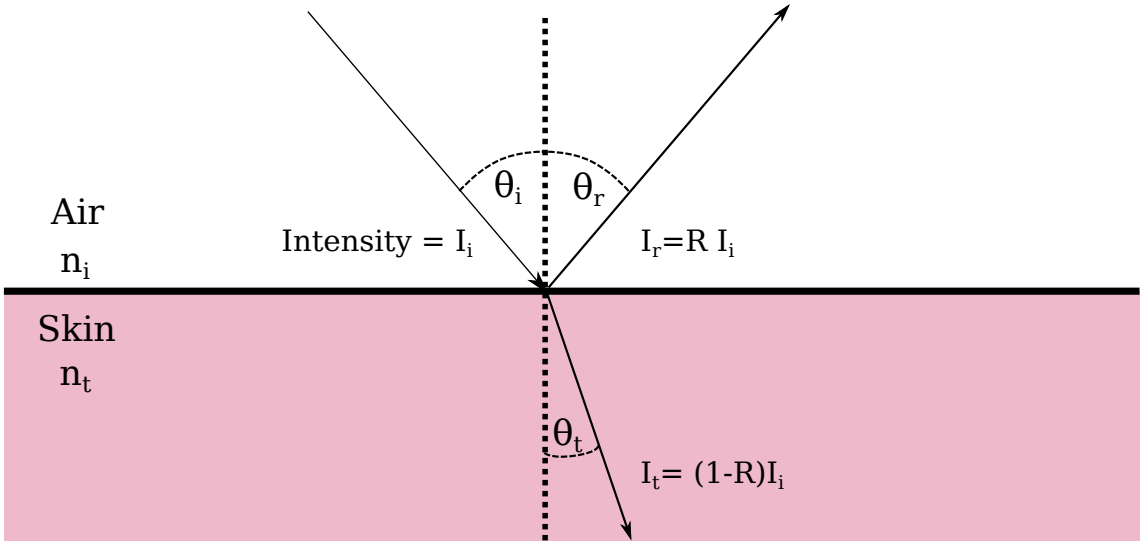

Figure 2.8: *An illustration of reflection and refraction of radiation at the air-skin boundary. The angle of incidence always equals the angle of reflection $\theta_i = \theta_t$), and the angle of refraction θ_t is found using Snell's law (Equation 2.42. The probability of reflection is found using the Fresnel equations which are combined in Equation 2.43.*

Total internal reflection

In the case that an incident power packet enters the medium, and is scattered back towards the surface, total internal reflection may take place if the incident angle θ_i is greater than the critical angle θ_c,

$$\theta_c = \arcsin(n_i/n_t) = \arcsin(n_{\text{skin}}/n_{\text{air}}) \tag{2.45}$$

taking note that the incident power packet is now on the skin side with $n_i = n_{skin}$ and $n_t = n_{air}$. In the case that $\theta_i > \theta_c$, the power packet undergoes total internal reflection, and continues the path length progression after being reflected. In the case that $\theta_i < \theta_c$, the power packet can either be reflected or refracted (and leave the medium). The behaviour is determined by calculating $R(\theta_i, \theta_t)$ (Equation 2.43), and random sampling using the rejection method as described by Equation 2.44.

2.6 Code validation

It is important to verify that the code could reproduce results from an existing published tissue MCRT simulation.

Jacques et al.[41] developed an MCRT code to simulate the effects of photobleaching during photodynamic therapy in rat skin. The results of their simulations were validated against experiment. Within this paper, the authors simulated the penetration of radiation into rat skin using MCRT, and fitted a function to the results,

$$\Psi(z) = \Psi(0)(C_1 e^{-k_1 z/\delta} + C_2 e^{-k_2 z/\delta}) \tag{2.46}$$

where $\Psi(z)$ is the fluence at depth z, $\Psi(0)$ the incident irradiance, and C_1,k_1,C_1,k_2 and δ are wavelength dependent parameters fitted to the simulation, described in Table 2.1.

Wavelength (nm)	μ_a (cm^{-1})	μ_s (cm^{-1})	C_1	k_1	C_2	k_2	δ (cm)
420	1.8	82	5.76	1.0	1.31	10.2	0.047
630	0.23	21	6.27	1.0	1.18	14.4	0.261

Table 2.1: *Fitting parameters for Equation 2.46*

A comparison of the results from the grid code and Equation 2.46 is shown in Figure 2.9. The simulation was set up on a grid of size x =2 cm, y =2 cm and z =2 cm discretised into $200 \times 200 \times 200$ voxels. The optical properties for the simulation are μ_a and μ_s, detailed in Table 2.1, and refractive index $n = 1.38$, and anisotropy factor $g = 0.9$. There is no differentiation in the optical properties between layers of the rat skin within this simple model. The simulation was run with 10^8 power packets, and takes about 25 minutes on the desktop PC.

Figure 2.9 shows excellent agreement between the results of the simulation and the fitted function. The second panel in Figure 2.9 closely inspects the deviation just under the surface of the skin, which is more pronounced for the shorter wavelength. This is because the impact of voxel resolution is more pronounced near the surface of the skin (increasing voxel resolution increases computation time).

To ensure the results presented within this thesis are a true representation of a numerically correct MCRT simulation, this validation step was repeated every time the MCRT code was materially altered. By confirming results matched the Jacques results, this confirmed the code was correctly simulating the transport of photons though a 3D grid, and could be applied to clinically relevant problems.

2.6.1 Convergence

In order to have confidence that the simulations were performed using enough samples, each simulation was checked for convergence. This was achieved by repeating the same MCRT simulation with three different pseudo random number seeds, and if the results did not differ by more than 3 significant figures, this was considered to converge. In practise, initial simulations would be run with small numbers of packets (e.g. 10^6 packets) to check that packet progression was occurring as expected. Then, these were increased by a factor of 10, until convergence was reached. For

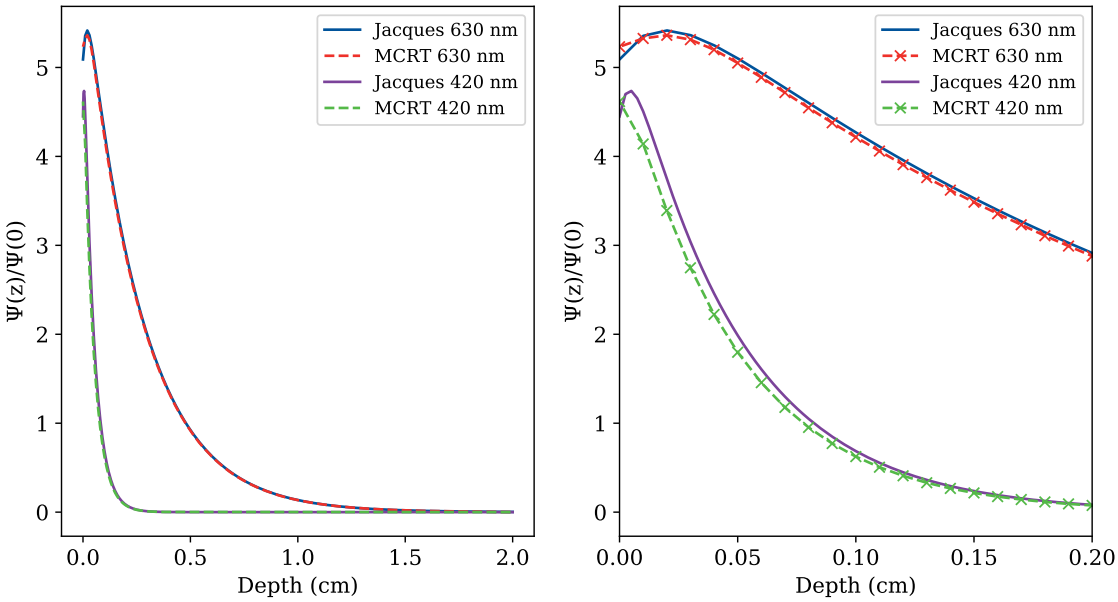

Figure 2.9: *A comparison of the results from the grid code and Equation 2.46 is shown in Figure 2.9. The plot shows normalised fluence against penetration of radiation as a function of depth for two wavelengths, 420 nm and 630 nm.*

example, 10^8 power packets is more than adequate for the validation steps above, and for most of the simulations performed in this thesis. In practise, 10^8 power packets usually gave a convergent result and was relatively fast to run (about 20 minutes). However, for some simulations described later on in this thesis, this was increased by a factor of 10 again, to 10^9 power packets.

The code as described here can be adapted to simulate non ionising radiation transport through tissue. The next chapter describes the application of this code to the specific case of simulating UVR transport through the upper layers of human skin.

Chapter 3

The UV-MCRT skin model

The previous chapter described the algorithmic application of MCRT to a 3D voxelated grid code. In order to simulate the transfer of UVR through human skin, optical properties that describe UVR interaction with skin tissue must be applied to the grid code.

This chapter describes the five layer MCRT skin model developed for modelling Fitzpatrick Skin Types I & II (see Table 1.1 in Chapter 1). Subsequent chapters describe applications and modification of this code in order to simulate some photobiological processes (such as DNA damage and phototherapy), darker skin types, and UVC irradiation. The basal layer is the location of most concern when investigating carcinogenic consequences of UVR exposure, and as such, the MCRT model developed must be able to simulate UVR transfer to the basal layer. The model must also allow relevant physical quantities, such as fluence and absorbed energy, to be extracted from the voxels representing the basal layer.

3.1 Grid geometry

In order to simulate MCRT of UVR through the skin, a 3D grid was built and divided into layers in order to model the upper layers of the skin. The global dimensions and voxel resolution of the grid are detailed in Table 3.1.

The grid has 101 voxels in each dimension (rather than 100; which would give grid resolution of 10 μm). This is an artefact from astronomical applications of this MCRT code, where a common applications involve a central emission source. By setting odd numbers of voxels, and fixing coordinates such that the origin is at the centre of the grid, this means a single voxel is fixed at the centre of the grid. In the simulations performed earlier on in this research (e.g. those presented in Chapter 4), retaining an odd number of voxels (101) in the lateral dimensions allowed results from a central slice through the grid to be extracted easily. However, in this case, keeping 101 voxels in the vertical dimension was unnecessary, and using 100 voxels would have made depth based analysis easier. In further chapters in this thesis, where central slice results are not presented, the numbers of grid voxels were chosen such that the resolution of the voxels was either 10 μm or 1 μm, not 9.9 μm as detailed in Table 3.1.

The layers simulated are the stratum corneum, the epidermis, a layer of melanin, the basal layer, and the dermis. The layer depths are detailed in Table 3.2 and shapes illustrated in Figure 3.2.

Dimension	Size	Number of Voxels	Resolution
x	1 mm	101	9.9 μm
y	1 mm	101	9.9 μm
z	1 mm	101	9.9 μm

Table 3.1: *Specifications of spatial grid used to simulate the upper layers of skin tissue as illustrated in Figure 3.2. It should be noted that each voxel (in total, 101 × 101 × 101 ≈ 10^6 voxels) is able to record the wavelength resolved fluence spectrum reaching that voxel using the wavelength resolved path length counter described in Chapter 2. To simulate a layer of skin, repeating boundaries were implemented on the vertically oriented faces of the grid. Any packets leaving by the bottom of the grid are terminated. This simulates an infinitely repeating medium in the horizontal directions, and so approximates a 1 mm^2 section of a large area of skin of depth 1 mm.*

Although the living epidermis is further stratified into the stratum lucidium, stratum granulosum and stratum spinosum, within this thesis these are treated as one layer, as it is assumed in this model that the constituent layers all transmit UVR in the same way.

The model, as described here, is designed to simulate Fitzpatrick type I and II skin that has not been exposed regularly to UVR (for example the underside of the arm, or the shoulder). In non-exposed types I & II, the melanin in the skin is mostly localised above the basal layer [42, 43]. By way of approximation, in the model, this distribution of melanin is simulated by separating the epidermis into two parts. The bulk of the modelled epidermal layer contains no melanin, and a thinner, concentrated melanin layer is sited directly above the basal layer. Within skin types III-VI, melanin is distributed throughout the epidermis in varying concentrations.

Layer	Depth (Healthy Skin)	SD
Stratum Corneum*	14.8 μm	4.8 μm
Epidermis	63.7 μm	–
Melanin Layer	73.7 μm	–
Basal Layer*	83.7 μm	16.6 μm
Dermis**	2000-6000 μm	–

Table 3.2: *Epidermal depths marked * taken directly from Sandby-Møller et al. [44]. Other depths are adapted to separate the melanin layer from the bulk of the epidermis in order to simulate non exposed skin. **The dermis extends deeper than the extent of our model, and as such, any packets that would reach deeper than 1 mm and scatter back to the basal layer are not accounted for. Due to the large optical depth a photon would have to travel for this to happen, this is unlikely, and as such was neglected.*

The grid as described in Table 3.1 is divided into layers on a voxel by voxel basis, which are mapped to optical properties pertaining to that skin layer. This allows multiple layer skin structures to be simulated. Within a single voxel the optical properties are homogeneous. Each voxel is mapped to specific optical properties depending upon its spatial location, allowing the structure of skin to be simulated via a five-layer model. This is illustrated in Figure 3.2.

As well as providing a convenient way to apply the optical properties to the model, the grid layout allows each voxel to function as a 'detector'. Each voxel contains a wavelength resolved path length counter, thus maintaining a running total of the path lengths of the power packets passing through that voxel. From this path length counter, fluence and absorbed energy can be estimated.

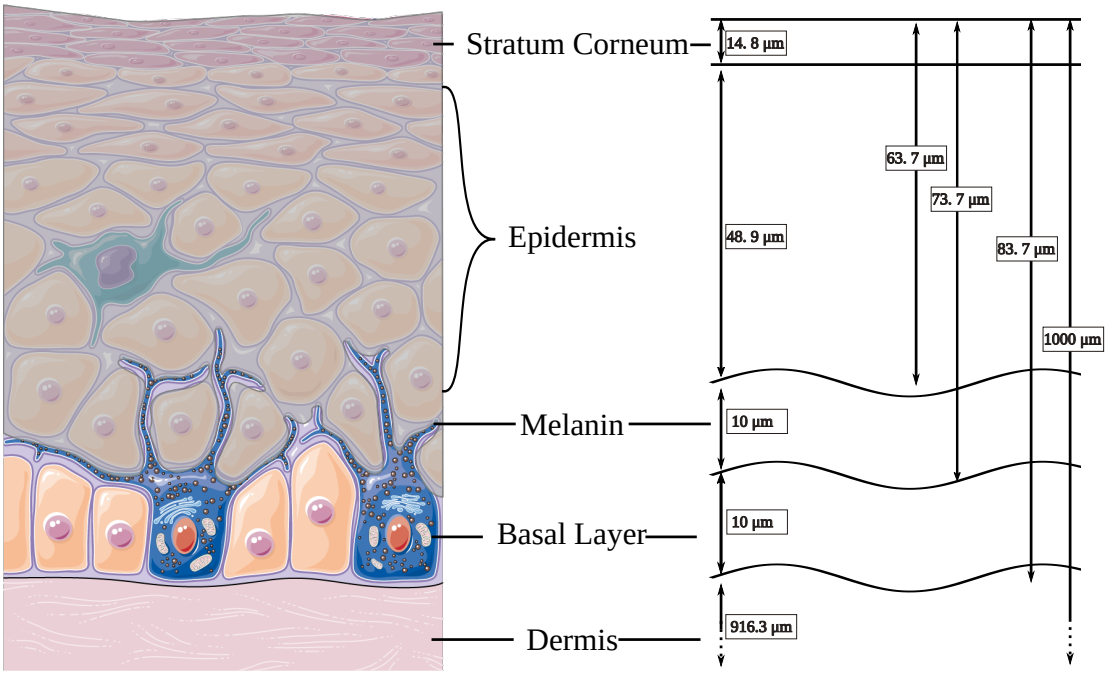

Figure 3.1: *An illustration of the geometry of the model alongside a sketch of the upper layers of the skin (adapted from Figure 1.1), with the basal layer highlighted. The geometry labelled here refers to the model, and is detailed in Table 3.2 and by Equations 3.3 to 3.7.*

The voxelated grid is thus used to both discretise the optical properties, and as method to bin results by location (by extracting results via the path length counter). Beyond the discretisation of the optical properties, the grid resolution itself has no effect on the underlying radiation transfer algorithm performed.

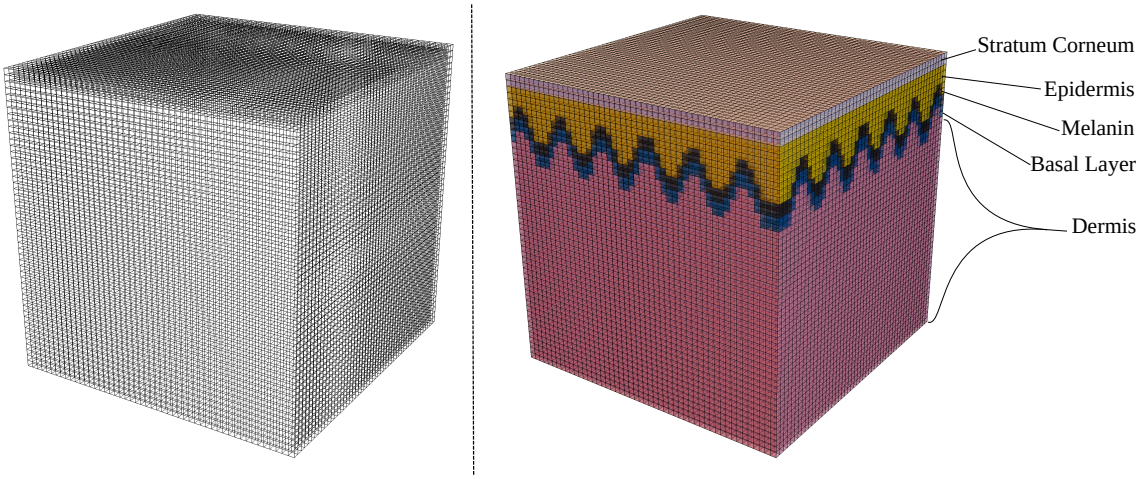

Figure 3.2: *Illustration of the voxelated five layer skin model (shown with 50 × 50 × 50 voxels for clarity). On the left the empty grid is shown, and on the right, an illustration of the voxels with assigned layers, which are mapped to optical properties.*

3.2 Optical properties

Optical properties describe how radiation interacts with matter. The optical properties discussed here include absorption (μ_a), scattering (μ_s and g), and refractive index n.

3.2.1 Refractive index

Optical properties of tissue vary widely across, and within, individuals [45, 46, 47]. There is limited data on optical properties of skin tissue in the UVR, and this area would benefit from a comprehensive literature review. Although the model is a five layer skin model, there are some optical properties that are considered to be the same throughout the model. For example, the refractive index n_skin [48] is described by,

$$n(\lambda) = 1.26 + \frac{4.54 \times 10^2}{\lambda - 2.87 \times 10^3} \tag{3.1}$$

where wavelength λ is given in nm. This is taken from Ding et al. [48]; where the dataset presented contains only one data point in the UVR (325 nm).

Due to the refractive index change between the air and the surface of the skin, Fresnel reflections are taken into account at this boundary (as described in the previous chapter).

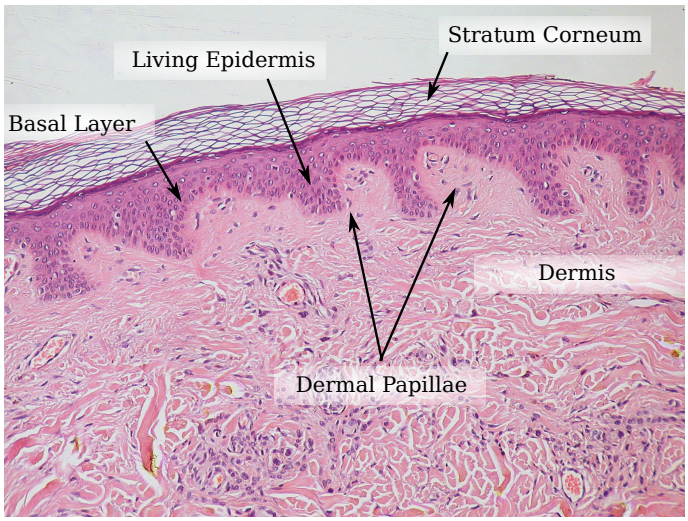

Figure 3.3: *Histology section of healthy skin magnified* $\times 10$ *(in the public domain). The thick, clear, stratum corneum at the surface is clearly visible, and the undulating dermal papillae (simulated using Equations 3.4-3.7) are also highlighted. This image shows the stratum corneum to be thicker (compared to the epidermis) than the depths reported in Table 3.2 suggests. This may be due to effects of sample processing, or this image may have a particularly thick stratum corneum or thin epidermis.*

3.2.2 Anisotropy factor

The anisotropy factor g, the parameter in the Henyey-Greenstein scattering phase function, (Chapter 2) is assumed to vary linearly with wavelength as described by Equation 3.2 [38],

$$g(\lambda) = 0.62 + 0.290\lambda \times 10^{-3} \tag{3.2}$$

Figure 3.4 shows the wavelength dependence of Equation 3.2 and the effect on the shape on the angle sampled from the Henyey-Greenstein phase function (equation 2.21).

3.2.3 Absorption and scattering

Absorption coefficients (μ_a) and scattering coefficients (μ_s) can vary across the different layers of the skin.

Stratum Corneum (layer 1)

The wavelength dependent absorption and scattering spectra for the stratum corneum are taken directly from van Gemert et al. [38] and shown in Figure 3.5. The stratum corneum provides significant protection against UVR , due to high absorption and scattering, particularly in the UVB. It is assumed for the purposes of this model that the stratum corneum in non-UV adapted Fitzpatrick skin type I or II skin contains no melanin, and as such has no influence on the absorption or scattering properties of this layer.

In this model the stratum corneum is approximated as having a flat surface and a flat base. Using the depth listed in Table 3.2, each voxel with a position between the surface of the model

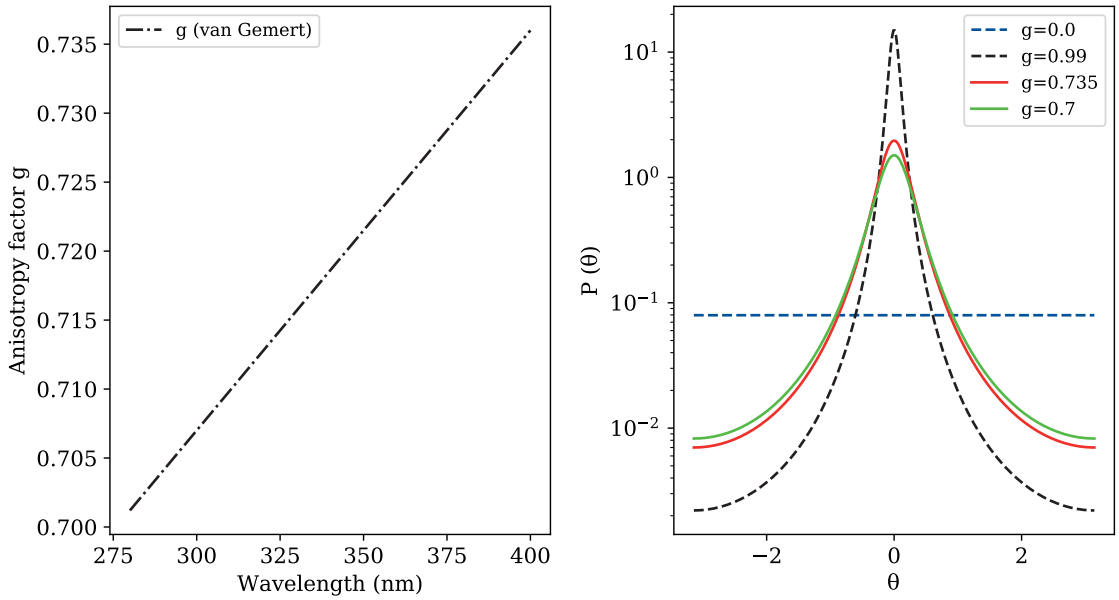

Figure 3.4: *The left panel shows the linear wavelength dependence of the anisotropy factor g, which is the time average of the polar scattering angle θ, $\langle \cos\theta \rangle$, in the reference frame of an incident photon [38]. The right panel shows the Henyey-Greenstein phase function (Equation 2.21 in Chapter 2) calculated for the limiting values of g, which gives the probability of the polar scattering angle with respect to impact direction.*

($z_{\max}$) and the base of the stratum corneum ($z_{\text{sc}} = 14.8\ \mu$m) is assigned the absorption and scattering coefficients shown in Figure 3.5.

Living Epidermis (layer 2)

Below the stratum corneum is the epidermis. It is modelled as having a flat surface and an undulating base to represent the dermal papillae (the wavelike structure clearly visible in Figure 3.3 and described by Equation 3.3),

$$z_{\text{base}}(x, y) = 0.03\ \text{mm} \times \sin\left(\frac{x}{0.015\ \text{mm}}\right) \times \cos\left(\frac{x}{0.015\ \text{mm}}\right) \tag{3.3}$$

where the coefficients are estimated from confocal microscopy images of human skin published by Jensen et al. [49]. The resulting geometry from this modelled surface is a regular structure (as shown in Figure (3.2) which aims to approximate the shape o the epidermal-dermal junction. It is clear from the histology section shown in Figure 3.3 that the epidermal-dermal junction is irregular. In future work, the effect of de-regularising this modelled junction could be investigated.

The scattering and absorption of UVR within the epidermis has a significant effect on the amount of UVR reaching the basal layer. The epidermal layer also contains living cells that are susceptible to UVR induced DNA damage, although it is unlikely that DNA damage occurring here would have serious consequences [50].

To simulate skin types I & II, the modelled epidermis is separated into two parts- a main

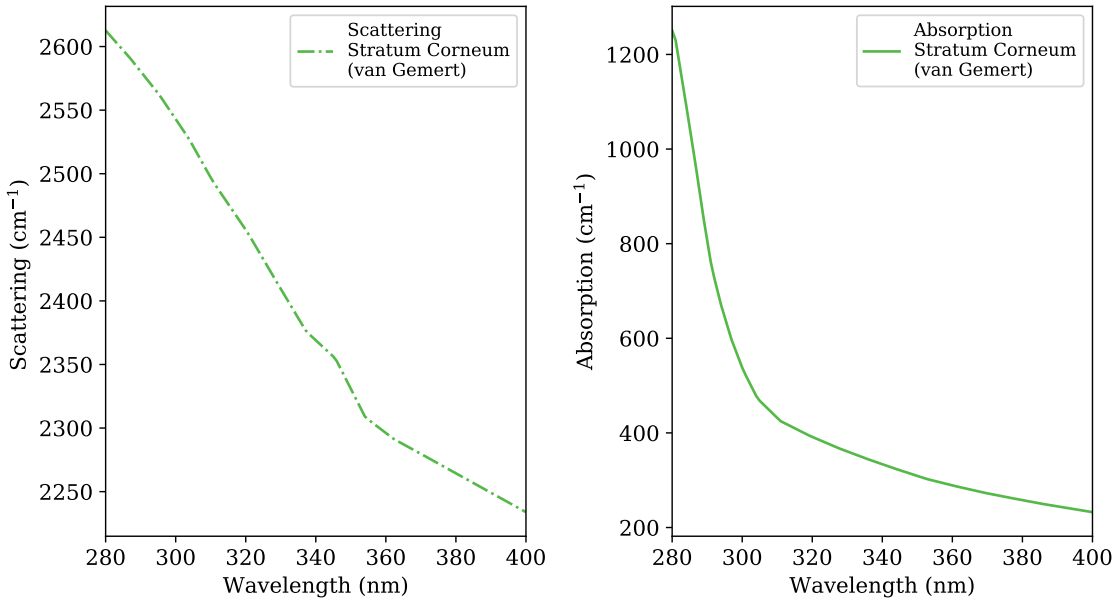

Figure 3.5: *Scattering and absorption coefficients for the stratum corneum, taken directly from van Gemert et al. [38].*

epidermal layer containing no melanin, and a thinner, concentrated melanin layer is sited directly above the basal layer.

Experimental data showing the scattering and absorption coefficients for the epidermis are published by van Gemert et al. (Figures 3.6 and 3.7). The original experimental data were gathered using 'medium complexioned Caucasian skin'.

In order to approximate the absorption coefficient for non exposed epidermis, the contribution of melanin to these experimental data was removed. It was assumed the experimental data described skin with a melanin volume fraction of 4 % (from concentrations described by Karsten et al. [42]). The result is an estimated absorption spectrum for non melanised epidermis, shown in the second panel of Figure 3.7.

Using the depths in Table 3.2, every voxel with a position between the base of the stratum corneum, ($z_{\text{sc}} = 14.8\,\mu\text{m}$) and the base of the non melanised epidermis,

$$z_{\text{epidermis}}(x, y) = z_{\text{base}}(x, y) + 63.7\,\mu\text{m} \tag{3.4}$$

is assigned the absorption coefficient for non melanised epidermis as described above. The scattering properties applied are of the form shown in the first panel of 3.6.

Melanin (layer 3)

The contribution of melanin to the UVR absorption in the epidermis is skin type dependent. In the model, this contribution is calculated and concentrated in the melanin layer. Melanin is the primary chromophore responsible for shielding the DNA-containing basal layer from DNA damage from UVR[51], however research has found that melanin may also act as a sensitiser [52], this is

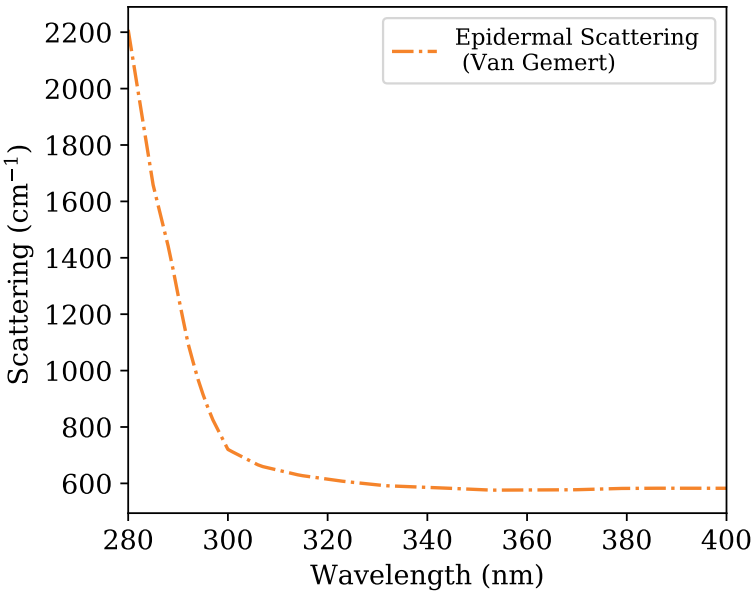

Figure 3.6: *Scattering coefficients for the epidermal, melanin, and basal layers, from van Gemert et al. [38].*

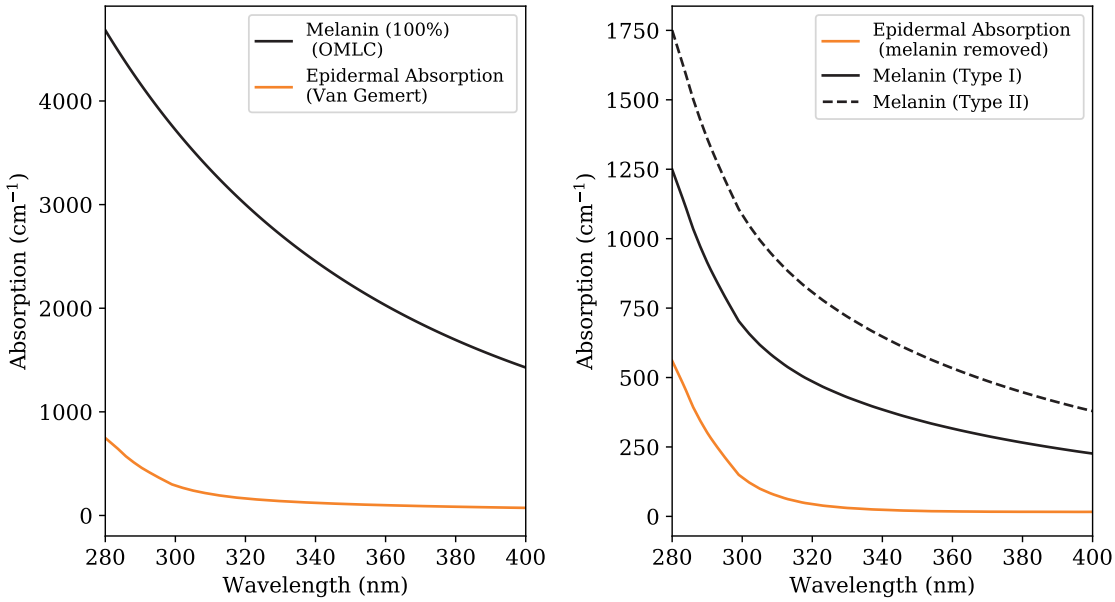

Figure 3.7: *Absorption coefficients for the epidermal & basal layers (van Gemert et al. [38],) and for melanin, from the Oregon Medical Laser Centre (OMLC) [45]. The right panel presents the resulting absorption coefficients for non melanised epidermis and the melanin layer residing above the basal layer.*

discussed further in Chapter 5.

The optical properties resulting from a combination of eumelanin and pheomelanin are described by Equation 3.5 [45],

$$\mu_{\mathrm{a,mel}} = 6.6 \times 10^{11} \lambda^{-3.33} V_{\mathrm{mel}} \tag{3.5}$$

where V_{mel} is the volume fraction of melanin in the skin, wavelength λ is given in nm, and the absorption coefficient of melanin $\mu_{\mathrm{a,mel}}$ is given in cm^{-1}.

The estimated volume fraction of melanin present in the skin ranges from $0-3\,\%$ for skin type I, and from $3-5\,\%$ for skin type II [42, 43, 53]. The midpoint values of $2\,\%$ for skin type I and $4\,\%$ for skin type II were chosen. These values are for melanin concentration across the whole epidermis, so the corresponding absolute volume was calculated and then concentrated within the voxels representing the melanin layer. The resulting absorption due to melanin was added to the non melanised epidermal absorption coefficient to give the absorption for the melanin layer for each skin type, shown in Figure 3.7.

To simulate the distribution of melanin in non exposed skin as a single layer of melanin above the basal layer, each voxel with a position between the base of the epidermal layer $z_{\mathrm{epidermis}}(x, y)$ (Equation 3.4) and the base of the melanin layer $z_{\mathrm{melanin}}(xy)$,

$$z_{\mathrm{melanin}}(x, y) = z_{\mathrm{base}}(x, y) + 73.7\ \mu\mathrm{m} \tag{3.6}$$

is assigned the absorption coefficient for melanised epidermis as described above. These are shown in Figure 3.6. The scattering properties applied are of the form shown in the first panel of 3.6.

Basal layer (layer 4)

The optical properties applied to the basal layer are the same as those applied to non melanised epidermis. In the paper published of this work [32], the basal layer was assumed to contain only DNA, for ease of analysis. However, this did underestimate the optical properties of the basal layer, as there are other chromosomes and scatterers present. In the model described here, optical properties of the basal layer are set equal to those in the epidermis. However, it is important to be able to isolate the basal layer, in order to extract data such as absorbed energy, or fluence. To simulate the basal layer, each voxel with a position between the base of the melanin layer $z_{\mathrm{melanin}}(x, y)$ (Equation 3.6) and the base of the basal layer $z_{\mathrm{basal}}(xy)$,

$$z_{\mathrm{basal}}(x, y) = z_{\mathrm{base}}(x, y) + 83.7\ \mu\mathrm{m} \tag{3.7}$$

is assigned the same properties as assigned to the living epidermis (layer 2).

Dermis (layer 5)

The deepest layer in this model is the dermis. The upper epidermal layers (the stratum corneum, epidermis and melanin) are responsible for the majority of the attenuation of UVR reaching the basal layer. However some UVR reaching the dermis is also scattered back to the basal layer, and as there is no protective melanin at the basal-dermal junction, this represents an important component of the model.

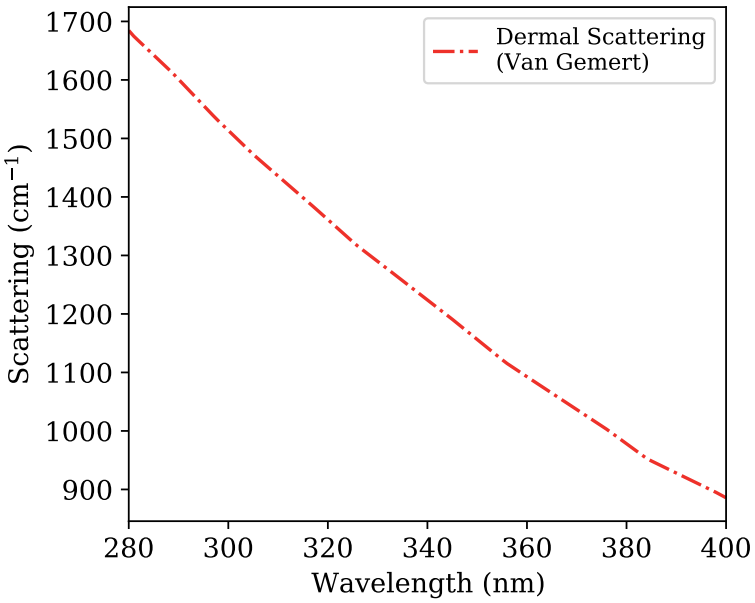

Figure 3.8: *Scattering coefficient $\mu_{\mathrm{s,dermis}}$ for the dermis. The scattering coefficient used and presented here is taken directly from van Gemert et al.[38]. This is not the same as that used in the paper of this work [32], and the coefficient used here is thought to be a better physical description of dermal scattering in the UV.*

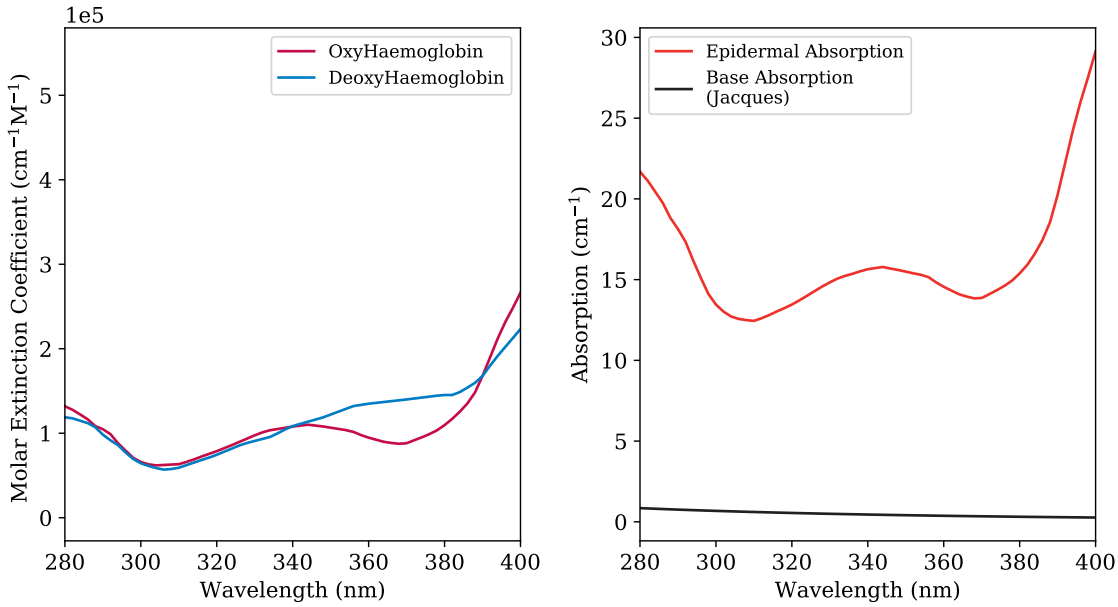

Figure 3.9: *Absorption coefficient $\mu_{\mathrm{a,dermis}}$ for the dermis, including the constituent extinction coefficients for oxyhaemoglobin and deoxyhaemoglobin. Note that the y-scale for the molar extinction coefficients of oxyhaemoglobin and deoxyhaemoglobin is in units of 1×10^5.*

The absorption properties for the dermis are described by Equation 3.8 [45]. This is shown, along with the constituent wavelength dependent components, in Figure 3.9. Here f_{blood} is the fraction of blood present in the skin, wavelengths λ are given in nm, and the absorption coefficient of the dermis $\mu_{\text{a,dermis}}$ is given in cm^{-1}. The coefficients $\mu_{\text{a,hgb}}$ and $\mu_{\text{a,base}}$ take the form described by Equations 3.9 and 3.10 respectively.

$$\mu_{\text{a,dermis}}(\lambda) = f_{\text{blood}}\mu_{\text{a,hgb}}(\lambda) + (1 - f_{\text{blood}})\mu_{\text{base}}(\lambda) \tag{3.8}$$

$$\mu_{\text{a,hgb}}(\lambda) = \frac{C_{\text{hgb}}}{\omega_{\text{hgb}}} \log_e(10) \left(\varepsilon_{\text{a,ohb}}(\lambda) S_{\text{O}_2} + \varepsilon_{\text{a,dhb}}(\lambda)(1 - S_{\text{O}_2})\right) \tag{3.9}$$

$$\mu_{\text{base}}(\lambda) = 7.84 \times 10^7 \times \lambda^{-3.255} \tag{3.10}$$

To determine the absorption coefficient for haemoglobin as used in Equation 3.8, Equation 3.9 is used. This equation includes the absorption A haemoglobin concentration C_{hgb} of $150\,\text{g}\,\text{L}^{-1}$ is used, and the molecular weight of haemoglobin ω_{hgb} is $64458\,\text{g}\,\text{mol}^{-1}$. The oxygen saturation S_{O_2} is assumed to be 75 % in the upper layer of the dermis. The extinction coefficients for both oxy and deoxyhaemoglobin, are taken from Jacques et al. [45] (and are reproduced in the left panel of Figure 3.9). Note that the y-scale in Figure 3.9 is in units of 1×10^5. The background absorption μ_{base} is taken directly from Jacques et al. and shown in the right panel of Figure 3.9; and includes the absorption coefficients of all of the other proteins in blood except haemoglobin.

The resulting dermal absorption coefficient described by Equation 3.8 is shown in the right panel of Figure 3.9. The scattering coefficient is taken directly from van Gemert et al. and is reproduced in Figure 3.8. These optical properties are applied to all voxels with positions below $z_{\text{basal}}(x, y)$ (Equation 3.7).

3.2.4 Summary of optical properties

The resulting grid contains voxels that are both labelled as a given layer, and assigned the optical properties pertaining to that layer. An illustration of the model is shown in Figure 3.10.

Any individual voxel, and the data within, can be extracted. As mentioned in the previous chapter, each voxel also acts as a detector, via the path length counter $\sum_i \Delta s_{i,\lambda}$, which records the wavelength dependent path lengths of the power packets. These can be utilised (using Equations 2.36 and 2.41) to estimate the energy absorbed by a voxel, or the fluence incident on a voxel.

3.3 Irradiation

An advantage of MCRT modelling is that it is possible to simulate irradiation by any source, by simulating the position of the source (and position of the intensity of the source), and the angle of entry of power packets. The source spectra used in the simulations presented within this thesis are application dependent, and as such will be described in each relevant chapter. Across all simulations presented here, the entire skin surface is illuminated with equal intensity. This is done via random sampling of the position of entry of the power packet,

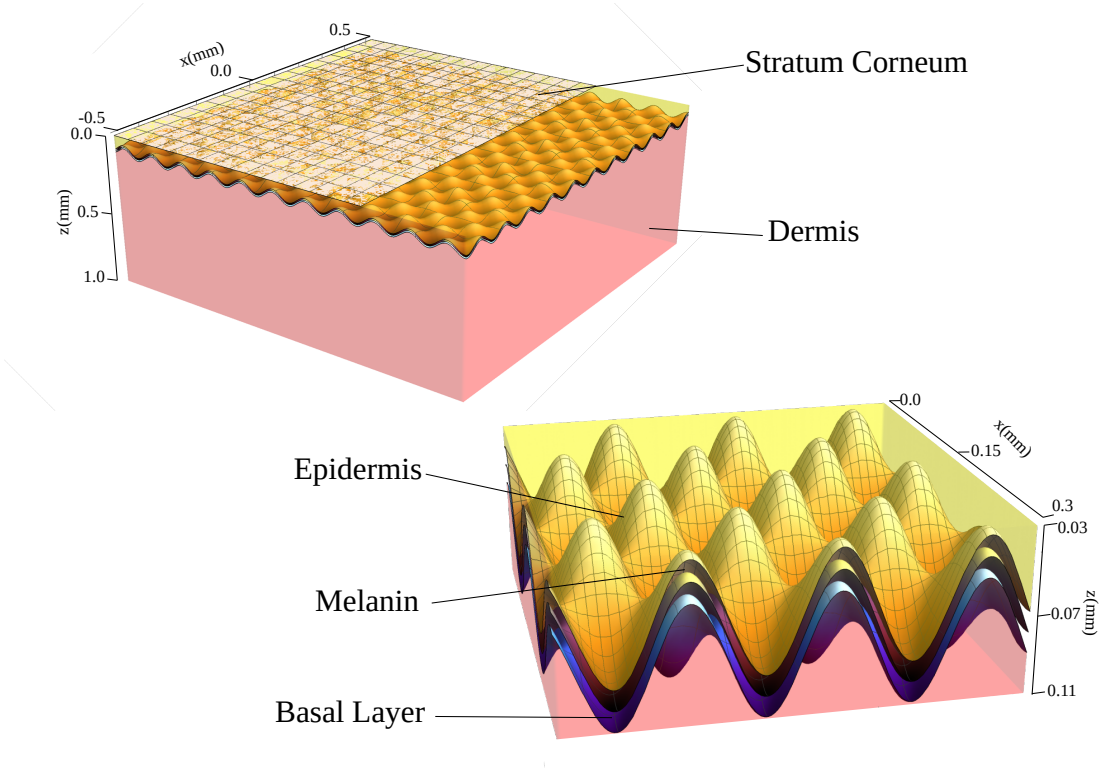

Figure 3.10: *An illustration of the resulting skin model, with layers labelled and size scales shown.*

$$x_{\text{pos}} = x_{\max}(2\xi - 1) \quad 0 < \xi \leq 1.0 \tag{3.11}$$

$$y_{\text{pos}} = y_{\max}(2\xi - 1) \quad 0 < \xi \leq 1.0 \tag{3.12}$$

$$z_{\text{pos}} = z_{\max} - \delta \tag{3.13}$$

Where x_{pos}, y_{pos} and z_{pos} are the spatial coordinates of the position of entry of the power packet, and $x_{\max}$, $y_{\max}$ and $z_{\max}$ the extent of the grid (the grid extends from $-x_{\max}$ to $x_{\max}$, and similarly for y and z). The value δ is a very small round-off value ($(z_{\max}/n_{\text{zcells}}) \times 10^{-6}$), used to ensure the power packet begins the random walk just within the surface of the skin, rather than starting on the discontinuity at the surface. The random number ξ is again from the uniform distribution $U(0, 1)$ to ensure x_{pos} and y_{pos} are independently and randomly sampled.

The model described here is able to simulate the transfer of radiation through an infinite plane of Fitzpatrick Types I & II skin, 1 mm deep. By tracking the progression of individual power packets through the medium, data can be extracted that allows photobiological processes to be simulated. The following chapter describes the application of this model to estimate the DNA damage due to sunbed and solar UVR exposure.

This model, in the main, is used throughout this thesis, with any minor adaptations described within each chapter as required.

Chapter 4

Quantifying direct DNA damage in the basal layer

Synopsis

Both keratinocyte and melanocyte skin cancers are attributable to DNA damage caused by UVR exposure. One DNA photoproduct, the Cyclobutane Pyrimidine Dimer (CPD), is believed to lead to DNA mutations caused by UVR. Using radiative transfer simulations, the number of CPDs directly induced by UVR from artificial and natural UVR sources are compared. Monte Carlo Radiative Transfer (MCRT) modelling was used to track the progression of UV photons through a multi-layered three dimensional (3D) grid that simulates the upper layers of the skin. By recording the energy deposited in the cellular DNA contained within the basal layer, the number of CPDs formed can be estimated. The results indicate that after spending 6 minutes on a commercial sunbed, skin will acquire the same amount as damage acquired during 10 minutes sunbathing in midday, midsummer Mediterranean sun.

4.1 Introduction

4.1.1 Motivation

In the UK, 9/10 sunbeds emit UVR that exceeds current recommended EU limits [54, 55], and there is an increased risk of squamous cell carcinoma (SCC) associated with sunbed use [56]. Given that UVR is a carcinogen (and it is known that UVR induced mutations are found in many skin cancers), and that skin is a turbid medium, it is reasonable to assume that a part of the carcinogenic action of UVR involves the transfer of UVR through the skin. The model developed is used to quantify the yields of direct DNA damage obtained from UVR exposure from both solar radiation and sunbed use.

4.1.2 Sunbeds

Sunbeds are used in the UK mainly for cosmetic tanning [54, 57]. This chapter is concerned only with commercial sunbeds for cosmetic use. Therapeutic UVR units are described in Chapter 7. In past decades there has been debate as to whether sunbed use increases the risk of cancer. Some studies found a causal link [58, 59, 60] while others did not [61, 62]. This debate stemmed from difficulties in elucidating risk attributable solely to sunbed use, as sunbed users were likely to exhibit sun seeking behaviour. However, a recent meta-analysis concluded that sunbed use does increase the risk of developing melanoma [63], though to a lesser extent than some previous estimates.

There is no doubt that sunbed users generally believe that a tan from a sunbed is safer than that from the sun [64, 65, 66] even though evidence to the contrary exists [67]. This myth of a 'safe tan' is still being promoted by the UK Sunbed Association at time of writing [68].

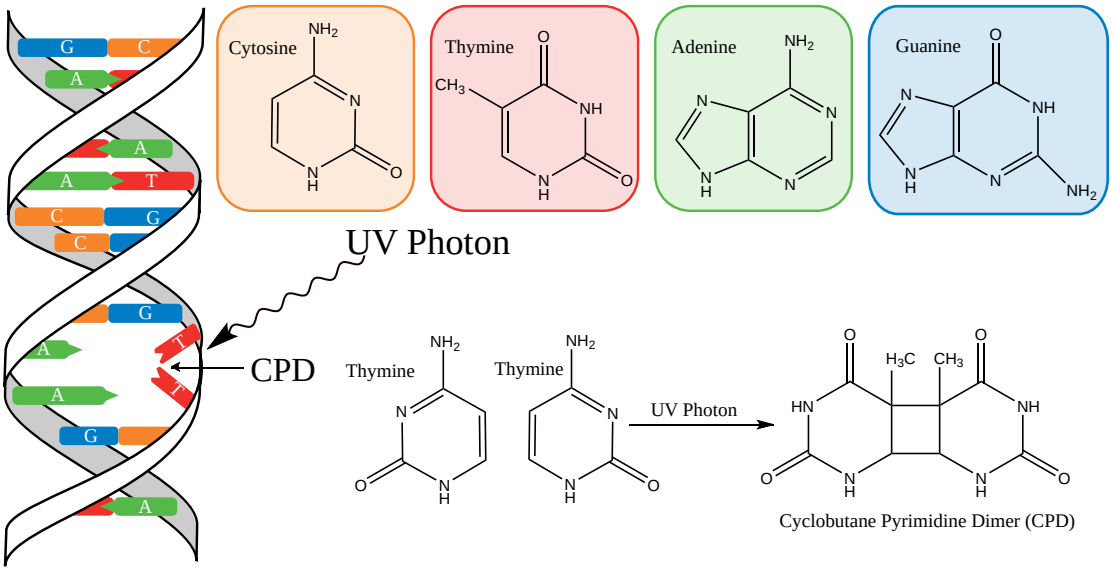

Figure 4.1: *A graphic description of the creation of a cyclobutane pyrimidine dimer (CPD). The top part of the sketch shows a healthy DNA strand, with the bases labelled and colour coded. The bottom half shows a CPD created after two neighbouring thymines are irradiated with a UV photon of sufficient energy. The base pair between the strands breaks, and the thymines bond together as illustrated. This causes the DNA strand itself to become misshapen, and the associated kink within the DNA strand is illustrated. CPDs most commonly occur between neighbouring thymines, however less commonly they can also occur between neighbouring cytosines, or between neighbouring thymine & cytosine bases.*

4.1.3 Photocarcinogensis: UVR and DNA damage

The processes that lead from UVR exposure to skin cancer are known as photocarcinogenesis. Although these are complex, and involve the interplay between various biochemical processes, photocarcinogenic pathways are reasonably well understood [3, 69]. In summary, UVR (directly or indirectly) causes mutations in DNA within skin cells. Eventually, over time, a cell could acquire

enough mutations for cancer to develop. Black et al. [3] state

"*There are three physical dimensions to photocarcinogeneis: dose, time and wavelength*"

To clarify, *'time'* refers to the latent period between UVR exposure and cancer being detected (and can be of the order of decades); whereas *'dose'* describes the total energy received by the skin (power incident on skin × exposure time), where time of exposure could be of the order of seconds to hours, and in the case of repeated doses, months or years).

Many skin cancers are known to be induced by UVR because they carry particular mutations that are not caused by any other known mutagen [69]. These mutations occur when DNA is altered by UV-induced molecular changes, and is then miscopied during the transcription process. These UVR induced molecular changes are known as DNA photoproducts; and involve a conformal (shape change) in the DNA molecule. The most common and numerous photoproducts of DNA are CPDs. Other pyrimidine photoproducts (6-4 PPs, Dewar isomers) are also common, however within this research only the CPD is considered, as these are the most numerous photoproduct produced by both UVA and UVB radiation [70]. In addition, UVR can also form reactive oxygen species (ROS) within the cell, which can cause a cascade of chemical reactions that lead to other types of DNA damage [3, 71]. Yields of both photoproducts and ROS are wavelength dependent [5, 71].

Photoproducts can be produced directly and indirectly. The direct process is illustrated in Figure 4.1; and may be measured *in vivo* by irradiating skin, then immediately taking skin samples and analysing them. Photoproducts can also be produced indirectly. Recent research has shown CPDs form after exposure to UVR has ceased in both melanin rich melanocytes [52] and in keratinocytes containing no melanin [72]. These are known as 'dark CPDs' and can contribute up to half of the total CPD yield observed in melanocytes [52].

It is important to note that until recently, UVB was considered to be responsible for direct DNA damage (and by extension cancer), and UVA was responsible for ROS (and by extension, photoageing). Recent research has found this is not the case [70]. Although UVA induces fewer CPDs than UVB by orders of magnitude, UVA does produce CPD. The UVA induced CPDs are not only experimentally detectable [5] but are the most numerous photoproduct produced by UVA [70]. Given that both sunbeds and the sun are primarily UVA sources (and UVA penetrates deeper into tissue than UVB), UVA induced CPDs must not be neglected as a contributor to the carcinogenic burden.

Although the formation of UV-induced DNA photoproducts is very common (on average each skin cell forms 50-100 photoproducts per second of sunlight exposure [73]), most occurrences are corrected by cell repair processes (base excision repair or nucleotide excision repair [73, 74]). If damage cannot be repaired, the cell may initiate apoptosis (controlled cell death).

If damaged DNA is not repaired, and a mutation occurs, this may have serious consequences, or no effect at all. The outcome depends on the location of the mutation, both within the skin structure, and on a genomic level. For example, 90 % of SCC tumours examined in the USA were found to contain p53 mutations [3]. P53 is known colloquially as 'the caretaker of the cell' and 'the guardian of the genome', and one role of p53 is to initiate controlled cell death should the cell become damaged, or if cell growth is out of control [69, 75].

Location of DNA damage within the skin

In healthy skin, the basal layer is the keratinocyte stem cell layer, where new cells are produced. Most of these cells leave the basal layer and move towards the surface (terminal differentiation), and eventually form the stratum corneum, which is then shed. This is important because although the cells in this upper epidermal layer do acquire DNA damage [76], it is unlikely to have serious consequences, as the cells in the epidermis are already committed to terminal differentiation [5, 50].

In contrast, DNA damage affecting the cells in the basal layer is potentially dangerous. The basal layer of the skin can accumulate enough DNA damage to lead to cancer [50]; and as such the basal layer is the focus of our analysis.

In summary, UVR (directly or indirectly) induces conformal changes to the DNA molecule. These are likely to be repaired. If they are not, this conformal change may result in a mutation. If this mutation occurs within a gene responsible for tumour control, and if this occurs within a cell located within the basal (stem cell) layer of cells, then this mutation will be passed on to daughter cells. Eventually, over time, a cell could acquire enough mutations for cancer to develop.

4.2 Methods

Most MCRT simulations described in this thesis use the model described here, and most of the subsequent research presented in this thesis was motivated by the research undertaken in developing this model. The aim is to quantify the risks of direct DNA damage caused by irradiation from a typical UK sunbed. It is not possible to use the MCRT model as described to quantify such risk in absolute terms. Unlike with ionising radiation (where the SI units of Sieverts quantify the probability that a given dose of ionising radiation will have long lasting health effects), there is no method or unit to quantify the long term health risks associated with a given amount of DNA damage.

However, long term health risks of solar exposure are well characterised [56]. Given this, the risk of direct DNA damage caused by irradiation from a sunbed are presented in terms of the risk of DNA damage caused by exposure to solar irradiation.

In order to quantify the amount of DNA damage caused by sunbed and solar irradiation, the code as described in Chapter 3 is applied here to simulate the transfer of UVR to the basal layer.

Once the transfer of UVR from the sunbed and solar sources is quantified, these data are analysed to estimate the relative risk of DNA damage from both sources.

4.2.1 MCRT simulation

4.2.2 Radiation sources

Sunbed

To quantify the DNA damage caused by a typical UK sunbed, a suitable spectrum was selected from data collected during previous research [54, 55]. This is shown in Figure 4.2. Each power packet has a wavelength randomly selected from this spectrum using the numerical approximation to the inverse transform method. The sunbed is considered a purely diffuse source, and as such, the

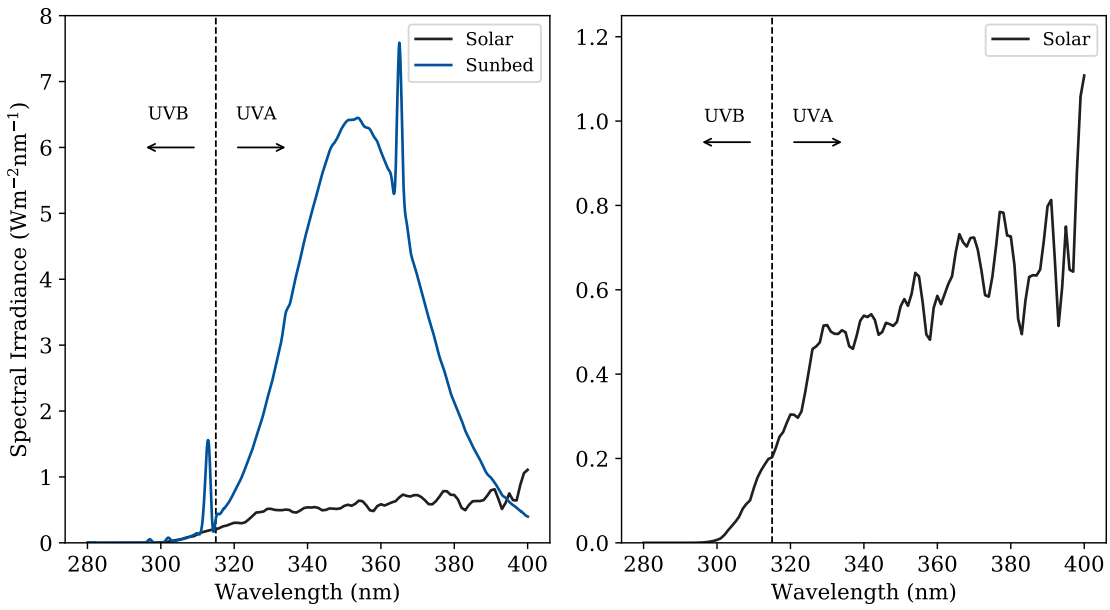

Figure 4.2: *The spectra of the radiation sources under investigation in this chapter are shown here; with division between the UVB (280 nm to 315 nm) and UVA (315 nm to 400 nm) bands marked. The left panel compares the UVR solar spectrum with a typical sunbed [54] (where the spikes indicate characteristic mercury emission lines: mercury lamps are commonly used in commercial sunbeds). The right panel shows this solar spectrum alone. This spectrum was recorded at midday during a cloudless day in July in Thessaloniki in Greece using ground-based instrumentation [14, 56]. The solar spectrum has a total irradiance of 50.5 Wm^{-2} (comprising 1.4 Wm^{-2} of UVB and 49.1 Wm^{-2} UVA). The sunbed spectrum has a total irradiance of 283.7 Wm^{-2} (comprising 3.26 Wm^{-2} of UVB and 280.2 Wm^{-2} UVA).*

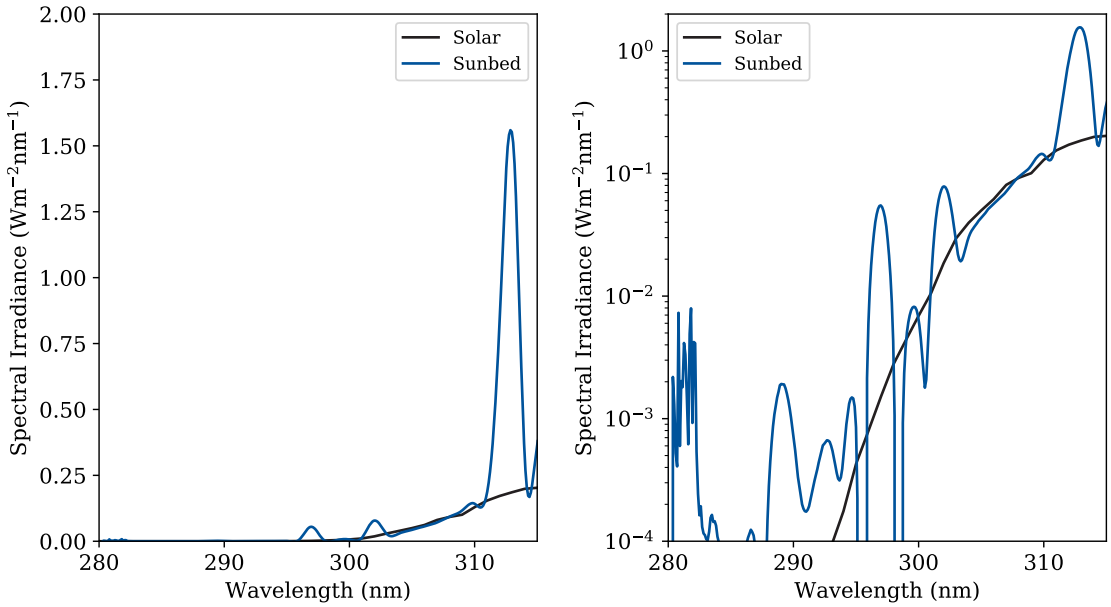

Figure 4.3: *The UVB spectra of the radiation sources under investigation in this chapter are shown here; with the right panel showing the data on a log scale in order to highlight the small amounts of UVB radiation emitted by the sunbed.*

position of entry was uniformly distributed across the surface of the grid, and the direction of entry to the grid was randomly sampled from an isotropic distribution,

$$\theta_{\text{sunbed}} = \cos^{-1}(-\xi) \quad 0 < \xi \leq 1.0 \tag{4.1}$$

where, as before, ξ is randomly sampled from the uniform distribution $U(0, 1)$.

Solar

An example of intense solar radiation was selected as a suitable comparison to the sunbed. A solar spectrum from a cloudless day in July at midday in Thessaloniki, Greece was chosen [14, 56] (Figure 4.2). Each power packet has a wavelength randomly selected from this spectrum using the method described in the introduction. The solar spectrum comprises a mix of direct and diffuse components determined by the date, time, and the location on earth where the spectrum was recorded. These are approximated by the clear sky model by Bird et al. [77, 78] as comprising 13% diffuse and 87% direct radiation. As such the direction of entry to the grid is randomly sampled using Equation 4.2.

$$\theta_{\text{solar}} = \begin{cases} \cos^{-1}(-\xi) & \text{if } 0 < \xi' \leq 0.13 \\ \pi & \text{if } 0.13 < \xi' \leq 1.0 \end{cases} \tag{4.2}$$

where, as before, ξ is randomly sampled from the uniform distribution $U(0, 1)$. In Equation 4.2, ξ' is used to select whether the power packet is diffuse or direct. If it is diffuse, a different random number ξ is selected to randomly determine the diffuse direction of entry.

The MCRT model as described in Chapter 3 was built in order to simulate irradiation from a sunbed and from the solar source as described above. Each simulation was performed for Fitzpatrick skin types I & II; making 8 MCRT simulations in total. Each simulation was run with 10^8 power packets. The MCRT model allows recovery of the spectrally resolved fluence in all the voxels in the model. Using the path length counters and the absorption coefficient of each layer, the power absorbed can be calculated.

In analysing the data developing this simulation, it is assumed that a significant part of the process of CPD formation is reducible to 'radiation transfer', and that the resulting biochemistry can be deduced from quantifying the amount of radiation reaching the basal layer.

The spectrally resolved fluence in the basal layer can be found via,

$$\psi(\lambda) = \frac{1}{N_{\text{basal}}} \sum_{i,j,k} \psi_{i,j,k}(\lambda) \text{ for } i,j,k \in \text{basal layer} \tag{4.3}$$

where $\psi_{i,j,k}$ is the fluence at voxel of index $\{i,j,k\}$ within the basal layer (and N_{basal} the number of voxels within the basal layer).

4.2.3 CPD yields

The aim is to quantify the DNA damage induced by UVR reaching the basal layer. CPDs are often found within signature mutations in UVR induced keratinocyte skin cancers (SCCs and BCCs) that are linked to lifetime cumulative UVR exposure, and as such the CPD yield was chosen as an indicator for DNA damage. Two approaches to calculating CPD formation in the basal layer are detailed here. One approach, described as 'band yield', is the same as was used in the paper published on this work [32]. This approach assumes that the CPD yields can be assigned to UVR bands (e.g. assume one CPD yield for UVA, and one for UVB). The second approach, taken subsequent to publication of reference [32] better represents the yield of UVR induced CPDs by utilising a spectra (CPD yield within DNA vs. wavelength), and is described as 'spectral yield'.

4.2.4 Band yields

The basal layer contains DNA, which is a strong absorber of UVB radiation, as indicated in Figure 4.4. The extinction coefficient spectrum of oligomeric duplex dA20:dT20 has previously been used to determine photodamage in DNA [79] and is used here as an approximation for the absorption coefficient of the DNA contained within cells. The concentration of DNA within the epidermal and basal layers is estimated using a volumetric method adapted from Mohlenhoff et al. [80]. Using the number of bases per human diploid cell (12.8 billion bases) along with average cell sizes for cells in the basal layer and epidermis (on average 13 μm and 20 μm respectively [81]), cells in the epidermal layer are estimated to have a DNA concentration of approximately 0.005 moles per litre, and those in the basal layer to have a DNA concentration of 0.018 moles per litre. Equation 4.4 is used to combine these concentrations with the extinction coefficient ε_{DNA} taken from Mouret et al. [79] to retrieve the absorption coefficient, as shown in 4.4.

$$\mu_{\text{a,dna}}(\lambda) = \log_e(10)\varepsilon_{\text{DNA}}(\lambda)C_{\text{DNA}} \tag{4.4}$$

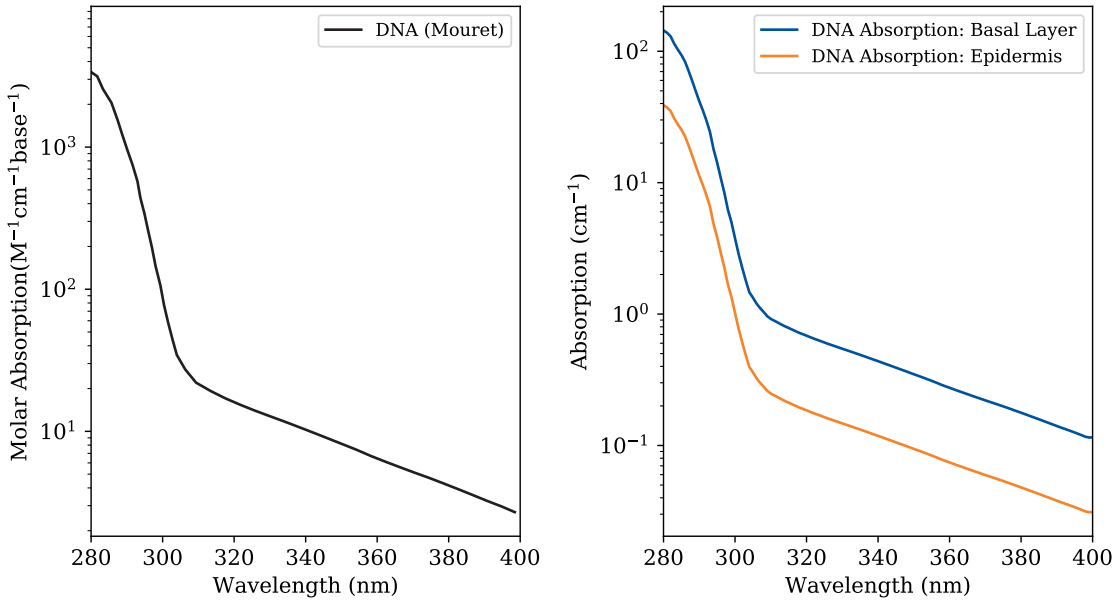

Figure 4.4: *The DNA molar absorption coefficient reproduced from Mouret et al. [79]; and the DNA absorption coefficients for the epidermis and dermis estimated using the method described by Molenhoff et al. assuming a DNA concentration of 0.018 M for the basal layer and 0.005 M for the epidermis, and using Equation 4.4.*

Using this absorption coefficient; the energy absorbed by DNA in the basal layer can be extracted using Equation 4.5,

$$E_{\mathrm{DNA},\lambda} = \frac{1}{N_{\mathrm{basal}}} \sum_{i,j,k} \mu_{\mathrm{a,DNA}} \psi_{i,j,k}(\lambda) \text{ for } i,j,k \in \text{basal layer} \tag{4.5}$$

For a photobiological process, such as CPD formation, the efficiency of the process can be described by the quantum yield ϕ given by Equation 4.6 where N_{process} is the number of photons causing the biological effect, and $N_{absorbed}$ is the number of absorbed photons; giving the proportion of effect to amount absorbed,

$$\phi = \frac{N_{\mathrm{process}}}{N_{\mathrm{absorbed}}} \tag{4.6}$$

Banyasz et al. demonstrated quantum yields for CPD formation to be $\phi_{\mathrm{UVB}} = 0.05$ and $\phi_{\mathrm{UVA}} = 0.0005$ [82].

As stated in the derivation of the RTE (Chapter 1), the number of photons absorbed is directly proportional to the energy lost during radiative transfer due to absorption. Thus considered in the frame of reference of the absorbing chromophore, the number of photons absorbed by a chromophore N_{absorbed} is directly proportional to the energy absorbed by that chromophore E_{DNA} .

As previously stated, to quantify the additional risk to human health due to sunbed use, the CPDs formed due to sunbed irradiation are expressed as a proportion of those absorbed due to solar irradiation, (as risks to health from solar irradiation are well characterised [56]) as shown in

Equations 4.8 - 4.9, where $E = E_{\mathrm{DNA}}$,

$$\left(\frac{\mathrm{CPD}_{\mathrm{sunbed}}}{\mathrm{CPD}_{\mathrm{solar}}}\right)_{\mathrm{UVB}} = \frac{\sum_{i,j,k}\sum_{\lambda=280}^{315} E_{i,j,k,\mathrm{sunbed}}(\lambda)}{\sum_{i,j,k}\sum_{\lambda=280}^{315} E_{i,j,k,\mathrm{solar}}} \text{ for } i,j,k \in \text{basal layer} \tag{4.7}$$

$$\left(\frac{\mathrm{CPD}_{\mathrm{sunbed}}}{\mathrm{CPD}_{\mathrm{solar}}}\right)_{\mathrm{UVA}} = \frac{\sum_{i,j,k}\sum_{\lambda=315}^{400} E_{i,j,k,\mathrm{sunbed}}(\lambda)}{\sum_{i,j,k}\sum_{\lambda=315}^{400} E_{i,j,k,\mathrm{solar}}} \text{ for } i,j,k \in \text{basal layer} \tag{4.8}$$

$$\left(\frac{\mathrm{CPD}_{\mathrm{sunbed}}}{\mathrm{CPD}_{\mathrm{solar}}}\right)_{\mathrm{total}} = 0.05\left(\frac{\mathrm{CPD}_{\mathrm{sunbed}}}{\mathrm{CPD}_{\mathrm{solar}}}\right)_{\mathrm{UVB}} + 0.0005\left(\frac{\mathrm{CPD}_{\mathrm{sunbed}}}{\mathrm{CPD}_{\mathrm{solar}}}\right)_{\mathrm{UVA}} \tag{4.9}$$

4.2.5 Spectral yields

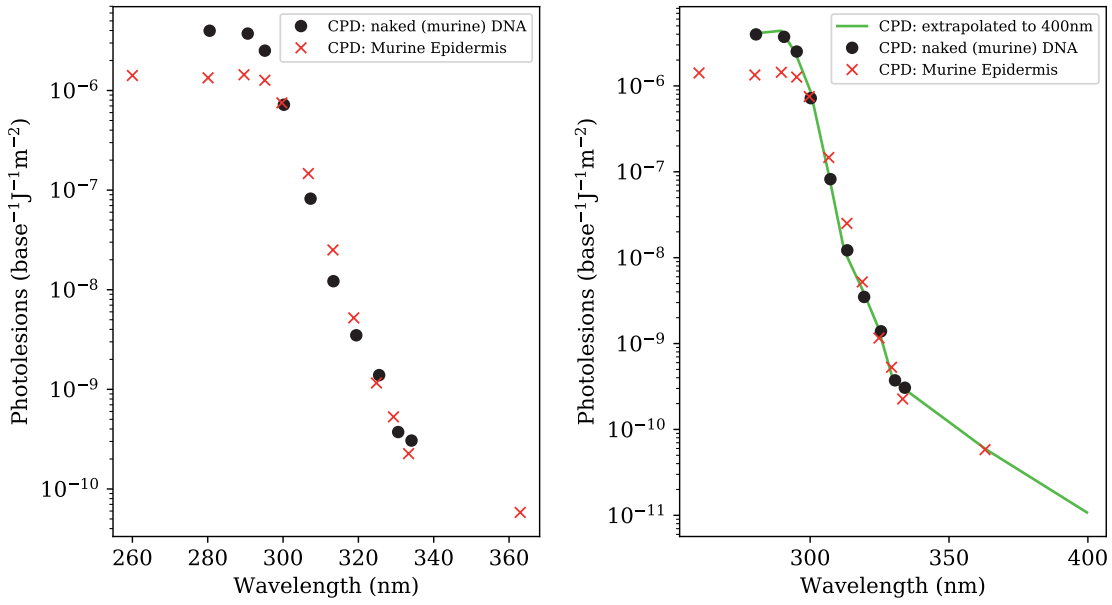

Figure 4.5: *The left shows the data published by Ikehata et al. [83] showing both CPD in naked murine DNA and CPD in the murine epidermis. As is shown, the naked DNA and epidermal results overlap after about 300 nm. As the dataset for naked DNA stops at 335 nm, the right panel shows an extrapolation to 400 nm using the epidermal CPD data between 335 nm and 360 nm.*

Figure 4.5 shows data published in late 2019 [83] showing a clear wavelength dependence on CPD yield within both naked DNA and layers within murine skin. Although the epidermal and dermal data may not be comparable to human skin, as murine epidermis is only2-3 cells layers thick, the naked DNA data is suitable (murine and human DNA would be expected to behave similarly to irradiation with UVR). The method followed here to differentiate DNA concentrations in the basal layer and epidermis is the same as described in the previous section. The second panel of Figure 4.5

extrapolates the naked DNA data set published by Ikehata et al. [83] to 400 nm; allowing it to be used within Equation 4.10.

$$\left(\frac{\mathrm{CPD}_{\mathrm{sunbed}}}{\mathrm{CPD}_{\mathrm{solar}}}\right)_{\lambda_1-\lambda_2} = \frac{\sum_{\lambda=\lambda_1}^{\lambda_2} \sum_{i,j,k} A_{\mathrm{CPD}}(\lambda)\psi_{i,j,k,\mathrm{sunbed}}(\lambda)}{\sum_{\lambda=\lambda_1}^{\lambda_2} \sum_{i,j,k} A_{\mathrm{CPD}}(\lambda)\psi_{i,j,k,\mathrm{solar}}(\lambda)} \text{ for } i,j,k \in \text{basal layer} \tag{4.10}$$

where $\psi_{i,j,k}$ is the fluence at voxel of index $\{i,j,k\}$, and A_{CPD} the extrapolated action spectra from the second panel in Figure 4.5. UVB yields are calculated by setting $\lambda_1 = 280$ nm and $\lambda_2 = 315$ nm, and UVA yields by setting $\lambda_1 = 315$ nm and $\lambda_2 = 400$ nm.

The data extracted from the model were used to calculate the CPD yield using both methods described above; and the methods were compared.

4.3 Results

The raw data produced by each of the simulations comprised a 4-D dataset, a hypercube comprising 3 spatial dimensions; x, y and z, each discretised onto a grid; and one wavelength dimension discretised into 121 bins 1 nm wide, comprising the UVB & UVA wavebands. Each dataset contained 121×10^6 data points (121 points for each of the 1×10^6 voxels).

Thus each voxel contains a wavelength resolved estimator of the radiation reaching that voxel, obtained using the path length counter method (Equations 2.37 and 2.41).

4.3.1 Radiation transfer

Figure 4.6 shows maps detailing the total number of absorbed photons per second through a central slice of the 3D grid for both the Mediterranean sun and the sunbed for skin type I and skin type II.

Figure 4.7 shows the fluence incident on the basal layer for both skin types and both radiation sources. The data are extracted from the main dataset using Equation 4.3. Figure 4.8 shows the same data as that presented in Figure 4.7; along with the incident spectra. The data in Figure 4.8 are normalised to show the difference in shape between the spectrum incident on the skin surface, and that incident on the basal layer.

UVR band	Basal (Type I)		Basal (Type II)	
	UVB	UVA	UVB	UVA
Solar	17.7%	57.9%	12.6%	43.4%
Sunbed	12.3%	39.7%	8.5%	29.2%

Table 4.1: *This table gives the proportion of incident radiation within each band reaching the basal layer for skin types I & II, for both solar and sunbed irradiation.*

Table 4.1 presents the proportions of the incident UVA and UVB from both sources reaching the basal layer in both skin types.

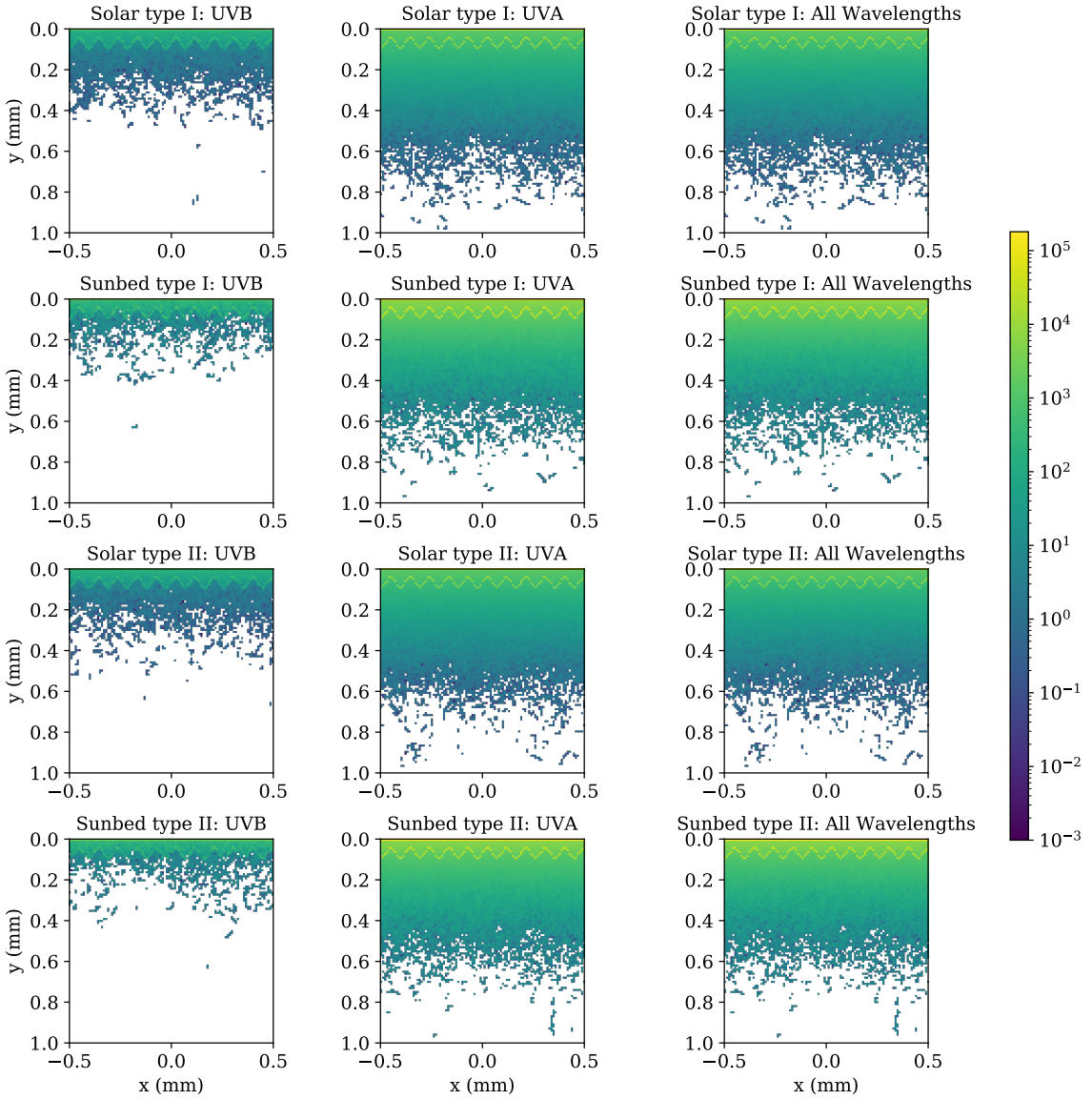

Figure 4.6: *Maps of energy deposited in the central slice of the model in terms of Jcm^{-3}. Both skin types are presented, and the maps have also been divided into the UVB and UVA. The plots have been standardised to the same colour bar. The top of each map shows a bright flat layer, indicating the expected strong absorption in the stratum corneum. The bright sinusoidal layer indicates high absorption in the melanin layer. The empty voxels at the bottom of the grid indicate no packets have penetrated that far, and as such, the depth chosen was adequate to capture any back scatter from the dermis.*

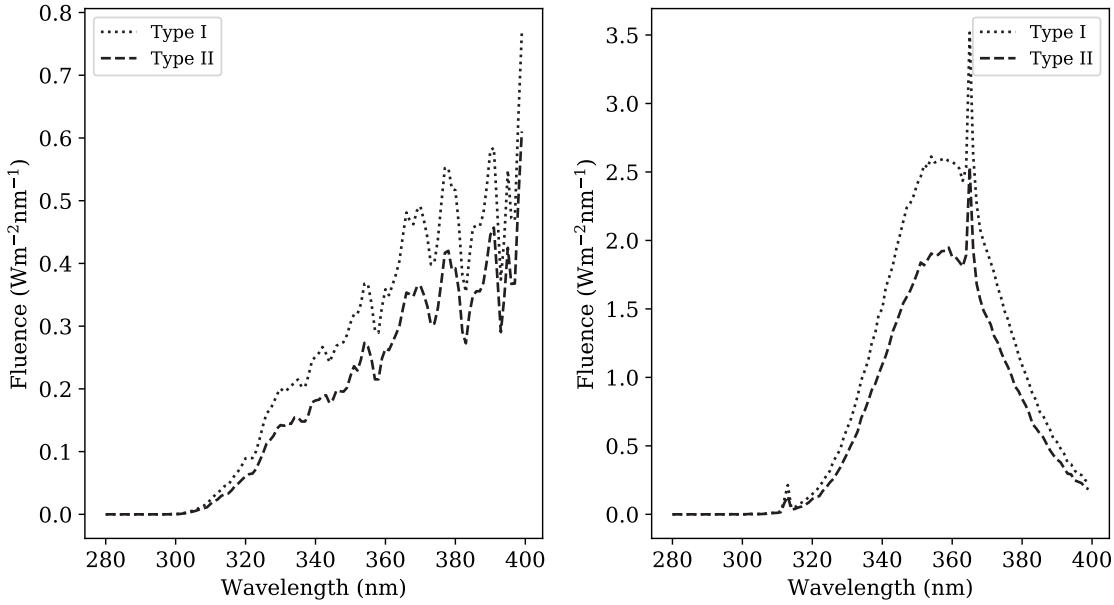

Figure 4.7: *Radiation incident on the basal layer for the solar and sunbed simulations. The data presented here are extracted from the main dataset using Equation 4.3. The proportions of UVA and UVB radiation reaching the basal layer are presented in Table 4.1.*

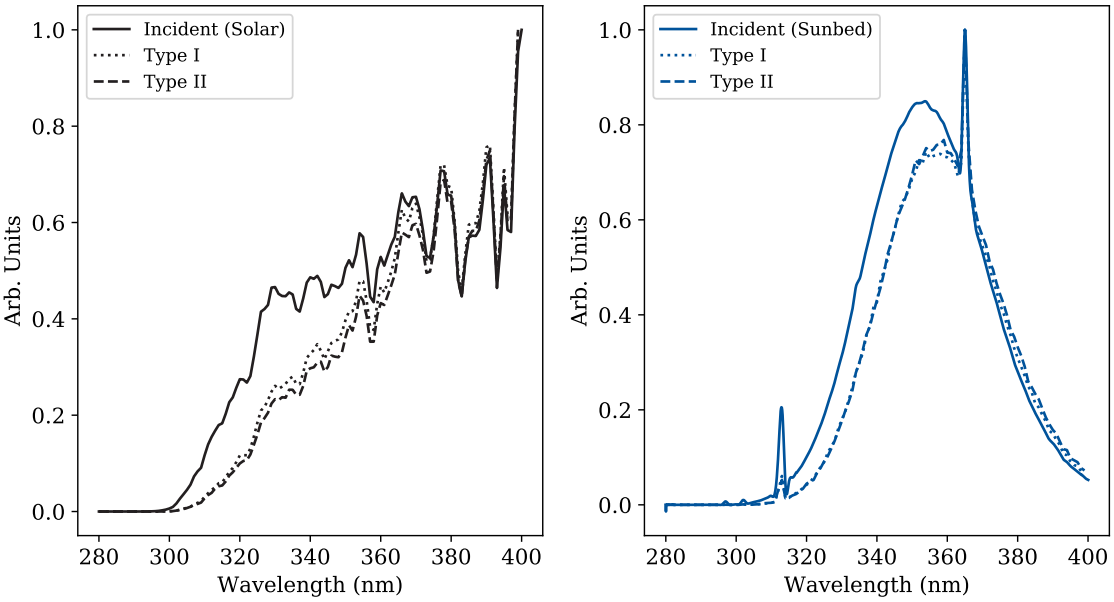

Figure 4.8: *Radiation incident on the basal layer for the solar and sunbed simulations, with the source spectra, normalised to show how the spectral shape has changed after passing through the upper layers of the skin.*

4.3.2 CPD yields

The results from applying Equations 4.8-4.9 on the retrieved data are presented in Table 4.2.

UVR Band	Band yield		Spectral yield	
	Skin Type I CPDs $^{\text{sunbed}}/_{\text{solar}}$	Skin Type II CPDs $^{\text{sunbed}}/_{\text{solar}}$	Skin Type I CPDs $^{\text{sunbed}}/_{\text{solar}}$	Skin Type II CPDs $^{\text{sunbed}}/_{\text{solar}}$
UVA	4.53	4.49	3.22	3.23
UVB	1.77	1.73	1.05	1.03
Total	3.89	3.86	1.68	1.67

Table 4.2: *Proportions of CPDs formed within the basal layer with respect to skin type and UVR band. The number of CPDs formed by the sunbed is expressed as a fraction of those formed by the Mediterranean sun. Methods used to calculate the CPD yields as described in the main text. Band yield describes the method used in previously published work [32], and spectral yield is obtained using Equation 4.10.*

UVR Band	Band yield		Spectral yield	
	Skin Type I CPDs $^{\text{UVA}}/_{\text{UVB}}$	Skin Type II CPDs $^{\text{UVA}}/_{\text{UVB}}$	Skin Type I CPDs $^{\text{UVA}}/_{\text{UVB}}$	Skin Type II CPDs $^{\text{UVA}}/_{\text{UVB}}$
Solar	3.28	3.41	0.41	0.41
Sunbed	8.40	3.28	1.24	1.30

Table 4.3: *Proportions of CPDs formed within the basal layer with respect to skin type and UVR Band. The spectral yield results are in line with what is expected; where the majority of solar DNA damage is caused by UVB radiation.*

Tables 4.2 and 4.3 give the proportions of CPD formed within the basal layer with respect to skin type, UVR band, and radiation source. In Table 4.2, the number of CPD formed under sunbed irradiation is expressed as fraction of those formed under solar irradiation. In Table 4.3 the number of CPD formed by the UVA component of the incident radiation is expressed as a fraction of those formed by the UVB component of the incident irradiation.

Figure 4.9 compares both methods used to estimate the CPD yield to published experimental CPD yields [5].

4.4 Discussion

4.4.1 Radiation transfer

Figure 4.6 shows maps detailing the total number of absorbed photons per second through a central slice of the 3D grid for both the Mediterranean sun and the sunbed for skin type I and skin type II. The maps clearly show the high absorption by melanin residing above the basal layer; and that more photons are absorbed by the grid simulating sunbed irradiation. This is expected, as the incident irradiance from the sunbed is higher than that for solar.

Figure 4.6 also shows for all of the simulations performed, the energy absorbed by the dermis drops off with depth into the dermis, indicating that some UVR penetrates deeper than the basal

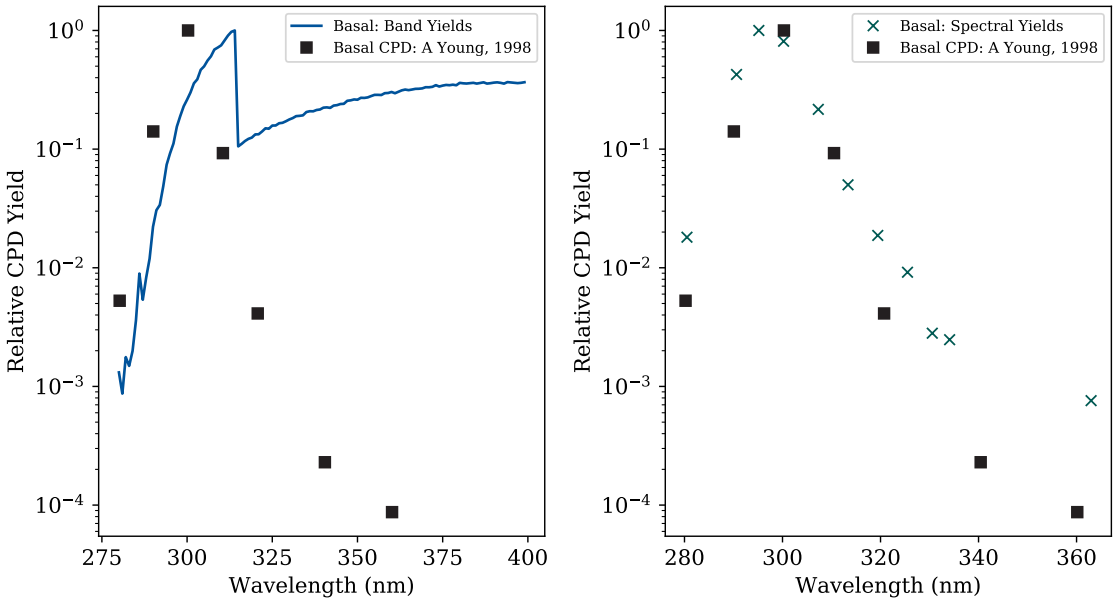

Figure 4.9: *The black dots on both panels represent experimental results from Young et al. [5]. The experimental results shown involved some normalisation of input radiation, and as such, to compare these, new simulations were performed using an input spectrum with uniform irradiance across all wavelengths. The left pane shows the 'band yield' method, and the right panel shows the 'spectral yield' method as described in the text.*

layer, scattering repeatedly until absorbed. Figure 4.6 shows that for every simulation, the base of the grid has recorded no fluence. This indicates that the geometry chosen to represent the depth of the dermis was adequate to capture the physics of UVR transport within the upper layers of the skin.

Figure 4.7 shows the fluence incident on the basal layer for both skin types and both radiation sources. The data are extracted from the main dataset using Equation 4.3. As expected, the plots show the shielding effect of melanin is more pronounced for skin type II. Figure 4.8 compares the shape of the spectrum incident on the basal layer in both skin types compared to the shape of the incident spectrum. Figure 4.8 clearly illustrates that the shorter wavelengths are filtered relative to the longer UVA wavelengths. There is little to distinguish the shape of the spectra incident on the basal layer between the different skin types.

Table 4.1 details the proportion of each band of incident radiation that reaches the basal layer. In skin type II, the proportions of incident radiation from both bands is more greatly reduced than in skin type I, thus demonstrating the shielding effects of the melanin.

For both sunbed and solar irradiation, for both skin types, Table 4.1 demonstrates the shielding effects of the upper layers of the epidermis offer preferential protection against UVB compared to UVA.

4.4.2 CPD yields

Table 4.2 presents the CPD formed from sunbed irradiation as a proportion of those from solar irradiation. Comparing both bands, there is no significant difference between proportions for skin types I & II, indicating that skin type does not afford a relative increase in protection. The 'band yield' method suggests that for both skin types, the sunbed induces about 3.9 times more CPD than Mediterranean midday sun. The 'spectral yield' method suggests that for both skin types, the sunbed induces about 1.7 times more CPD than Mediterranean midday sun.

Table 4.3 compares the CPD induced by UVA to the CPD induced by UVB. The band yield method suggests, across all sources and skin types, that the majority of CPD are induced by UVA radiation. This method suggests that for skin type II, for both sources, about 3 times as many CPD are induced by UVA radiation compared to UVB. However for skin type I, the ratio is much higher for the sunbed; where results indicate that the UVA present in the sunbed is responsible for 8 times as many CPD as induced by the UVB component.

However, the results for spectral yield indicate that there is a similar proportion of CPD induced by UVA compared to UVB across both skin types. The spectral yield method agrees with the band yield method in that it suggests the majority of CPD induced by sunbeds are due to UVA radiation. However the spectral yield method differs from the band yield method in that it suggests that the majority of CPD induced by solar radiation are due to the UVB component. This is in line with accepted thinking, where UVA is thought to be responsible for a significant number of CPD, but not the majority [79]. Woollons et al. [84] found that the majority of CPD found in human keratinocytes were induced by the UVB content of a UVA sunlamp; however; this study was conducted *in vitro* and as such the findings in reference [84] cannot be directly translated across to *in vivo*, where epidermal shielding affects the spectrum reaching the basal layer.

Using both methods, the results Table 4.3 indicate that UVA radiation is responsible for the majority of CPDs formed in the basal layer from sunbed use. This is an important finding, as for a long time, due to the relatively small likelihood of CPD formation due to UVA radiation (see Equation 4.6 and Figure 4.5) UVA was not considered a relevant factor in carcinogenic potential. In fact, in experiments with mice, Ikehata et al. have found that the most mutagenic CPD lesions (the CPD most likely to lead to an actual mutation) peaks at about 313 nm; with significant mutagenicity either side of this boundary [83]. This adds weight to the argument that UVA should not be neglected as a contributor to carcinogenisis. The fact that UVA is responsible for the majority of CPD induced by sunbed irraditaton is a combination of non zero likelihood of CPD formation by UVA, and the greatly increased penetration ability of the UVA component of incident radiation (Table 4.1).

Comparison of Table 4.1 and Table 4.2 highlights the importance of calculating CPD yields, as relying on radiation reaching the basal layer is not enough to reach a conclusion about potential risks of DNA damage. For example, in skin type I, for solar radiation, the majority of the incident UVA radiation (57.9%) reaches the basal layer. Using this, the conclusion might be reached that solar radiation was more dangerous. However, using both methods, Table 4.2 indicates that proportionally, sunbed radiation induces more CPD.

If the risk of DNA damage from sunbed use for one skin type can be deduced from the ratio between the number of CPDs formed due to sunbed exposure to the number formed due to solar exposure, then Tables 4.2 indicates that for both skin types, the additional risk is almost equal;

despite skin type II containing twice as much melanin [18, 42].

4.4.3 Justification of spectral yield

It is likely the 'band yield' method, as used in reference [32], overestimates the UVA induced CPD yield (see Figure 4.9). This is because both the sunbed and solar radiation are primarily UVA sources; and using the method described above, the same CPD yield is applied for 320 nm as applied at 399 nm.

Experimental work by Young et al. [5] recovered CPD yields at different depths *in vivo*. Measuring CPD *in vivo* can be confounded by indirect CPDs and DNA repair processes; however the experimental protocol reported in Young et al. [5] is likely to be reporting mostly directly induced CPD. The experimental results published for CPD yield in the basal layer are reproduced in Figure 4.9.

These are compared to results from new simulations performed using a UVR input spectra of uniform irradiance between 280 nm and 400 nm. This was chosen as to simulate the experiment, which was performed using monochromatic UVR. It is clear that from the comparisons in Figure 4.9 that the spectral yield method is a better fit to experimental results. Though both methods reproduce the experimental CPD formation well up to about 300 nm; the data obtained by the 'band yield' diverges considerably from experimental results when wavelengths are greater than 320 nm.

However, as Figure 4.9 shows, the spectral yield method starts to diverge from experimental results at about 330 nm, and as such may overestimate the CPD yield due to UVA radiation (though not as dramatically as shown by the band yield method). One possible reason for this may be that the simulations performed to produce the results in Figure 4.9 did not reproduce the experimental protocol exactly. The experimental protocol used a monochromator; which are not truly monochromatic and produce radiation with a small but non zero bandwidth. However this is unlikely to be responsible for the divergence seen in the left panel of Figure 4.9. Given that CPD yield decreases with increasing wavelength (Figure 4.5), it is reasonable to assume that the experimental results would over-report CPD rather than under-report (due to the non-zero amount of shorter wavelength radiation present in the monochromatic beam). The divergence is unlikely to be due to repair processes having already started, as repair of CPD is slow. However, again, the experimental protocol was designed to prevent this. One possible explanation is that in the naked CPD results from Ikehata et al. [83]; at longer wavelengths the CPD yield becomes so low that systematic errors become proportionately larger; leading to an over reporting of CPD due to the longer wavelength UVA in the basal layer. Another reason for this discrepancy is that optical properties used for the upper layers are underestimating the extent of scattering and absorption in the longer wavelength UVA; meaning that in the simulations, more radiation reaches the basal layer than would happen *in vivo*.

Given the evidence presented in Figure 4.9, the spectral yield method is likely to provide a better estimation of CPD formation than that provided by the band yield method (as used in reference [32]).

4.4.4 Epidermal DNA as protection

The focus in the analysis presented here is on DNA damage within the basal layer, as this is damage with carcinogenic potential. DNA damage also occurs in the epidermis. As keratinocytes in the epidermis are likely to be committed to terminal differentiation, any damage occurring here is unlikely to have long term consequences [50, 85]. As a result, it may be that DNA within the epidermis actually plays a protective role in shielding the basal layer from UVR. Melanin is usually considered to be the only protective chromophore, however recent research indicates that the role of melanin can no longer be considered as purely protective, and it may in fact be carcinogenic [52] (for more detail, please see the discussion in Chapter 5). The results presented here point towards DNA within epidermal keratinocytes being a potentially protective mechanism for cellular DNA in the basal layer.

4.5 Conclusion

The MCRT model described in Chapter 3 was adapted to simulate irradiation of human skin types I & II by sunbed and solar sources. These datasets produced by the simulations were interrogated to attempt to quantify the amount of DNA damage occurring in the basal layer using two different methods. However the model does not include UVR induced enzymatic DNA repair mechanisms (which would reduce the total number of CPDs formed), nor other sources of CPD formation, such as dark CPDs formed both with and in the absence of melanin [52, 72]. As a result, the model is likely to under represent the total number of CPDs formed and by way of compensation, ratios of sunbed induced CPDs to solar induced CPDs were presented. The validity of these results relies on the assumption that other CPD formation methods; and repair processes, follow a similar wavelength dependence to direct CPDs.

Of the two methods of calculating the CPD yield presented, the spectral yield method is likely to provide the most accurate estimation of CPD formation.

Using the spectral yield results, Table 4.2 suggest the sunbed induces about 1.7 times more CPD than solar radiation. The conclusion is then drawn that 6 minutes on a sunbed gives the same damage as 10 minutes in the Mediterranean sun.

The results quantify the relative risk of direct CPD formation from sunbed use in terms of solar exposure. By implication this quantifies the risk of direct DNA damage due to exposure to UVR from a sunbed in comparison to that from Mediterranean sunlight.

The basal layer has a high concentration of DNA [81] and is considered the layer of the skin that can accumulate enough DNA damage to cause risk to human health [50]. The argument that UVB radiation can not penetrate far enough into the epidermis to cause significant damage to the basal layer is not supported by this model.

This model is only applicable to Fitzpatrick skin types I-II that are not UVR adapted, where the melanin resides immediately above the basal layer; however the model could be adapted to simulate other skin types, and these are discussed in the following chapter. When skin is not UVR adapted, the UVR causes greater risk to skin health due to the lower concentration of melanin in the epidermis, as part of the response to UVR involves melanogenesis, and movement of existing melanin into the living epidermis (colloquially known as ‘tanning’). This model could be extensively

adapted, by implementation of time dependent elements, to simulate this process.

Chapter 5

Simulating Melanin Distribution

Synopsis

The previous chapter describes a MCRT model capable of simulating UVR induced direct DNA damage in the basal layer of skin types I & II. This chapter describes the extension of the model in order to simulate UVR induced direct DNA damage in skin type VI. By way of validation, the model is designed to simulate published experimental methods as far as possible. Results comparing theoretical differences in CPD formation between skin types I & II, and skin type VI are compared to findings obtained from the same published experimental work. The model is also used to investigate the impact of melanin distribution on UVR induced DNA damage, and to quantify the extent to which results differ when solar radiation exposure is investigated.

5.1 Introduction

Melanin is considered to be the chromophore primarily responsible for photoprotection against DNA damage in the skin [51]. Melanin is a natural skin pigment, and is present in the skin in various quantities and qualities, presenting as different skin colours across and within individuals.

Keratinocyte cancers (SCC & BCC) are known to be caused by mutations induced by UVR [3]. In black skinned individuals, incidence of SCC and BCC is lower (approximately 20 to 60 times less common) than that found within those with white skin [86, 87, 88].

It has been reported that the extra protection provided by melanin in black skin is not enough to account for the lower incidence of keratinocyte cancers reported in black skin [89]. It has been suggested that the distribution of additional melanin (rather than the presence of additional melanin) may explain the lower keratinocyte cancer incidence observed in in black skinned individuals [90].

Work by Fajuyigbe et al. [90] compared the melanin distribution in skin with experimentally obtained direct CPD yield in different layers. Results from skin types I & II were compared to those obtained from skin type VI. This allowed determination of a 'DNA protection factor' afforded by the melanin present in skin type VI. As the experimental work reported depth resolved melanin concentrations, and associated CPD yield in the basal layer, the research [90] provided an excellent basis for both simulation design and opportunity to compare theoretical results to experiment.

Melanin

Skin pigmentation, in the form of melanin, is considered to be the main photoprotective agent in the skin. As part of the response to UVR, melanocytes in the basal layer produce melanin, a pigment, from the non essential amino acid tyrosine. The melanin is encapsulated in organelles called melanosomes. Melanocytes are shown in Figure 1.1, with melanosomes visible within the melanocytes, illustrated by small brown dots. The melanosomes are taken up by surrounding keratinocytes, which move up through the epidermis. The rate of melanosome production, and the rate of uptake (and resulting distribution of melanin) is considered to be responsible for different skin colours. As the keratinocytes move towards the surface, the melanosomes begin to break down, distributing melanin throughout the skin. The rate of this degradation is skin type dependent [51].

5.2 Methods

Alterations to the model previously described are outlined here. In order to simulate the experimental method as described by Fajuyigbe et al. [90], changes were made to the irradiation source, the geometrical grid representation of skin layers, and the optical properties of the layers.

5.2.1 Irradiation source

The irradiation source used in the experimental work is an 300W-16S xenon arc solar simulator (SSR) [90]. The spectrum is shown in Figure 5.1. When comparing the SSR source with solar radiation, the SSR appears to be a poor substitute for solar radiation. This is illustrated in the left panel of Figure 5.2. However when the input spectra $I_i(\lambda)$ are erythemally weighted, via $E(\lambda)I_i(\lambda)$, (where the erythemal effectiveness $E(\lambda)$ is given by Equation 1.1 [15] and where λ is given in nm) then the spectra exhibit an almost identical shape, as shown in the right panel of Figure 5.2.

In the experimental work [90], UVR doses were delivered via a 7 mm diameter light guide in direct contact with buttock skin. A punch biopsy of 4 mm diameter was taken from the centre of the exposed area immediately after exposure. It is assumed the output from a light guide may be approximated as diffuse. Given this, and given that the irradiation area is larger than the area biopsied, the experimental method can be approximated as uniformly exposing the surface of a small area of the skin to diffuse UVR.

5.2.2 Grid setup

In order to simulate the distribution of melanin within the skin, the depth (z) resolution of the grid was increased to 1 μm. The lateral resolution remains at 10 μm Increasing the depth resolution increased demands on available computer memory, and in order to compensate for this, a smaller patch of skin (of surface area 0.5 mm $\times$ 0.5 mm) was simulated. The grid design used is detailed in Table 5.1. Details on why the grid design was chosen can be found in the Grid geometry section of Chapter 3.

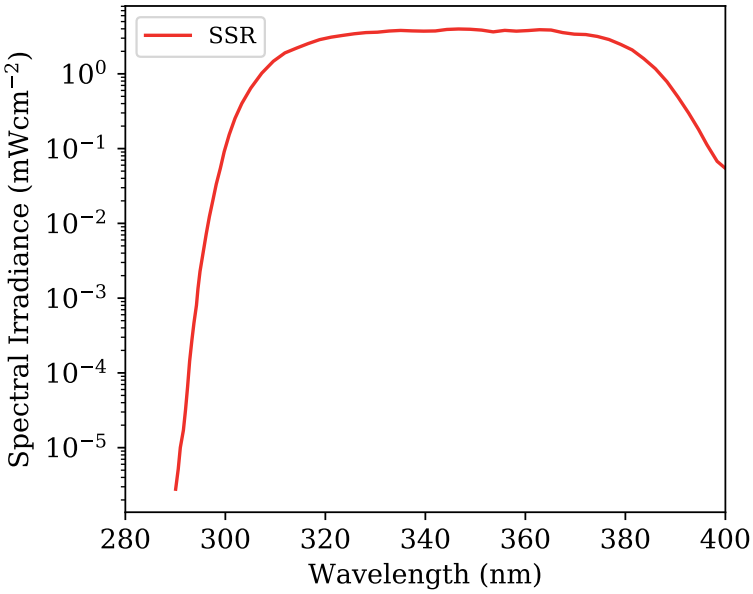

Figure 5.1: *Spectrum of the solar-simulated radiation (SSR) source used in experiments by Fajuyigbe et al. [90]. The radiation is delivered to the skin via a liquid light guide. The SSR source is a 300W-16S xenon arc solar UVR simulator is made by Solar Light, USA.*

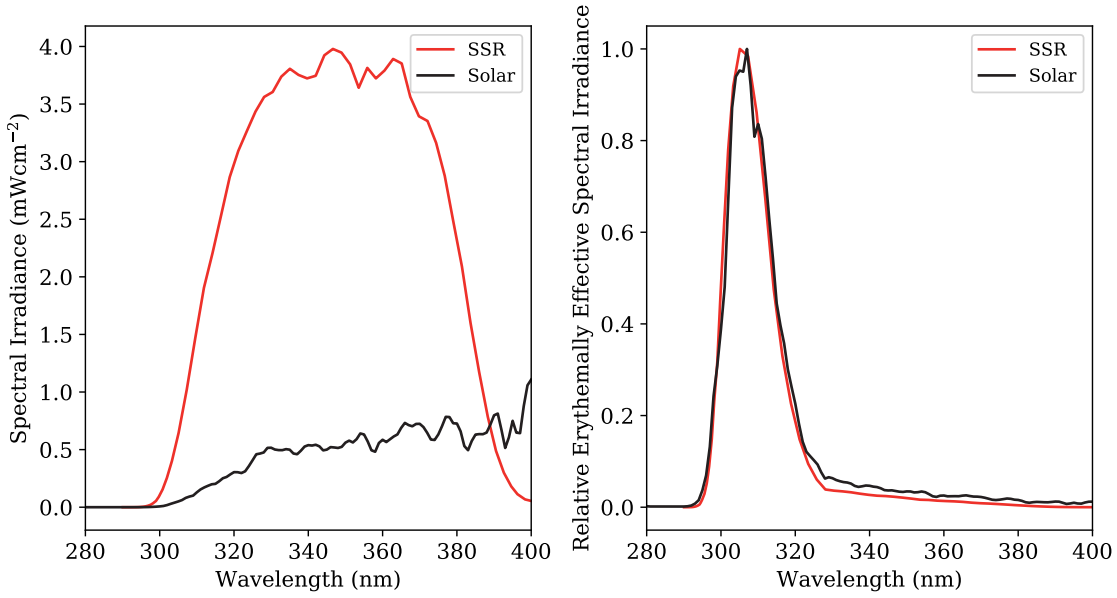

Figure 5.2: *The left panel directly compares the SSR source with solar radiation. It is evident the two spectra are different shapes (even when neglecting the difference in intensities), and as such the SSR does not appear to be a suitable alternative to solar radiation. However the right panel shows the relative erythemal effectiveness of each source (described by Equation 1.1). Both sources have a very similar wavelength dependent erythemal effectiveness, so the SSR is considered a suitable solar simulator.*

Dimension	Size	Number of Voxels	Resolution
x	0.05 mm	50	10 μm
y	0.05 mm	50	10 μm
z	0.04 mm	400	1 μm

Table 5.1: *Specifications of spatial grid used to simulate the upper layers of skin tissue. As before, each voxel each voxel (in total, $50 \times 50 \times 400 = 10^6$ voxels) contains a path length counter, enabling each voxel to act as a detector, recording a full spectra of the wavelengths reaching that voxel.*

5.2.3 Skin types

In the work by Fajuyigbe et al. [90] experimental results for melanin distributions (and CPD) are obtained from punch biopsies from the buttock. This ensures the biopsied skin is unlikely to be regularly exposed to UVR. Therefore the epidermal depths simulated represent the buttock specific epidermal depths reported by Sandby-Møller et al. [44]. Fajuyigbe et al. [90] also report melanin distribution within the upper, middle and the bottom of the epidermis, and so the epidermal layer within the model was further divided into two parts; an upper and a mid-epidermal layer. The epidermal depths and layer dependent melanin concentrations are reproduced in Table 5.2.

Layer Depths

Layer	Depth	Percentage of total Melanin	
		Skin Type I/II	Skin Type VI
Stratum Corneum*	14.9 μm	0%	0%
Epidermis (Top)	55.0 μm	5%	13%
Epidermis (Middle)	76.5 μm	15%	27%
Melanin Layer	86.5 μm	80%	60%
Basal Layer*	96.5 μm	0%	0%
Dermis**	2000-6000μm	0%	0%

Table 5.2: *Depths of epidermal layers in buttock skin. Depths marked * taken directly from Sandby-Møller et al. [44]. The base of the dermis, marked **, extends deeper than the domain of the grid. Here, the living epidermis is further divided into two sections (the middle, and the upper), in order to simulate melanin distributions described by Fajuyigbe et al. [90].*

Similar to before, layer separations are described by the following equations, with the sinusoidal z_{base} representing the shape of the dermal papillae,

$$
\begin{aligned}
z_{\text{base}}(x,y) &= 30\ \mu\text{m} \times \sin\left(\frac{x}{15\ \mu\text{m}}\right) \times \cos\left(\frac{x}{15\ \mu\text{m}}\right) \\
z_{\text{sc}} &= 14.9\ \mu\text{m} \\
z_{\text{epidermis (top)}}(x,y) &= \frac{2}{3} z_{\text{base}}(x,y) + 55.0\ \mu\text{m} \\
z_{\text{epidermis (mid)}}(x,y) &= z_{\text{base}}(x,y) + 76.5\ \mu\text{m} \\
z_{\text{melanin}}(x,y) &= z_{\text{base}}(x,y) + 86.5\ \mu\text{m} \\
z_{\text{basal}}(x,y) &= z_{\text{base}}(x,y) + 96.5\ \mu\text{m}
\end{aligned}
$$

Optical properties

The optical properties for the stratum corneum, basal layer and dermis remain as previously described. Within the epidermal and melanin layers, the scattering coefficients remain as previously described, however the absorption properties are altered. In the previous chapter it is assumed that in non exposed skin types I & II, melanin is concentrated above the basal layer. In fact, as reported by Fajuyigbe et al. [90], they find that across different skin types, melanin is distributed throughout the epidermis in a similar way, with just the total amount changing. From the published results [90] it is possible to obtain the actual percentages for basal, middle epidermis and upper epidermis for skin type VI, as reproduced in Table 5.2. However for skin types I & II, these values are not easily elucidated from the published results [90]. A distribution is assumed with the majority of the melanin residing above the basal layer. This is detailed in Table 5.2.

Within this simulation, one model is built to represent skin types I & II, and another for skin type VI. As the total epidermal melanin concentration is assumed to be 2 % for skin type I and 4 % for skin type II, the combined model for skin types I & II uses a total melanin concentration of $V_{\text{mel,I/II}} = 3\,\%$. For skin type VI, the total melanin concentration is assumed to be $V_{\text{mel,I/II}} = 24\,\%$, 8 times that found in skin types I & II [91]).

This is divided up into the layers as described in Table 5.2, resulting in absorption coefficients of,

$$\mu_{\text{a,epi}_{\text{upper}}} = 6.6 \times 10^{11} \lambda^{-3.33} f_{\text{upper}} V_{\text{mel}} \tag{5.1}$$

$$\mu_{\text{a,epi}_{\text{middle}}} = 6.6 \times 10^{11} \lambda^{-3.33} f_{\text{middle}} V_{\text{mel}} \tag{5.2}$$

$$\mu_{\text{a,mel}} = 6.6 \times 10^{11} \lambda^{-3.33} f_{\text{melanin}} V_{\text{mel}} \tag{5.3}$$

Where $f_{\text{upper}}, f_{\text{middle}}$ and f_{melanin} are the proportions of total melanin as distributed across the layers as described in Table 5.2.

The values described in Equations 5.1 to 5.3 are added to the non melanised epidermal absorption coefficients using the method described in Chapter 3, and thus a layer dependent absorption coefficient is obtained.

The simulations as described were run with 10^8 power packets; which produced convergent results. The results were analysed using methods similar to those described in the previous chapter,

and the fluence reaching the basal layer was extracted from the path length estimator results, using Equation 4.3.

5.2.4 DNA protection factor

Within the published experimental results [90], the layer dependent CPD yield in skin type VI was compared to that from skin types I & II. This was described by the authors as the DNA protection factor,

$$\mathrm{DNA_{PF}} = \frac{\mathrm{CPD_{I/II}}}{\mathrm{CPD_{VI}}} \tag{5.4}$$

where $\mathrm{CPD_{I/II}}$ is the CPD yield in skin types I & II, and $\mathrm{CPD_{VI}}$ the CPD yield in skin type VI. The DNA protection factor describes the amount by which melanin in black skin protects DNA from damage. Within the reported experimental procedure, the CPD yields were obtained by exposing different volunteers to different doses of UVR, and working out the relative CPD yields from these. It is possible to analyse results from the simulation in order to produce comparable results to those published [90]. Similar spectra to those displayed in Figure 5.3 may be extracted for the upper and middle layers of the epidermis, using the following equations,

$$\psi_{\mathrm{upper}}(\lambda) = \frac{1}{N_{\mathrm{upper}}} \sum_{i,j,k} \psi_{i,j,k}(\lambda) \text{ for } i,j,k \in \text{upper epidermis} \tag{5.5}$$

$$\psi_{\mathrm{middle}}(\lambda) = \frac{1}{N_{\mathrm{middle}}} \sum_{i,j,k} \psi_{i,j,k}(\lambda) \text{ for } i,j,k \in \text{middle epidermis} \tag{5.6}$$

where layer N_{upper} and N_{middle} are the number of voxels within the upper and middle epidermal layers respectively, and the fluence $\psi_{i,j,k}$ is that found at voxel of index $\{i,j,k\}$ within the upper or middle epidermal layer respectively.

The method to analyse spectral CPD yields, as described in the previous chapter, is adapted here to compare CPD yields between different skin types, across different layers,

$$\mathrm{DNA_{PF,\,layer}} = \left(\frac{\mathrm{CPD_{I/II}}}{\mathrm{CPD_{VI}}}\right)_{\mathrm{layer}} = \sum_{\lambda=280\,nm}^{400\,nm} \frac{A_{\mathrm{CPD}}(\lambda)\psi_{\mathrm{layer,I/II}}(\lambda)}{A_{\mathrm{CPD}}(\lambda)\psi_{\mathrm{layer,VI}}(\lambda)} \tag{5.7}$$

Where A_{CPD} is the CPD action spectrum (from Ikehata et al. [83]), and *layer* is the layer of interest (upper epidermis, mid epidermis, or basal layer).

5.2.5 Melanin distribution

Fajuyigbe et al. [90] postulate that it is melanin distribution in black skin, rather than melanin content alone, that provides the extra protection against UVR induced DNA damage. Using MCRT, this could be examined. To investigate this, the model as described in this chapter was altered to simulate the melanin distribution as was assumed in the initial model design and published in reference [32]. These assumed that all melanin present in the epidermis is concentrated in a 10 μm layer above the basal layer.

The simulations were run with 10^8 power packets, and the fluence reaching the basal layer was extracted from the path length estimator results, using Equation 4.3.

5.2.6 Solar effects

It is difficult to use solar radiation in a controlled environment, as the spectrum of solar radiation changes with time of day or year. For this reason, solar simulators are used to simulate solar radiation under laboratory conditions. Given that MCRT is able to simulate any irradiation source, the simulations described in this chapter were repeated for solar radiation (as described in the previous chapter).

5.3 Results

The fluence incident on the surface of the skin, and on the basal layer of both skin types I/II & VI, is shown Figure 5.3.

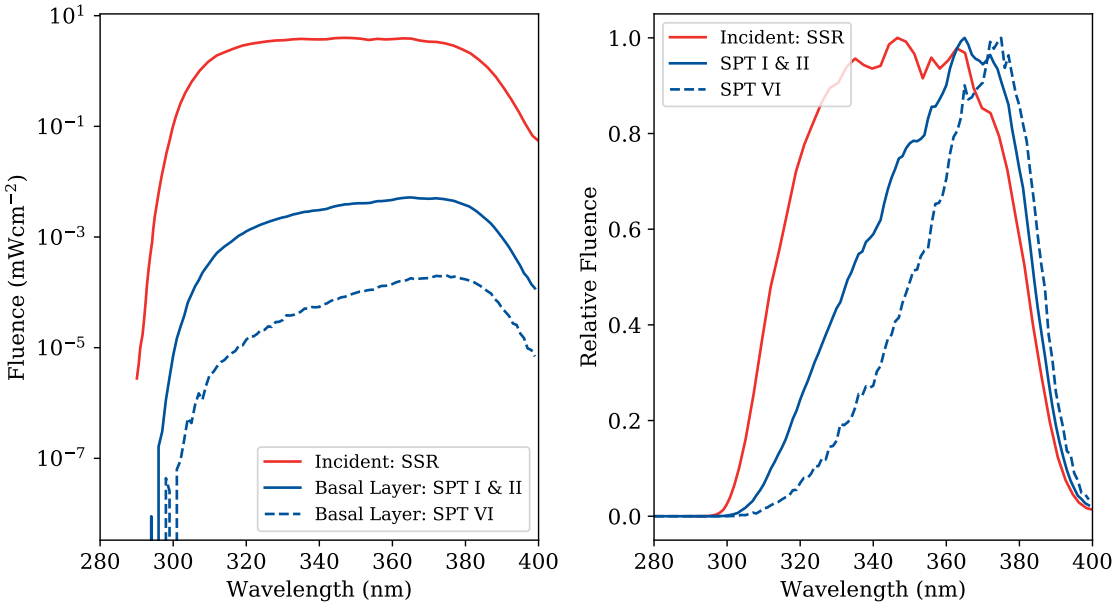

Figure 5.3: *Radiation incident on the basal layer of both skin types simulated, along with the incident radiation. The left panel shows the absolute irradiance of the source, along with the fluence incident on the basal layer in both skin types. The right panel shows the same data, to illustrate how additional melanin shields relatively more shorter wavelength radiation. The data presented here are extracted from the main dataset using Equation 4.3.*

By extracting the spectrally resolved fluence from the basal layer, Equation 5.7 was used to calculate the theoretical DNA_{PF} for different layers. These are presented in Table 5.3, where they are compared directly to published experimental results [90].

5.3.1 Melanin distribution

To investigate the postulation in reference [90], (that it is melanin distribution rather than melanin content alone, that provides additional protection) results from a simulation where all melanin is concentrated above the basal layer) is shown in Figure 5.4.

	Upper Epidermis DNA_{PF}	Mid Epidermis DNA_{PF}	Basal Layer DNA_{PF}
Published Results [90]	5.0 (95% CI 4.5-5.5)	16.5(95% CI 11-27)	59.0 (95% CI 24-110)
Simulation	5.8	24.4	109.5

Table 5.3: *Comparison of the level of DNA protection factor at different depths afforded by skin type VI as compared to skin types I& II.*

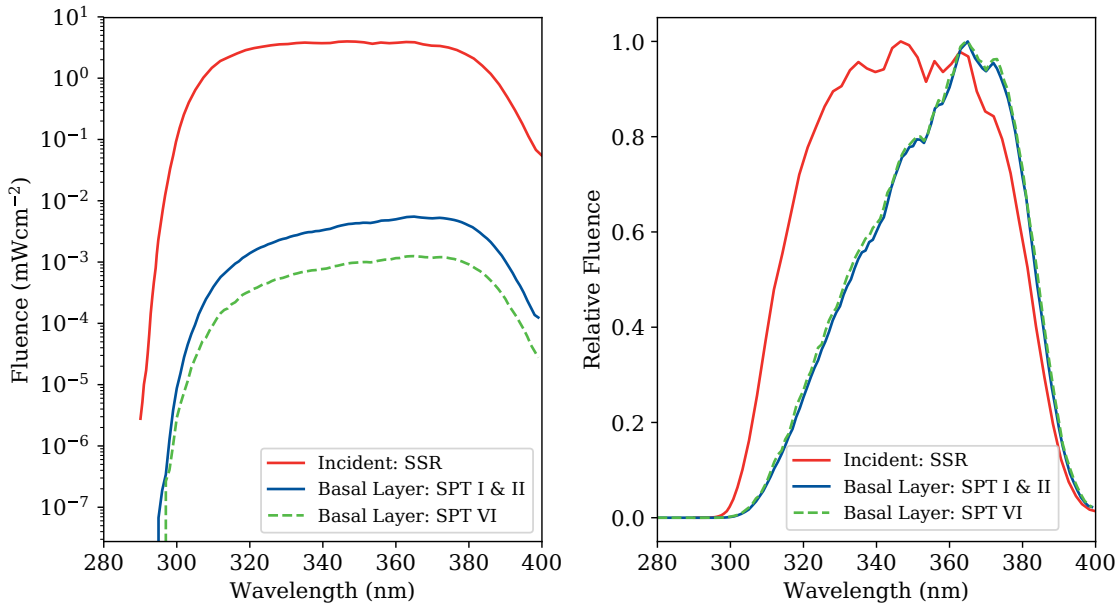

Figure 5.4: *Radiation incident on the basal layer of both skin types simulated, along with the incident radiation, for simulations of buttock skin where all melanin is concentrated in a 10 µm layer above the basal layer. The right panel indicates that in this scenario, the shape of the spectra incident on the basal layer in both skin types is almost exactly the same, and the additional quantity of melanin in skin type VI has not shielded the basal layer from proportionally more shorter wavelength UVB.*

5.3.2 Solar effects

The basal layer fluence results were extracted from simulations of solar irradiation. These are shown, along with incident spectra (from the left panel of Figure 4.2, in Figure 5.5.

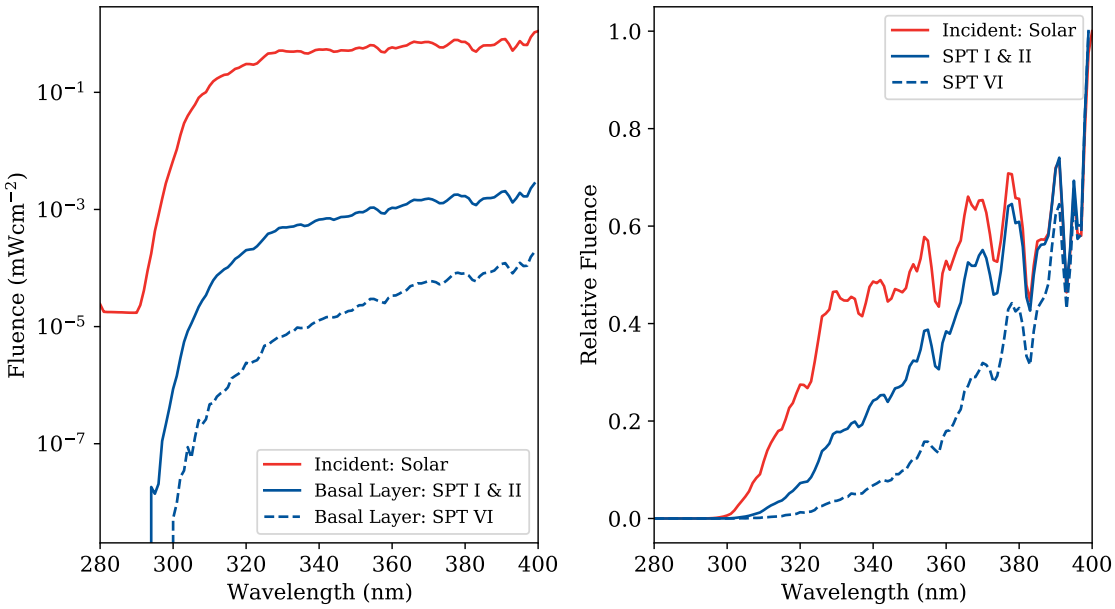

Figure 5.5: *Solar radiation incident on the basal layer of both skin types simulated, along with the incident radiation. The right panel shows normalised incident irradiance, along with the fluence on the basal layer for both skin types, to illustrate how additional melanin shields against relatively more shorter wavelength radiation. The data presented here are extracted from the main dataset using Equation 4.3 in Chapter 4.*

Equation 5.7 was used to calculate the theoretical DNA_{PF} for different layers. These are presented in Table 5.4.

	Upper Epidermis DNA_{PF}	Mid Epidermis DNA_{PF}	Basal Layer DNA_{PF}
Solar (Theoretical)	5.6	22.8	85.6

Table 5.4: *Comparison of the DNA protection factor at different depths afforded by skin type VI as compared to skin types I & II.*

5.4 Discussion

Melanin depth distribution and the subsequent effects on UVR penetrating the skin have previously been examined by computational modelling [42]. This work used commercial software to perform ray tracing (a subset of MCRT and does not capture scattering media well), and investigated the 370 nm to 900 nm wavelength range, which was loo large for direct comparison with the work presented here.

As expected, Figure 5.3 shows the basal layer in skin type VI receives betwen 10 to 100 times less radiation than for skin types I & II, with evidence of considerable epidermal shielding of the shorter wavelength UVB radiation.

In comparing the simulation results to the experimental results (displayed in Table 5.3), the resulting DNA_{PF} for the middle epidermis and the basal layer lie within the 95% confidence intervals as given by the experimental results; though at the upper limit of these confidence intervals. The result for the upper epidermis lies just outside. Given that the DNA protection factor for the upper epidermis is mostly influenced by the optical properties for the stratum corneum (though there is some influence from the optical properties of the epidermis below, due to back scatter), this may indicate that the optical properties (or the geometry) for the stratum corneum require alteration. The results suggest that the optical properties (and geometry) for the stratum corneum are either underestimating the optical depth of the skin type I & II stratum corneum, or overestimating the optical depth of the skin type VI stratum corneum. The optical properties and geometry for the stratum corneum were taken from literature (Chapter 3 and Table 5.2) however in future varying these parameters may be helpful in adapting the model to simulate real world results.

Overall, though the model gives results that are within the confidence intervals, the high value of the DNA_{pf} found in the simulations as compared to the average found experimentally indicates that the simulation has either over-estimated the amount of CPD inducing radiation penetrating into skin types I & II, or underestimated the same for skin type VI.

Effect of melanin distribution on DNA protection factor

When all the melanin is concentrated in a single 10 μm layer above the basal layer, the total DNA protection factor DNA_{pf} (calculated using Equation 5.7) is found to be only $DNA_{pf} = 3.86$. The theoretical findings presented here support the conclusion presented in reference [90] that it is the distribution of melanin within black skin, and not just the presence of addition melanin, that significantly affects the level of DNA protection afforded by black skin. This has potential implications for potential interventions for skin cancer prevention. It is currently assumed that sunscreens work by creating a film on the surface of the skin (and that a sunscreen that penetrated into the skin would be undesirable). These results indicate that perhaps if a sunscreen could safely penetrate into the upper layer of the skin and remain there, this may be an efficacious sunscreen solution.

5.4.1 Solar radiation

The results in Table 5.4 indicate that the theoretical DNA_{pf} provided by black skin exposed to solar radiation is slightly lower than the theoretical DNA_{pf} provided by black skin exposed to solar simulated radiation. This has may suggest that SSR under-induces CPD in black skin when compared to solar irradiation, or similarly, that SSR over-induces CPD in skin types I & II when compared to solar irradiation. To answer this conclusively, the model would benefit by being able to estimate the absolute number of CPD formed in different skin types, and under different irradiation conditions.

5.5 Conclusion

The theoretical results, validating against published experimental protocol presented here are broadly within the 95 % confidence intervals as stated from experimental results. However the results indicate that either the model is under estimating the amount of carcinogenic UVR reaching the basal layer for skin type VI, or overestimating the same for skin types I & II. It is important to note that extensive work by Karsten et al. [42] has computationally investigated the scattering properties of melanin as it fragments in the epidermis (in the 370 nm to 900 nm wavelength range). The simulations presented here treat melanin as a purely absorbing chromophore, however this is a crude approximation. Further work, including applying the fragmentation pattern and scattering properties identified by Karsten et al. [42] may improve this model, and better reproduce experimental results.

The results indicate that by localising melanin above the basal layer, the DNA_{pf} is reduced by 30 fold. This result has implications for UVR protection strategies. In future, this code could be developed further to simulate a true melanin gradient within the living epidermis.

However, the model may be compromised, as it does not take into account the effect of 'dark CPD', which are CPD which form after exposure to UVR has ceased in both melanin rich melanocytes [52] and in keratinocytes containing no melanin [72], and may contribute up to half of the total CPD yield observed in melanocytes [52]. In addition, DNA repair processes are not modelled. These effects could be included in future development of this model.

Chapter 6

Theoretical prediction of DNA photoprotection by sunscreen

Synopsis

Sunscreens are topical products used primarily to prevent sunburn. Sunscreens are formulated such that after application, the constituent UVR filters form a protective film on the surface of the skin. The performance of sunscreens are assessed against several standards, the most commonly recognised being the sun protection factor (SPF). Recent research has investigated the extent to which sunscreens protect DNA from photodamage. As current SPF testing necessitates the induction of erythema in human subjects, and any assessment of the DNA protection factor from a given sunscreen requires invasive procedures, accurate simulations of such processes may prevent harm to human subjects. The aim of this work is to build and add a film of sunscreen to the surface of the skin model described in previous chapters, and investigate effects on the theoretical CPD yield in skin protected by a layer of sunscreen.

6.1 Introduction

A sunscreen film consists of UVR filters and some formulation, to act as a vehicle to improve cosmetic features (such as ease of spreading, scent or appearance). UVR filters work by absorbing and scattering UVR, and when these are present in a film on the skin, this means the amount of UVR reaching the skin is reduced. There are many UVR filters approved for use by different regulatory systems [92]). The nomenclature of UVR filters can be complex, with filters referred to by several different chemical or trade names [92]. Within this text UVR filters are referred to by the relevant international nonproprietary name and the associated standard abbreviation.

6.1.1 Testing of sunscreens

Several different methods are used to characterise the efficacy of sunscreen. Of these, the most recognisable is the SPF. The SPF quantifies how much radiation with the ability to cause sunburn

is transmitted by the sunscreen (e.g. an SPF 30 sunscreen transmits $1/30^{\text{th}}$ of incident erythemal radiation- radiation with the potential to cause sunburn under test conditions). Other rating systems (such as persistent pigment darkening, or the Boots star rating [93, 94]) describe how well the sunscreen filters UVA radiation. The UVA rating systems differ considerably across regulatory bodies and are outside the scope of this thesis.

In vivo SPF testing

To label a product with an SPF, a test on human subjects must be performed. This test adheres to an international standard [95] and is effectively the same across all regulatory bodies in the world (with small changes in protocol).

A group of volunteers is selected with skin described as light by the Individual Typology Angle (ITA) system [96]. The ITA describes pigmentation of skin (whereas the Fitzpatrick Skin Type describes typical response to UVR, with pigmentation inferred from this). Volunteers must have an average ITA of between 41° to 55° (in practice, this range is comparable to Fitzpatrick types I and II). Each volunteer has an area of the skin on their back covered by a reference sunscreen, the sunscreen under test, and an area left unprotected. An example of the absorption spectrum of the reference sunscreen is shown in Figure 6.1.

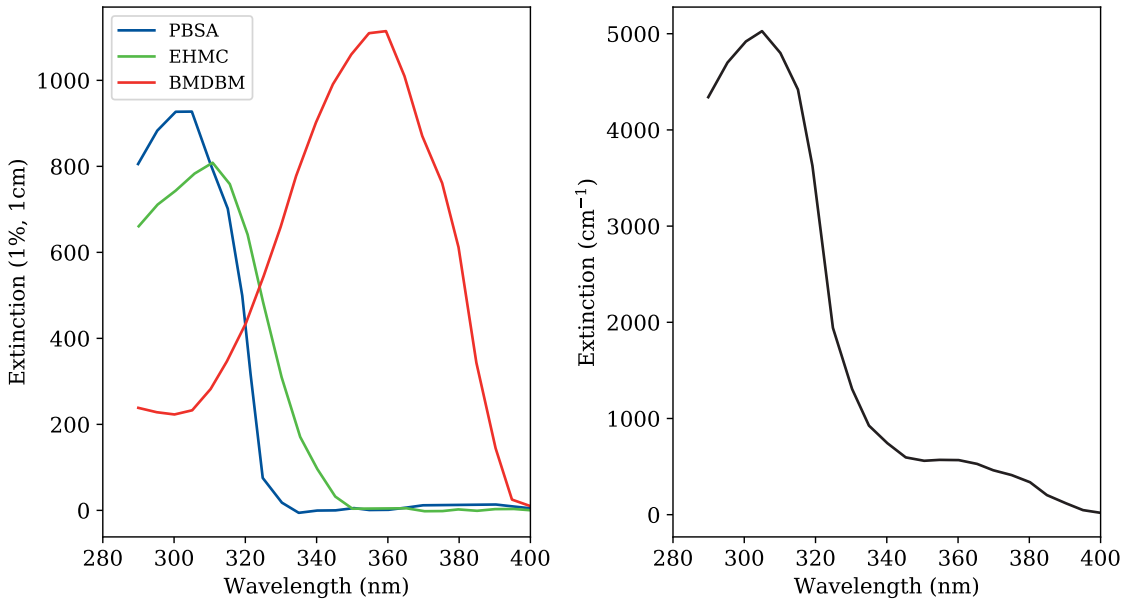

Figure 6.1: *The left panel shows the absorbance of the three constituent filters of the standard P3 sunscreen at a concentration of 1% in a solution (data extracted from Osterwalder & Herzog [92]). The right panel shows the absorbance of the P3 standard sunscreen, which comprises by volume 2.78% PBSA (phenylbenzimidazole sulfonic acid), 3.0% EHMC (octyl methoxycinnamate) and 0.5% BMDBM (avobenzone). The P3 sunscreen is expected to give an SPF of 15.5 ± 1.5 [95, 97].*

The application of the sunscreens must strictly adhere to protocol. The amount applied must be $2\,\text{mg}\,\text{cm}^{-2}$ and this must be applied to the skin in a specified motion with a gloved finger. Small sites on each volunteers back are exposed to increasing (timed) doses of radiation from a solar

simulator lamp. Between 16-24 hours post exposure, erythema is assessed by a trained individual, who identifies the minimal dose at which each volunteer has developed erythema (the Minimal Erythemal Dose- MED). For an individual, the SPF is given by,

$$\mathrm{SPF}_{\mathrm{individual}} = \frac{\mathrm{MED}_{\mathrm{protected}}}{\mathrm{MED}_{\mathrm{unprotected}}} \tag{6.1}$$

The SPF of the product under test is the mean of all valid individual SPFs calculated. During the test, the volunteer's response to a control sunscreen with a fixed SPF is also assessed, and a reading of $\mathrm{SPF}_{\mathrm{individual}}$ is only considered valid if the individual has displayed the erythemal response expected for this sunscreen with a fixed SPF (known as a reference sunscreen).

Reference sunscreens

The SPF testing of a new sunscreen is performed against a 'reference sunscreen', by way of calibration. A reference sunscreen is a formulation with exact ingredients, quantities and manufacturing process specified by the international standard [95]. On following the testing protocol described above, the reference sunscreen will return an SPF within a specified range. One reference sunscreen is the P3 sunscreen. Prior to the introduction of the 2019 standard, sunscreens expected to return a high SPF were tested against the P3 sunscreen (in the latest international standard [95], other high SPF standard sunscreen formulations are specified). When testing the P3 sunscreen, an individual must respond with an $\mathrm{SPF}_{\mathrm{individual}}$ of 15.5 ± 1.5.

Although this SPF testing protocol is a carefully developed international standard, there has been some debate as to the extent to which the SPF is representative of 'real life' protection afforded by sunscreens. It has been suggested that the SPF may overestimate protection in natural sunlight [98], and specifically that the SPF rating on a UVB biased sunscreen overestimates the protection afforded in temperate latitudes [99]. This is because the protection the sunscreen provides will change as the irradiation profile changes. One study has shown that although differently filtered solar simulators may meet the international standard, there can be differences of up to 50% between the rated SPF using these simulators [100]. The biggest issue with *in vivo* SPF testing remains that it necessitates harm to an individual, as to determine an SPF, erythema must be induced. In addition, the process is expensive and time consuming. As such, there is great interest in *in vitro* and *in silico* methods.

SPF testing *in vitro*

Although *in vitro* testing is not yet considered an acceptable method for evaluating the SPF of a sunscreen, some *in vitro* methods are used to rate UVA protection. *In vitro* methods use transmission spectroscopy, where sunscreen is applied onto a roughened PMMA (polymethylmetacrylate) plate in order to better simulate the surface of human skin. The UVR transmittance analyser contains a UVR lamp and an integrating sphere, and measures the transmittance of the sunscreen on the PMMA plate.

$$\mathrm{SPF}_{\text{in vitro}} = \frac{\sum_{\lambda=290\ \mathrm{nm}}^{400\ \mathrm{nm}} E(\lambda) I_{\text{source}}(\lambda)}{\sum_{\lambda=290\ \mathrm{nm}}^{400\ \mathrm{nm}} E(\lambda) I_{\text{source}}(\lambda) T(\lambda)} \tag{6.2}$$

Equation 6.2 describes how the *in vitro* SPF can be calculated, where $I_{\text{source}}(\lambda)$ is the incident spectrum, $T(\lambda)$ is the transmittance of the sunscreen measured by the analyser, and $E(\lambda)$ is the 1998 CIE erythema action spectrum [15, 101] described by Equation 1.1, reproduced here for convenience,

$$E(\lambda) = \begin{cases} 1 & 250\ \mathrm{nm} < \lambda \leq 298\ \mathrm{nm} \\ 10^{0.094(298-\lambda)} & 298\ \mathrm{nm} < \lambda \leq 328\ \mathrm{nm} \\ 10^{0.015(140-\lambda)} & 328\ \mathrm{nm} < \lambda \leq 400\ \mathrm{nm} \end{cases} \tag{6.3}$$

The 1998 CIE action spectrum is displayed in Figure 6.2.

If sunscreen is applied to the plate in the same amount as specified by the *in vivo* test, the SPF is overestimated. It is thought that this is because the PMMA plates do not simulate the surface of the skin well, and other application amounts are recommended depending on the roughness of the PMMA plate in use [102].

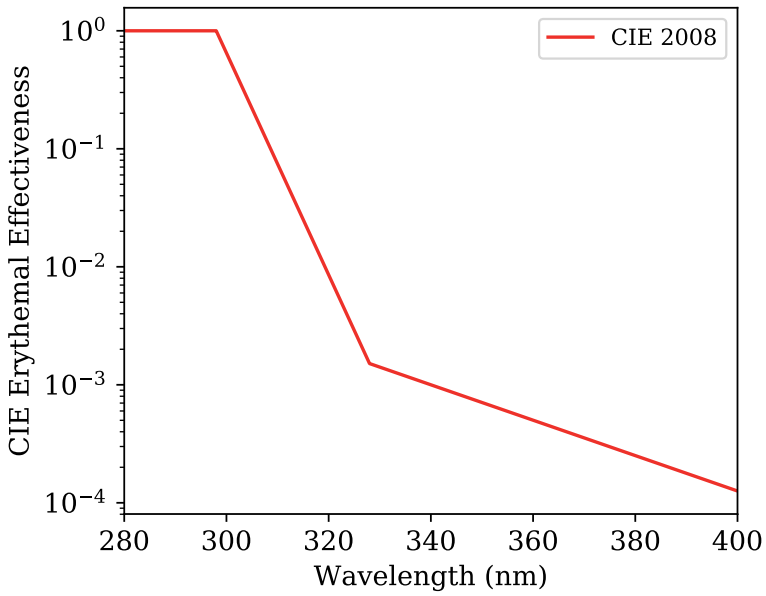

Figure 6.2: *This shows the CIE 1998 (ISO/CIE 1999) Erythemal effective action spectrum [15, 101].*

SPF prediction *in silico*

As it is assumed the UVR filters within a sunscreen are solely responsible for the UVR filtration (there is no protective effect afforded by the vehicle), and the *in vivo* application amount is carefully

measured, it could be assumed that simple application of the Beer-Lambert law (Equation 6.4) might provide a good estimation of the SPF. Although sunscreen contains high concentrations of UVR filters, the Beer-Lambert law is considered valid [103]). The Beer-Lambert law is reproduced here,

$$\frac{I_t}{I_i} = 10^{-\varepsilon l c_{\text{conc}}} \tag{6.4}$$

where I_i is the intensity of incident radiation, and I_t the intensity of transmitted radiation (both of which are required to determine the SPF of a given filter). The molar decadic extinction ε and the concentration c_{conc} are easily determined for a given sunscreen. However l, the thickness of the sunscreen film, is more difficult to elucidate. Human skin varies in thickness [104] and even with careful application it is impossible to get a even amount covering the skin. The first attempt to provide a mathematical solution to this was by O'Neill, by way of development of a step film model [105]. This divided the applied volume of sunscreen into a depleted area and an area of excess, then used the resulting differing values of l (film thickness) to calculate the SPF. Brown and Diffey used this to explain why sunscreen protection afforded *in vivo* was less than would be predicted using the Beer-Lambert law [106]. Eventually the step film model was abandoned in favour of using a probability distribution to simulate the film profile [102]. Current best practice for the modelling of sunscreen film thickness uses the inverse of the gamma distribution, an asymmetrical distribution described by Equation 6.5. In this context, this distribution describes the variation in height of a sunscreen film (h) relative to the 'parent film' height (that is, the film height achieved by the volume of sunscreen applied if there is no variation in film height, see Figure 6.3).

$$f(h) = \left(\frac{h}{b}\right)^{c-1} e^{-\frac{h}{b}} \frac{1}{b\Gamma(c)} \tag{6.5}$$

In Equation 6.5, h indicates the proportion of the 'parent' film present, and $f(h)$ the probability of finding this h value for a given sunscreen. To construct the film thickness profile from the probability distribution, the height h is selected from the cumulative distribution (Equation 6.6). With this method for determining film thickness, the sole factor determining the probability distribution is c, the shape parameter (which, in this case, represents the asymmetry of the film height distribution, or the evenness of spreading. A smaller shape factor c indicates an asymmetrical distribution, with less even sunscreen application). The scale factor b is needed for normalisation, and to conserve the volume of sunscreen applied (such that $bc = 1$).

$$F(h) = \int_0^h f(x)dx \tag{6.6}$$

The publicly available online sunscreen formulation simulators [97] (the BASF Sunscreen simulator [107] and the DSM sunscreen optimiser [108]) use a combination of Beer's law in conjunction with the treatment of film thicknesses described here. The predicted shape profile c is determined using an equation taking into account filter concentrations (reproduced in part in Equation 6.10). In addition to these considerations, photoinstabilites are taken into account, as well as syngergistic or deleterious effects of certain combinations of UVR filters (these are fully detailed in Herzog & Osterwalder [97]).

Though existing *in silico* methods reproduce *in vivo* SPF results well, they are not considered

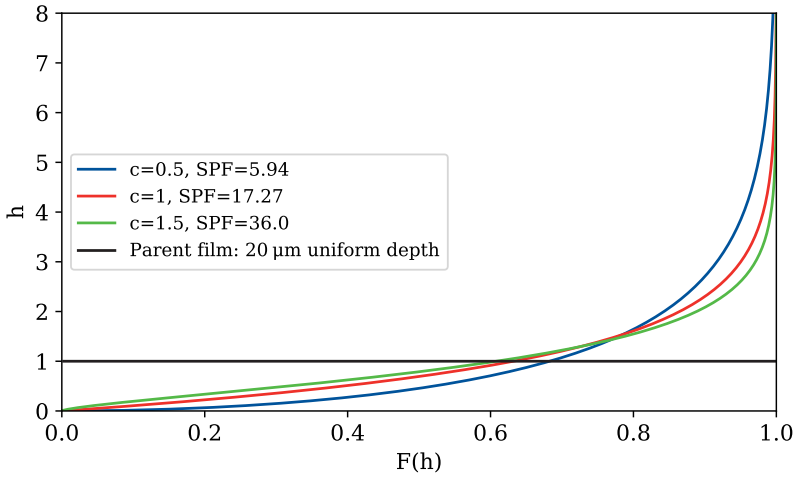

Figure 6.3: *This plot shows the different film profiles for different shape factors, and the associated SPF obtained when films of P3 sunscreen are simulated with different film profiles using a basic no grid MCRT method [97]. The black line indicates the parent film: a concept used in sunscreen simulation to suggest the potential film thickness achievable in an ideal scenario.*

acceptable replacements for *in vivo* testing. In addition, existing *in silico* methods do not give an indicate the efficacy of sunscreens in protecting DNA from damage, which can be provided by an MCRT model of the transport of UVR though a sunscreen film on human skin.

6.2 Monte Carlo transmission code

6.2.1 Methods

As a first step to building an MCRT model of sunscreen on skin, a basic Fortran 90 Monte Carlo sampling code was developed to ensure results from published work on sunscreen simulators could be reproduced. The Python SciPy Stats package was used to create the datasets for a given value of c (see Figure 6.3). This dataset was read into the Fortran 90 code as the film profile. The extinction coefficients for the filters comprising the P3 sunscreen were extracted from Osterwalder and Herzog [92] and checked against a known dataset (personal communication)[109]. The P3 sunscreen comprises 2.78% PBSA (phenylbenzimidazole sulfonic acid), 3.0% EHMC (octyl methoxycinnamate) and 0.5% BMDBM (avobenzone). The input spectrum is the international standard solar simulator as used by Osterwalder and Herzog [92]. The simple MC code randomly samples from the input spectrum to obtain a wavelength (λ), and from the film profile to obtain an (h) value, from which the film thickness $l(\mu\text{m})$ is determined using Equation 6.7 [102],

$$l = 10hQ \tag{6.7}$$

where Q is application amount in $\text{mg}\,\text{cm}^{-2}$. The factor $10 = 10\ \mu\text{m}\,\text{g}^{-1}$ comes from the assumption that sunscreen has a density of $\rho = 1\,\text{g}\,\text{cm}^{-2}$. Please note Equation 6.7 does not take into account any evaporation of the film (which would then inversely increase the concentration of the

UVR filters).

A maximum optical depth is obtained using,

$$\tau_{\max} = 2.303\varepsilon l \tag{6.8}$$

and if a randomly sampled depth is larger than this, the packet is transmitted (the factor 2.303 comes from conversion between logarithm bases, as $log_e(x)/log_{10}(x) = 2.303$).

The incident packets and transmitted packets are binned by wavelength, and the resultant SPF is found using Equation 6.9 where $E(\lambda)$ is the CIE erythemal effectiveness as described by Equation 6.3, N_i is the number of incident packets, and N_t the number of transmitted packets.

$$\mathrm{SPF}_{\text{in silico}} = \frac{\sum_{\lambda=290\ nm}^{400\ nm} E(\lambda)N_i(\lambda)}{\sum_{\lambda=290\ nm}^{400\ nm} E(\lambda)N_t(\lambda)} \tag{6.9}$$

6.2.2 Results

The results obtained by this simple code, and comparisons to published results [97] are shown in Table 6.1.

Shape Factor	Herzog and Osterwalder [97]	Basic MC results
c=0.5	6.3	5.94
c=1.0	17.3	17.27
c=1.5	35.0	36.0

Table 6.1: *Results of a very basic MC sampling code to reproduce published results from existing sunscreen simulators [97, 107, 108].*

The spectrum of solar simulated UVR transmitted through a film of P3 sunscreen is shown in Figure 6.4.

6.2.3 Discussion

There is good agreement between results obtained using the MCRT transmission code are compared to published results [97] in Table 6.1. Slight differences are likely due to different datasets used for the filter extinctions (the results from reference [97] will use extinction coefficients available to the authors from the commercial laboratories they are associated with, these are not publicly available). The good agreement between results give confidence that both the optical properties selected and the geometry (for film profiles) match those used by previous work [97].

Figure 6.4 illustrates how the sunscreen shown in Figure 6.1, and the shape factor from the high SPF scenario (Table 6.1), affects the transmission of radiation. The visible discontinuity at about 330 nm in the right hand panel of Figure 6.4 is due to the discontinuity in Equation 6.3, however it does clearly show that proportionally, more of the transmitted erythemally effective radiation is in the UVA than is incident. This is because sunscreens are designed prevent burning, so mainly focus on blocking the UVB.

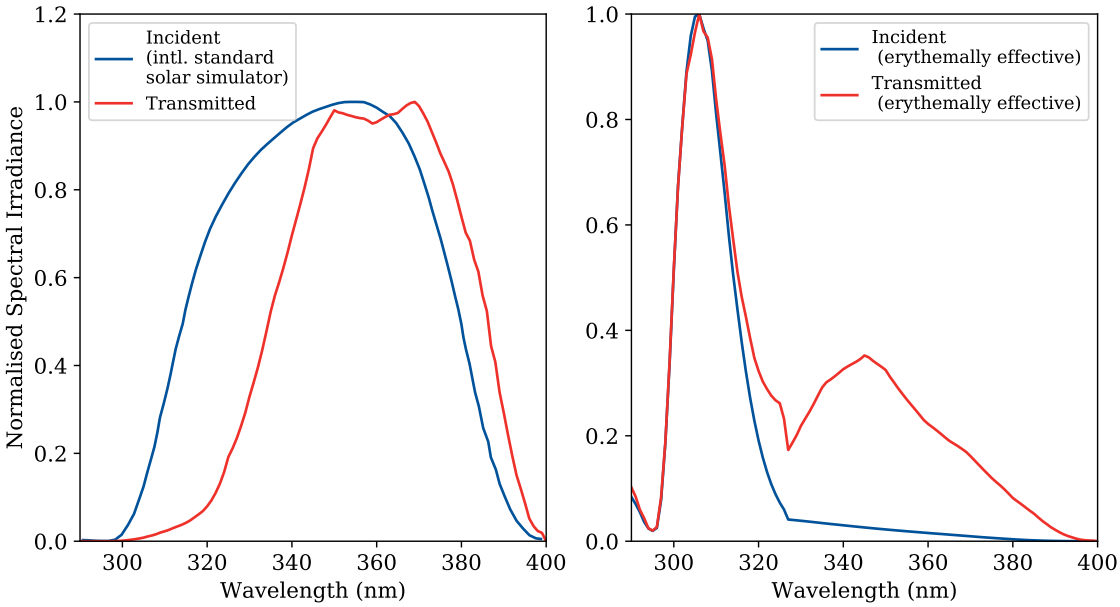

Figure 6.4: *The left panel shows a normalised incident and transmitted spectrum of a solar simulator (the incident spectrum is extracted from Herzog & Osterwalder [97]. The transmitted spectrum is the results of the simulation through a high SPF film as reported in Table 6.1. The right panel shows the same results multiplied by erythemally effective factor as described by Equation 6.3 (the discontinuities are due to discontinuities in Equation 6.3).*

6.3 Grid MCRT

6.3.1 Methods

The aim of the code development was simulate a sunscreen film that could be added to the skin model as described in previous chapters. In order to do, so a stand alone sunscreen film was simulated using the grid code, and the theoretical SPF this film affords compared against published results. To simulate this film of sunscreen with the grid code, again the optical properties of the sunscreen and the sunscreen film geometry were determined. This time, they are implemented using the voxellised grid model.

Optical properties

The simulation aimed to reproduce results published by Herzog & Osterwalder [97] testing the SPF of various dilutions of a premix UVR filter concentrate (containing 20% EHMC, 20% DHHB (diethylamino hydroxybenzoyl hexyl benzoate), 6% EHT (ethylhexyl triazone) and 5% BEMT (bemotrizinol)). The results presented in reference [97] provide *in vivo* SPFs for a wide range of different total filter concentrations, in addition to the *in silico* results presented. The filter concentrations examined in reference [97] and used in the simulations performed here are presented in Table 6.5.

The extinction of the constituent filters of the premix (and of the premix at different concentrations) used in reference [97] is shown in Figure 6.5.

% Premix	Filter Conc. [97]	SPF in vivo	*In silico* [97]
6	1.2% EHMC, 1.2% DHHB, 0.36% EHT, 0.3% BEMT	6.5	6.1
10	2% EHMC, 2% DHHB, 0.6% EHT, 0.5% BEMT	10	9.8
15	3% EHMC, 3% DHHB, 0.9% EHT, 0.75% BEMT	17.6	14.8
20	4% EHMC, 4% DHHB, 1.2% EHT, 1% BEMT	20.9	19.8
25	5% EHMC, 5% DHHB, 1.5% EHT, 1.25% BEMT	30.4	25.0
30	6% EHMC, 6% DHHB, 1.8% EHT, 1.5% BEMT	35.0	30.2
50	10% EHMC, 10% DHHB, 3% EHT, 2.5% BEMT	48.8	51.0

Table 6.2: *This table presents the filter compositions used to test the performance of an existing sunscreen simulator, and are used to test the simulation approaches presented here (the MC no-grid code as described above, and the grid code MCRT approach). The leftmost column details the dilution of the premix (containing 20% EHMC, 20% DHHB (diethylamino hydroxybenzoyl hexyl benzoate), 6% EHT (ethylhexyl triazone) and 5% BEMT (bemotrizinol) used, absorption of the filters is shown in Figure 6.5.*

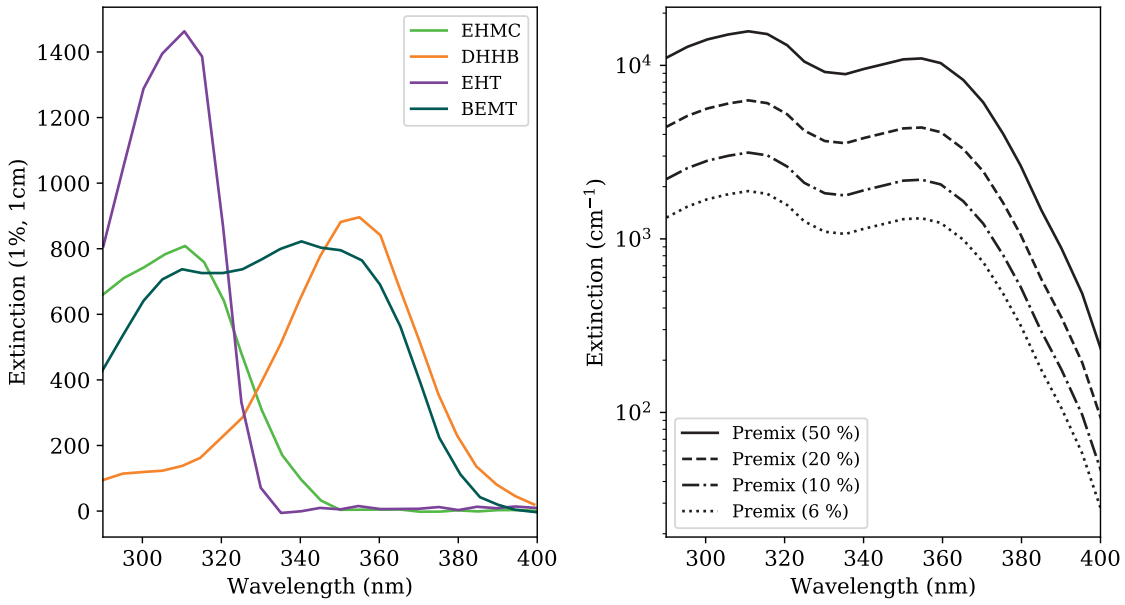

Figure 6.5: *The left panel shows the absorbance of the three constituent filters of the premix sunscreen as used by Herzog & Osterwalder [97] to demonstrate efficacy of a sunscreen simulator. The premix comprises 20% EHMC, 20% DHHB (diethylamino hydroxybenzoyl hexyl benzoate), 6% EHT (ethylhexyl triazone) and 5% BEMT (bemotrizinol). The right panel shows the absorbance of each of these filters at a 1% concentration (weight by volume), and the right panel shows this premix at a selection of the dilutions used in the Table 6.2.*

The filter extinction coefficients of the constituent filters were extracted from data published by Osterwalder & Herzog [92] and checked against a known dataset (personal communication) [109]. Voxels containing the sunscreen (see the next section for geometry) had the optical properties applied, and the remaining voxels were left empty.

Geometry

The depth (z) resolution of the grid voxels was 1 μm and a small patch of sunscreen of surface area 0.5 mm $\times$ 0.5 mm was used for the simulation. By applying repeating boundaries, the model simulated an infinite sunscreen film. The grid design used is detailed in Table 6.3.

Dimension	Size	Number of Voxels	Resolution
x	0.05 mm	50	10 μm
y	0.05 mm	50	10 μm
z	0.02 mm	200	1 μm

Table 6.3: *Specifications of spatial grid used to simulate a film of sunscreen.*

To find the shape factor to produce the film thickness profile, Equation 6.10 is taken from [97], where $\gamma_{\text{total},\%}$ is the total percentage (weight by volume) of the filters present in the sunscreen, and the parameters $p1 = 0.33$, $p2 = 0.69$, $p3 = 0.89$, $p4 = 1.95$ and $p5 = 0.5$ have been determined within reference [97]. The original form of Equation 6.10 contains an oil phase term, which accounts for synergistic effects between the water phase and the oil phase of UVR filters. However to calculate this, the extinction profile in the oil phase is required, and this data was not accessible.

$$c = p1 + p2(\gamma_{\text{total},\%}/(\gamma^{p3}_{\text{total},\%} + p4) + p5/4 + \text{oil phase term} \tag{6.10}$$

Equation 6.10 was used to calculate values of c for each of the filter concentrations shown in Table 6.2. The Python SciPy Stats package was used to create film profiles for each value of c, which were read into the Fortran 90 code. It is assumed for the purposes of this simulation that the applied amount is 2 mg cm^{-2}, that the surface of the sunscreen film is flat, and that there are no 'holes' or areas of total depletion of sunscreen. To simulate the sunscreen film, while looping over the top layer x and y, at each voxel, an h value is randomly sampled from the profile corresponding to the premix dilution under test. This is used in Equation 6.7 to determine a z-depth, and these voxels are assigned the sunscreen optical properties. An example of the sunscreen film in voxel representation is shown in Figure 6.6.

Simulation & data analysis

The input spectrum is, again, the international standard solar simulator as used by Osterwalder and Herzog [92]. Simulations were run with 10^9 packets. Packets exiting the bottom of the grid (and so would be incident on skin, if the sunscreen film was on skin) are binned by wavelength, and used within Equation 6.9, as before.

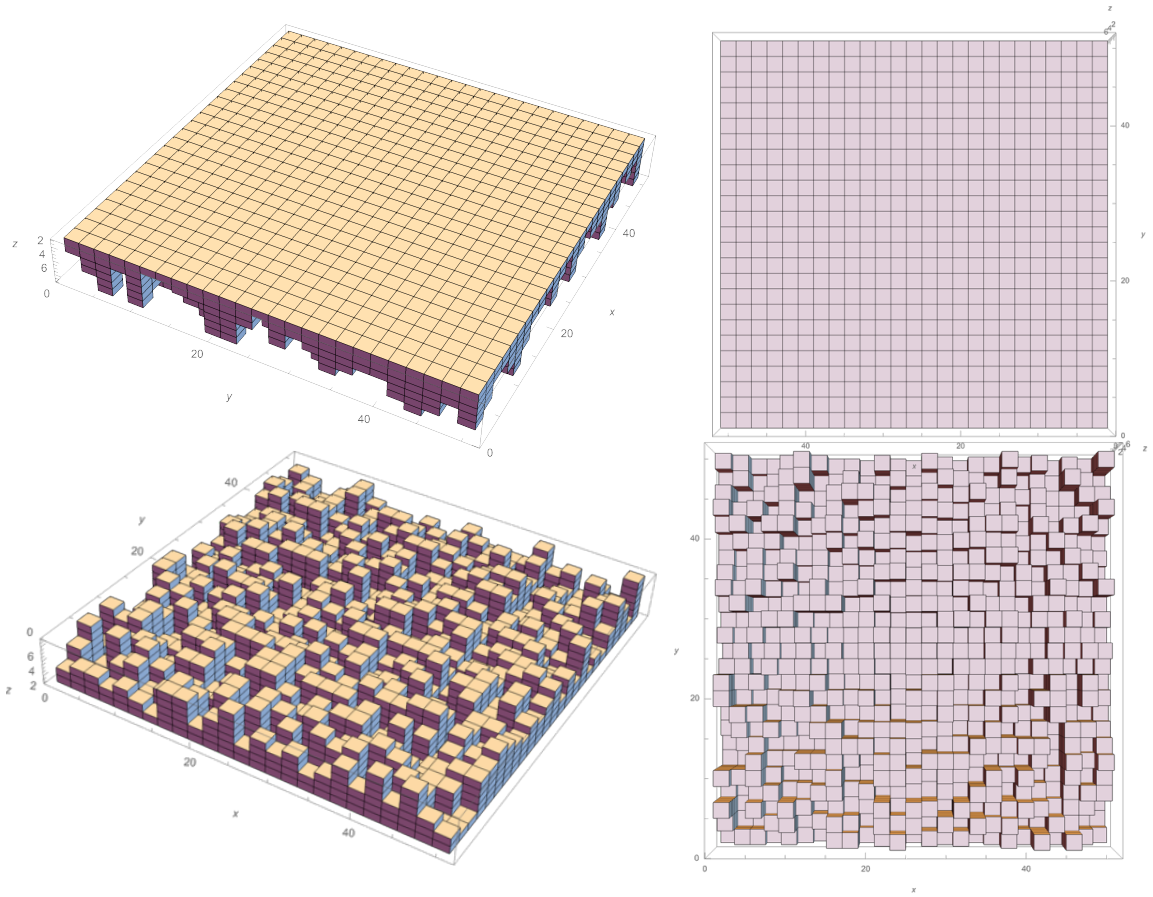

Figure 6.6: *Voxelated representation of the sunscreen film. The top views show the smooth surface of the film, and the bottom images show the base of the film, as in contact with the skin surface. All axes here are marked in voxels.*

Results

Table 6.4 compares results obtained from the grid code against the previously published results [97].

% Premix	Filter Conc. [97]	SPF in vivo	*In silico* [97]	MC No Grid	MC Grid
6	1.2% EHMC, 1.2% DHHB, 0.36%EHT, 0.3% BEMT	6.5	6.1	5.9	6.4
10	2% EHMC, 2% DHHB, 0.6%EHT, 0.5% BEMT	10	9.8	9.4	9.86
15	3% EHMC, 3% DHHB, 0.9%EHT, 0.75% BEMT	17.6	14.8	14.4	16.4
20	4% EHMC, 4% DHHB, 1.2%EHT, 1% BEMT	20.9	19.8	19.0	19.9
25	5% EHMC, 5% DHHB, 1.5%EHT, 1.25% BEMT	30.4	25.0	24.3	28.1
30	6% EHMC, 6% DHHB, 1.8%EHT, 1.5% BEMT	35.0	30.2	29.9	32.3
50	10% EHMC, 10% DHHB, 3%EHT, 2.5% BEMT	48.8	51.0	49	49.6

Table 6.4: *This table compares results testing the performance of an existing sunscreen simulator against results testing the MC no-grid code as described above, and the grid code MCRT approach. The leftmost column details the dilution of the premix (containing 20% EHMC, 20% DHHB (diethylamino hydroxybenzoyl hexyl benzoate), 6% EHT (ethylhexyl triazone) and 5% BEMT (bemotrizinol)) used, absorption of the filters is shown in Figure 6.5.*

Figure 6.7 shows comparison between results from the MCRT grid code to those from the published work [97] (and the no grid MC code described in the previous section).

Discussion

The existing sunscreen simulator appears to underestimate the SPF, apart from at a high filter concentration (Figure 6.7). The grid code appears to perform better in estimating the *in vivo* SPF. It could be this is due to a simple increase in path lengths in the grid code. If the film thickness profile is describing the real shape of the film on the skin, then using this profile in the Beer-Lambert law (6.4 will only correctly reproduce the physical distance travelled by photons at normal incidence. Photons at non normal incidence may, on average, travel a further physical distance, so encounter a greater optical depth and are therefore be more likely to be absorbed at a shallower physical depth.

The film profile was chosen to be random film height samples in x & y (that fit the film profile heights from Equation 6.10). During conversations with sunscreen formulators at the 17$^{\text{th}}$ International Conference of Photobiology (also 18$^{\text{th}}$ Congress of the European Society of Photobiology, Light & Life 2019, Barcelona, Catalonia), they explained the topography of the skin is so jagged at

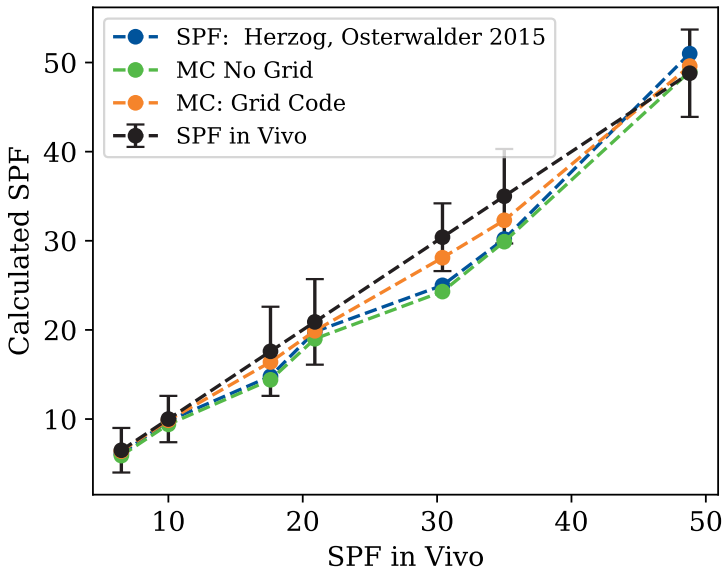

Figure 6.7: *Simulated vs in vivo SPF. This is a plot of the data presented in Table 6.2, obtained from the sunscreen MCRT grid code, using varying concentrations of a UVR filter premix (containing 20%EHMC, 20% DHHB, 6% EHT and 5% BEMT).*

small scales that a random choice of depths might better simulate sunscreen than a smooth film. However because of how films form, there will be areas of continuous films.

Ideally, if a good topographic image of sunscreen film on human skin could be obtained, this could be used to determine a real geometry for the sunscreen film under simulation. Vehicle composition is likely also important in sunscreen film formation (this is not captured by Equation 6.10), so different formulations with the same filter composition may have different film profiles. If *in silico* simulations were found to be so improved by the use of 'real' geometry that they could be used in place of *in vivo* SPF testing, then in future, humans may still need to be retained within the workflow for *in silico* SPF determination. For example, by taking a topographic image of a sunscreen film applied on a human volunteer, this film geometry could then be used within an MCRT simulation to determine the SPF of a given sunscreen. Although this would not remove the use of humans entirely, it could remove the harmful element of SPF testing.

6.4 Simulating effect of sunscreen on DNA damage

After obtaining good agreement between the sunscreen film MCRT and published results, the next stage was to combine the 3D film of sunscreen with the 3D skin model.

6.4.1 Methods

6.4.2 Code validation

In order to validate any theoretical results from the model, it was adapted to simulate the experimental setup from Young et al. [110], where the protective effects of application of different amounts of a high SPF sunscreen were investigated by quantifying CPD in the basal layer (and in the epidermis overall). The grid setup and skin layer separations were exactly as described in Chapter 5, as the experiments in Young et al. [110] were performed on buttock skin, and the irradiation source was the same solar simulator as shown in Figure 5.1.

6.4.3 Sunscreen

The sunscreen under test in reference [110] was stated as having an *in vivo* SPF of 65±15.8, and ingredients listed as MBBT (bisoctrizole), DBT (diethylhexyl butamido triazone), BEMT(bemotrizinol) and BMDBM (avobenzone). However, percentages or proportions of the ingredients were not listed. The existing available sunscreen simulators [107, 108] were used to vary the filter percentages of this combination of filters until an SPF match was found. An acceptable match of 7% MBBT, 5% DBT, 5% BEMT and 2.5% BMDBM was found, which gave a predicted SPF=64.8. The constituent filters and effect of the combined mixture is shown in Figure 6.8.

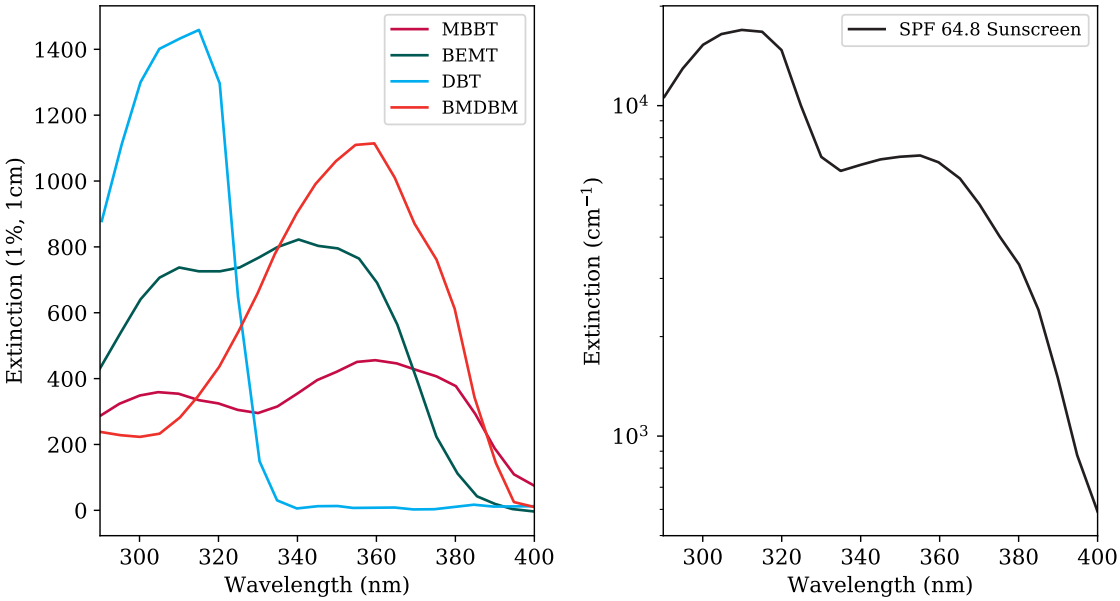

Figure 6.8: *The left panel shows the absorbance of the three constituent filters of the high SPF sunscreen used by Young et al. to investigate photoprotection by sunscreen in vivo. The sunscreen is assumed to comprise of 7% MBBT, 5% DBT, 5% BEMT and 2.5% BMDBM.*

The experimental work in [110] investigated the effects of optimal application ($2\,\mathrm{mg\,cm^{-2}}$) and effects of sub optimal application ($0.75\,\mathrm{mg\,cm^{-2}}$). Using the SciPy stats package, a film profile was built (using Equation 6.10 to find c). A layer of sunscreen voxels were added to the top of the skin

model.

Simulations were run with 10^8 packets (for the model representing skin types I & II) . In the experiment, 4 SED were used on unprotected skin, and 30 SED for protected, in order to simulate real life behaviour. This was reproduced in the simulation by multiplying the irradiance for the unprotected simulation by 4, and by 30 for the simulation including the sunscreen.

In order to investigate the effect of sunscreen on DNA damage in skin type VI, the simulations were repeated (using 10^9 photons, for better signal to noise). In order to investigate whether the solar simulator provides a suitable simulation for true solar radiation in sunscreen testing, the simulations were repeated with the solar spectrum used in Chapter 4.

Data analysis

Following the methods described in Chapter 5, the fluence incident on the basal layer was extracted and the methods described in Chapter 4 applied to estimate the relative CPD yields within the basal layer.

6.4.4 Results

Results comparing the CPD yield in the basal layer of skin type I/II are shown in Table 6.5 and compared to experimental results.

	Experimental Results [110]		Simulation Results	
	0.75 mg cm^{-2}	2 mg cm^{-2}	0.75 mg cm^{-2}	2 mg cm^{-2}
$\frac{\text{CPD}_{\text{protected}}}{\text{CPD}_{\text{unprotected}}}$	0.85	0.33	0.95	0.31

Table 6.5: *Basal layer CPD yield estimated by simulations and basal layer CPD yield as published by Young et al. [110].*

Table 6.6 shows the CPD yields across both skin types simulated, and across both solar and solar simulated irradiation.

	Solar Simulator		Mediterranean Sun	
	0.75 mg cm^{-2}	2 mg cm^{-2}	0.75 mg cm^{-2}	2 mg cm^{-2}
SPT I/II $\frac{\text{CPD}_{\text{protected}}}{\text{CPD}_{\text{unprotected}}}$	0.95	0.31	0.92	0.33
SPT VI $\frac{\text{CPD}_{\text{protected}}}{\text{CPD}_{\text{unprotected}}}$	0.32	0.11	0.34	0.11

Table 6.6: *CPD: comparing the different CPD yield comparisons in different skin types and incident radiation.*

The radiation incident on the basal layer over both skin types, and from both irradiation regimes, is shown in Figure 6.9.

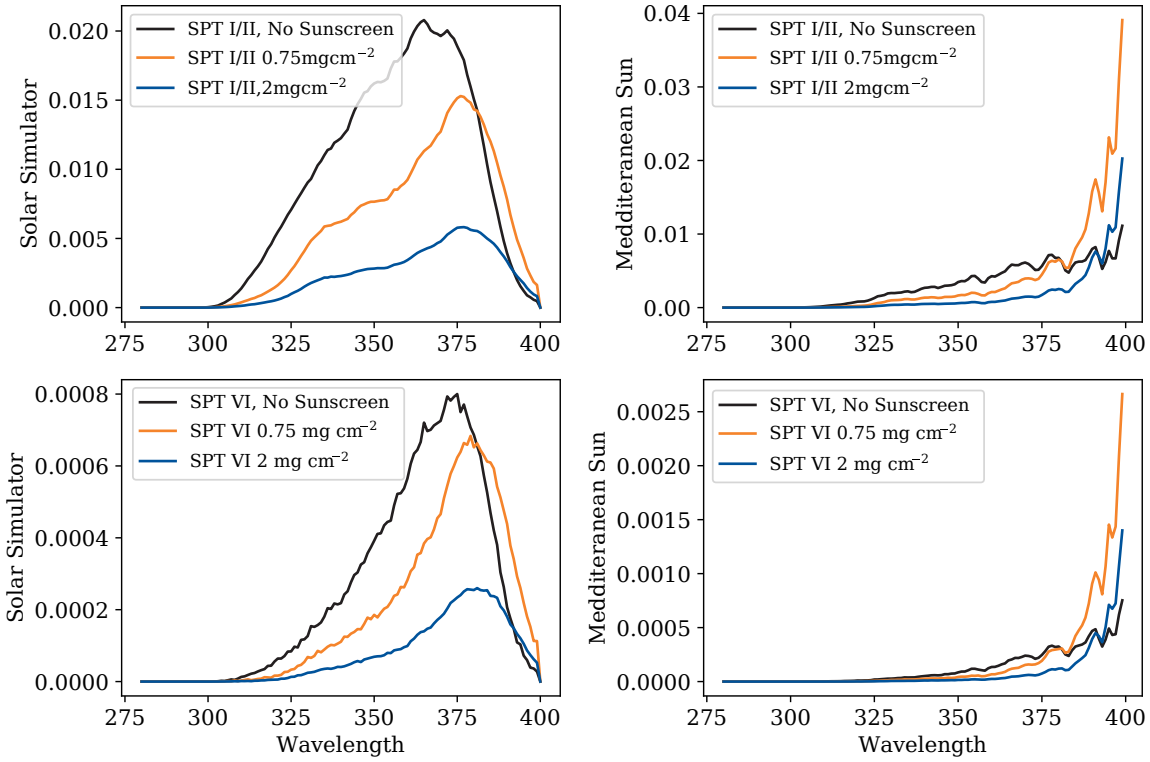

Figure 6.9: *Radiation incident on the basal layer for both skin types simulated, and with solar and solar simulated radiation.*

6.4.5 Discussion

Table 6.5 shows that there is good agreement between experimental CPD yields [110] and the simulation results, giving confidence that the simulations are representing the wavelength dependent filtering effects of sunscreen (and the resulting reduction in CPD yield) well.

The results presented in Table 6.6 indicate that there is no meaningful difference in the relative CPD yield between results for simulated and solar radiation. It is thought that the use of solar simulated radiation overestimates SPF of a sunscreen during testing. However, as discussed in previous chapters, erythema (the endpoint for SPF testing) and CPD yield in the basal layer are not the same, as CPD induced throughout the epidermis are thought to be responsible for erythema [5]. It may be concluded from these theoretical results that solar induced basal layer CPD yield may be well simulated by solar simulated radiation, however this requires further investigation. For example, testing simulations against several sunscreens (with *in vivo*) with both solar and solar simulated radiation would confirm these.

From the theoretical results, it appears that relatively speaking, sunscreen on skin type VI is more protective against DNA photodamage than in skin types I & II. Skin type VI appears to enjoy a 3 fold boost in the photoprotective effects from wearing sunscreen. This may be due to the multiplicative effects of filtering via the sunscreen, and the melanin distributed throughout the skin type VI epidermis.

One implication of sunscreen use on darker skin types has been identifying the impact on the ability to synthesise vitamin D. Future investigation could aim to use an MCRT model of the transport of radiation through sunscreen films applied to darker skin to quantify the reduction in CPD yield compared to the reduction in ability to synthesise vitamin D, in order to quantify health benefits vs risks in sunscreen use by darker skinned populations.

One obvious limitation of the work presented here is that the work simulated very few sunscreen formulations. This was due to limited amounts of published data on experimental results and sunscreen formulations. Subsequent to completion of this work, a new FDA ruling now ensures sunscreens sold over the counter in America are labelled with their constituent UVR filter concentrations. This change will mean work such as this can be extended to cover many more sunscreens.

Another limitation of this work, as discussed in the methods section, is that it is assumed that there are no holes (no areas of complete depletion) in the sunscreen film. This is likely to be an unreasonable assumption as for many reasons, it should be assumed that small breaks develop in the sunscreen film. In addition, larger breaks in sunscreen film could be assumed to occur (the simulations performed here only simulate an area of 1 mm) due to film removal due to friction or sweat. These could be investigated in future work to identify the impact of these in relation to cancer risk.

6.5 Conclusion

Here, a method for simulating UVR transport through a layer of sunscreen on human skin was developed. It was found that the MCRT model reproduces *in vivo* SPF slightly better than existing sunscreen simulators. In addition, the MCRT model was found to represent experimental CPD yields

within the basal layer. The model was developed to simulate CPD yields on sunscreen protected skin type VI, and it was found that relatively speaking, sunscreen affords greater reduction in CPD yield skin type VI skin than in skin type I/II. This is likely due to the additional effect of melanin distribution in skin type VI.

Chapter 7

Spectrally and spatially resolved depth penetration achieved by phototherapy lamps

Synopsis

The work presented in this chapter was motivated by clinicians at Ninewells Hospital and Medical School, Dundee, who wished to determine quantitatively if utilising UVA1 phototherapy radiation within a photochemotherapy protocol could be an effective treatment. Existing phototherapy treatments are safe and evidence based, and as such, UVA1 photochemotherapy would only be considered for use in patients where other approaches have failed.

Current best practise and limitations of phototherapy will be briefly discussed. This chapter goes on to describe a simulation led approach (using MCRT) to estimate the depth of penetration into skin tissue achieved by radiation emitted by phototherapy lamps. Both healthy and diseased skin tissue were simulated. Using these spectrally and spatially resolved results for each lamp, the best lamp for maximal UVR penetration can be identified.

A summary of this work has been published in the British Journal of Dermatology, titled 'Could psoralen plus ultraviolet A1 (PUVA1) work?' [33]. As far as we know, psoralen plus UVA1 ('PUVA1') therapy has not yet been investigated as a treatment for certain conditions that are resistant to other approaches. Our simulations indicate PUVA1 could work, and as such have provided theoretical justification for clinicians to move towards a clinical trial of PUVA1.

7.1 Introduction

Phototherapy and photochemotherapy use UVR to treat skin diseases such as psoriasis, an autoimmune disease causing skin inflammation and irritation. Psoriasis is characterised by a faster turnover time of keratinocytes in the skin. Rather than taking the normal 25-30 days to mature and shed, keratinocytes in psoriatic skin mature after 3-5 days [111]. This fast cell turnover means mature,

keratinised skin cells reach the surface of the skin at a faster rate than the cells are able to shed. This leads to a build up of dead skin cells at the surface of the skin, resulting in skin scaling and inflammation. Severity of psoriasis can range from mild to severe, and can have significant impact on the quality of life of a sufferer.

The use of sunlight to treat skin disease has a long history, both in conjunction with photosensitive plant extracts, and sunlight alone [18, 112, 113]. The first UVR lamp for medical treatment was invented in 1896, beginning the practice of phototherapy within the hospital environment [112, 113].

Both phototherapy and photochemotherapy treat psoriasis by interrupting the accelerated cell life cycle. These UVR based treatments are typically provided in a clinical setting, although in Scotland a clinically managed home phototherapy service is available [114, 115]. Within a clinically managed service, UVR exposure is carefully calibrated and monitored. The treatment unit consists of fluorescent lamps and the quantity of UVR exposure is varied by altering the exposure time. Therapeutic doses may be delivered in times as short as 15 seconds.

7.1.1 Phototherapy

The majority of phototherapy performed in the UK uses narrowband ultraviolet B radiation (NB-UVB), so called due to the small range of wavelengths emitted by the lamp, as shown in Figure 7.1.

NB-UVB radiation peaks at $\lambda = 311$ nm with a full width at half maximum (FWHM) of about 2 nm. NB-UVB has been in use in Europe since the invention of the Philips TL01 lamp in 1988[1], however due to regulatory requirements, it was only introduced in the US in 1998. Broadband UVB phototherapy lamps are still in use in some settings [116], however for psoriasis NB-UVB is considered a superior treatment [117]. NB-UVB therapy is highly effective and currently considered safe. To date, no increased risk of skin cancer due to NB-UVB therapy has been found [118]. As NB-UVB lamps were introduced in 1988, and skin cancer can develop over timescales of decades; this is an area of ongoing research [117].

NB-UVB phototherapy works by locally damaging DNA which induces immunosuppression [117, 119]. To summarise, the photons emitted by the NB-UVB lamp carry enough energy to cause direct DNA damage. This direct DNA damage has several effects, including the up-regulation of p53; known as 'the tumour suppressor gene'. When p53 is up-regulated this can arrest the natural cell cycle, or even cause the cell to die [69, 75, 120]. The mechanisms by which NB-UVB immunosuppression is achieved are complex, and not fully understood [119] however current understanding is described in detail by Beissert et al. [121], and with specific reference to skin diseases, by Schneider et al. [117].

Given that phototherapy works by directly damaging DNA, and given the explanations of photocarcinogenesis from previous chapters, this raises the question as to why NB-UVB therapy shows no increased risk of cancer. The reason may be the very short exposure times required for therapeutic effect. Immediate, direct DNA damage does occur, arresting the accelerated cell cycle. However without prolonged exposure, DNA repair may be able to take place before replication occurs. It is this process of replicating damaged DNA which can lead to mutations and eventually cancer.

[1] More information on the Philips TL range is available at `https://www.lighting.philips.com/main/products/special-lighting/phototherapy`

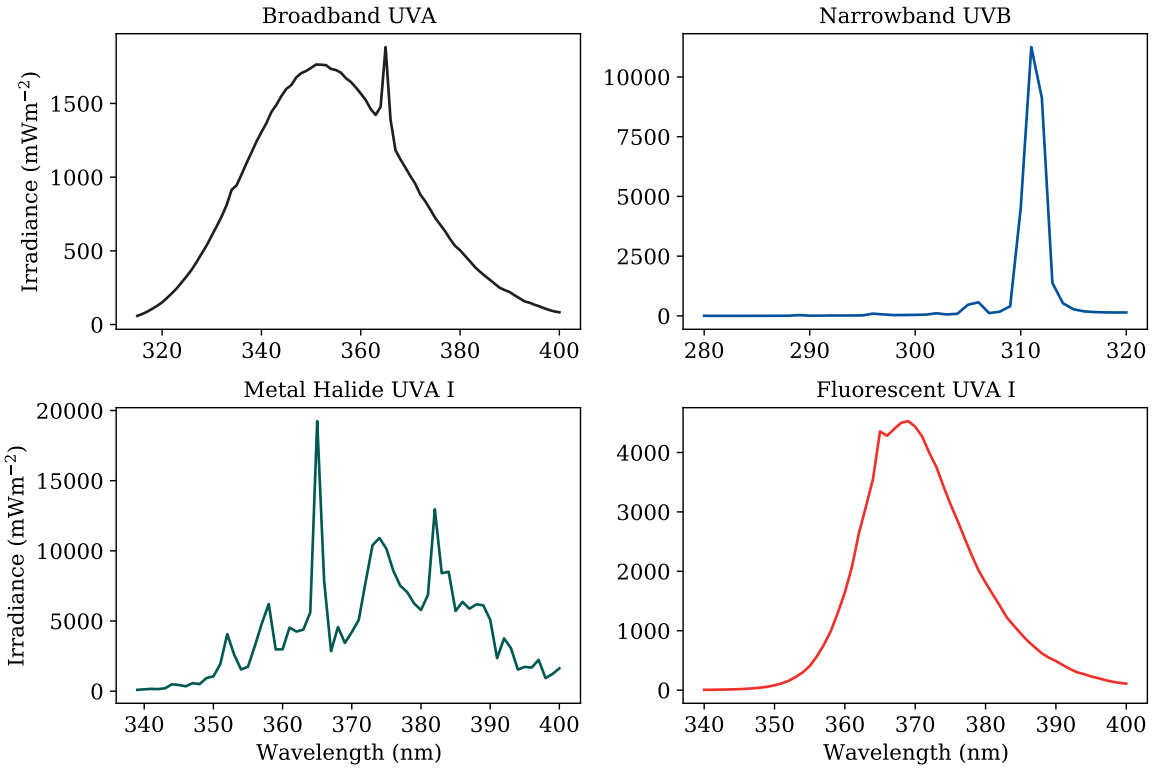

Figure 7.1: *Spectra of the four phototherapy lamps investigated. Broadband UVA is the standard lamp used for PUVA treatment. Narrow-band UVB (NB-UVB) is the standard lamp used for phototherapy across Europe. The Fluorescent UVA1 and the Metal Halide UVA1 lamp both emit radiation over the same range, and are both used in UVA1 monotherapy. The peak wavelengths are found at λ=351 nm for broadband UVA, λ=311 nm for NB-UVB, and λ=365 nm for the UVA1 lamps. All lamps exhibit the characteristic mercury line at 365 nm, however the peak for Broadband UVA is considered to be at the centroid of the smooth broadband radiation (rather than at the sharp mercury peak).*

7.1.2 Photochemotherapy

Although nowadays most phototherapy in Scotland is performed using NB-UVB lamps, this has only been the case since the late 1980s. Prior to the invention of the TL01 lamp, photochemotherapy was the standard radiation based psoriasis treatment. Photochemotherapy is phototherapy using both ultraviolet A radiation (UVA) and a photosensitiser (introduced to the skin either topically, via a cream or bath, or systemically, using oral medication). The radiation source used is a broadband UVA source, shown in Figure 7.1. The photosensitiser used will belong to the psoralen family of drugs, hence the name PUVA - P(soralen) plus UVA.

Psoralens are a family of molecules which can be used as photosensitisers. Psoralens are mutagens (an agent that can alter DNA), which bind with DNA. The resulting molecule is reactive to UVR, hence the photosensitising effect. In addition to being used as as medicine, psoralens are commonly used in molecular biology research as a tool to mutate DNA. The common psoralen used in psoriasis treatment is 8-methoxypsoralen (8-MOP), which was first isolated from the Amma Majus plant in 1947 [18, 112].

Why is PUVA used?

PUVA is often avoided as a first line treatment due to the convenience, safety and effectiveness of NB-UVB, however for certain diseases it is used as a first line treatment [122].

PUVA is often used as a second line treatment in treating a 'standard' presentation of psoriasis if NB-UVB is no longer effective [122]. In this situation, PUVA may work due to additional systemic immunosuppressive effects observed after PUVA treatment which are not observed after NB-UVB treatment [123].

As NB-UVB failure commonly occurs in patients with psoriasis that is thicker than usual, PUVA is recommended as a first line treatment for patients presenting with pustular psoriasis, or psoriasis on body sites that have thicker skin, such as the hands and soles (palmo-plantar presentation) [122]. In addition, PUVA is considered as a first line therapy for patients with a higher skin phototype, as PUVA is more effective than NB-UVB for these patients [122]. In both of these scenarios (thicker psoriasis, or a higher melanin content in the skin) the radiation must penetrate through an optically thicker medium before it reaches the region where therapeutic effect can be achieved.

There are two components to PUVA therapy: the photosensitiser, and the radiation. Efficacy of the treatment therefore involves both effective distribution of the photosensitiser within the skin, and successful penetration of wavelengths of radiation that will activate the photosensitiser.

When PUVA fails: the case for PUVA1

UVA1 refers to the near-visible waveband within UVA radiation (340 nm to 400 nm). The dermatology department at Ninewells Hospital and Medical School, Dundee, is one of only 3 places in the UK where UVA1 monotherapy is offered [124]. UVA1 monotherapy may be used to treat dermatoses such as graft versus host disease, and a variety of sclerosing (stiffening) skin diseases [124, 125, 126]. UVA1 monotherapy is not currently recommended in the treatment of pustular psoriasis [125, 127], however a pilot study suggests it may be a promising treatment [128]. UVA1

is rarely indicated- roughly 80% of phototherapy treatments in Scotland are now NB-UVB, with 18% PUVA and 3% UVA1 (figures courtesy of Photonet, the Managed Clinical Network for UVR Phototherapy in Scotland).

The penetration depth achieved by radiation incident on the skin is wavelength dependent, and longer UVR wavelengths penetrate deeper into the tissue. One reason PUVA works when NB-UVB fails may be, in part, to the advantageous penetration offered by the Broadband UVA source used for PUVA [129].

For some diseases, such as palmoplantar pustular psoriasis, neither PUVA nor NB-UVB is effective. If PUVA fails, current treatments that might be attempted include Grenz ray therapy, systemic retinoids or systemic immunosuppression. Systemic treatment can have serious side effects. One reason for PUVA failure could be that the radiation cannot penetrate deep enough into the skin to produce therapeutic effect. This provides justification to investigate whether UVA1 lamps, having a longer peak wavelength, are able to reach greater depth in the skin, and are sufficiently absorbed by psoralen–DNA complexes to provide clinical benefit beyond that achieved using standard broadband UVA photochemotherapy.

7.2 Methods

The code described in Chapter 3 required small modifications to investigate whether psoralen plus ultraviolet A1 (PUVA1) could work.

Incident spectra used are shown in Figure 7.1 (and are combined in the same plot in Figure 7.2). All lamps were considered to have a diffuse output (as described by Equation 4.1).

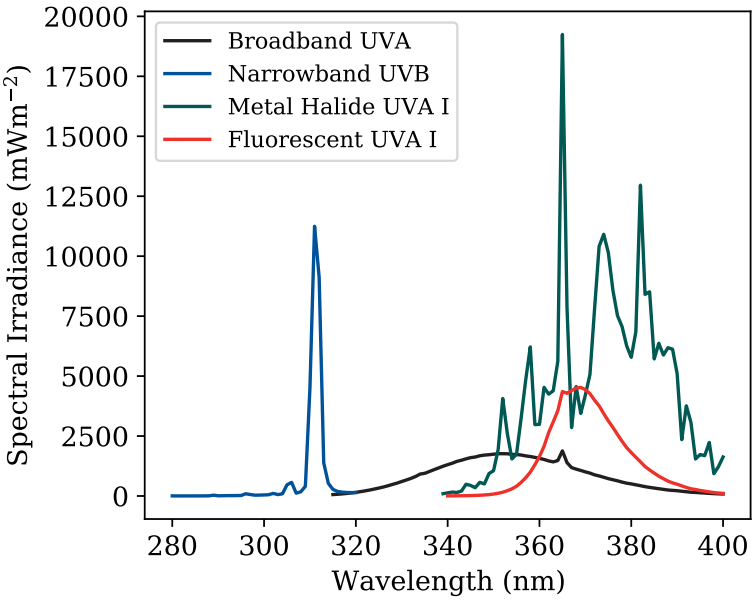

Figure 7.2: *Spectra of the four phototherapy lamps investigated shown on one plot, for comparison.*

7.2.1 Depth resolution of the epidermal layers

The code developed and described in Chapter 3 has a z (depth) resolution of 10 μm. Initial investigations indicated this was too large to clearly distinguish between the penetrations achieved by the different lamps, and so the z (depth) resolution of the model was increased to 1 μm, as was done in Chapters 5 and 6. The grid design used is detailed in Table 5.1).

The depths used are presented in Table 7.1 and are taken from results obtained by experiments performed by Sandby-Møller et al. [44]. Clinicians from Ninewells suggested, as a first approximation, psoriatic skin could be simulated by doubling the thickness of the stratum corneum.

Layer	Depth (Healthy Skin)	Depth (Psoriasis)
Stratum Corneum	14.8 μ m	29.6 μ m
Epidermis	63.7 μm	63.7 μm
Melanin Layer	73.7 μm	73.7 μm
Basal Layer	83.7 μm	83.7 μm

Table 7.1: *Epidermal depths from Sandby Møller et al. [44] for healthy and psoriatic skin (adapted to separate melanin layer from the bulk of the epidermis to simulate non exposed skin). Clinicians at Ninewells indicated that as a first approximation, psoriatic skin could be simulated by doubling the thickness of the stratum corneum.*

7.2.2 Effect of 8-MOP on the optical properties

One clear distinction between this application of the code and any previously modelled system described in this thesis is the addition of the photosensitiser. By nature of the mechanism of action, the photosensitiser will affect the radiation transfer. However it is important to identify the expected size of this effect in relation to the optics of the skin, as if this effect is small enough, it may be neglected.

From a study investigating concentrations of psoralen in skin tissue treated for psoriasis (from both topical and systemic application), the greatest concentration of 8-MOP in the epidermis was found to be 128 pg mm^{-3} [132].

We know that the molar attenuation coefficient of 8-MOP reaches a maximum in the UVC of 2.5×10^4 M^{-1} cm^{-1}. In clinical practice, within the range of UVR wavelengths used for photochemotherapy, the highest relevant molar attenuation coefficient of 8-MOP lies at about 303 nm, and it is 1.25×10^4 M^{-1} cm^{-1}. These values are obtained from the datasets presented in Figure 7.3 [130, 131].

8-MOP has a molecular weight of 216 g M^{-1}. If the maximum concentration found in the epidermis is 128×10^{-12} g mm^{-3}, then the molar concentration is 5.9×10^{-13} M mm^{-3}. The volume of skin simulated is 1×10^{-4} cm^{-3}, or 0.1 mm^{-3} (0.05 cm $\times$ 0.05 cm $\times$ 0.04 cm). This means the maximum number of moles of 8-MOP that could be present in the simulated volume of skin would be 5.9×10^{-12} M. This gives a maximum possible extinction coefficient of 7.37×10^{-8} cm^{-1}. This is many orders of magnitude lower than any of the optical properties used to simulate radiation transfer through the skin. As a result the contribution to absorption from 8-MOP has not been taken into account within the radiation transfer simulations.

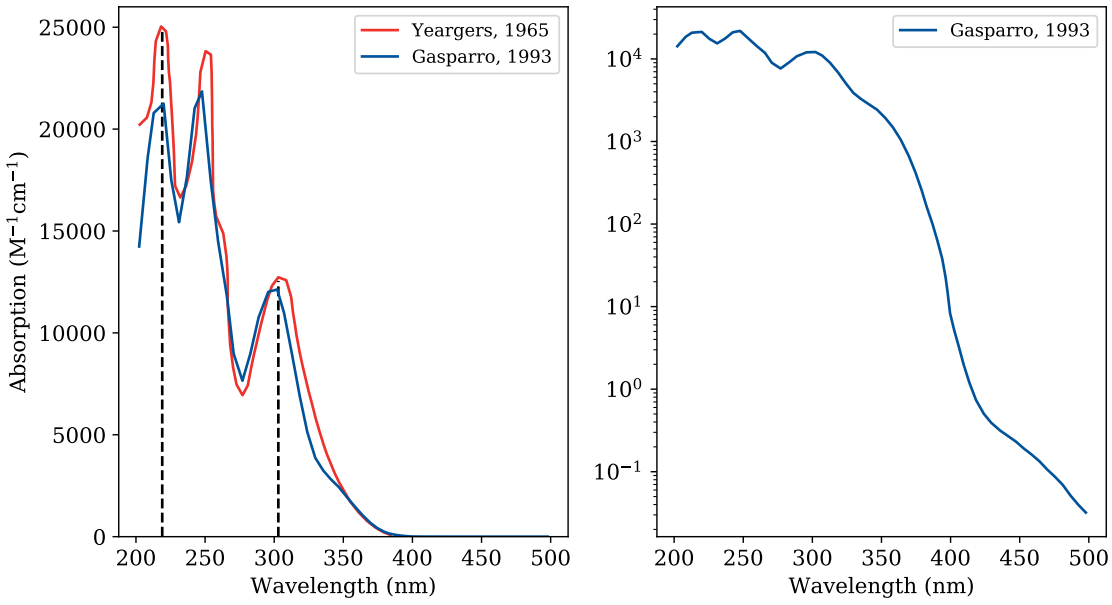

Figure 7.3: *Data for absorption of raw 8-MOP, reproduced from data from Yeargers et al. [130] (8-MOP in aqueous glycerol) and Gasparro et al. [131] (8-MOP in ethanol). The positions of maximum absorption are indicated with dashed lines. The second panel shows the data as presented by Gasparro et al., who present evidence of photoproducts of DNA and 8-MOP after irradiation with visible light. The absorption of 8-MOP in ethanol is presented on a log scale to make this non zero absorption in the visible range clear.*

Data analysis

Initial simulations were performed with a model for non-exposed Fitzpatrick type II (Caucasian) skin. A simulation using 10^8 power packets was run for both healthy and diseased skin for each of the four lamps under investigation, producing 8 datasets in total. Data was extracted from the path length counters in each voxel via the methods described in Chapter 4.

As in previous chapters, the raw data produced by each of the simulations comprised a 4-D dataset (a hypercube comprising 3 spatial dimensions, x, y and z, each discretised onto a grid, and one wavelength dimension- the UVB & UVA wavebands, discretised into 1 nm bins). Each dataset contained 121×10^6 datapoints (121 points for each of the 1×10^6 voxels). Thus each voxel contains the spectrally resolved fluence in that voxel, obtained using the path length counter method.

These datasets were interrogated in several ways to identify whether there is additional penetration depth provided by UVA1 phototherapy radiation that could be utilised to provide clinical benefit beyond broadband UVA photochemotherapy.

By summing each dataset over all wavelengths, and over both lateral dimensions (x and y) as shown in Equation 7.1, this produces a dataset quantifying the penetration of radiation through the skin.

$$\psi_z = \sum_{\lambda=280}^{400} \sum_{i=1}^{50} \sum_{j=1}^{50} \psi_{i,j,k}(\lambda) \tag{7.1}$$

Where $\psi_{i,j,k}(\lambda)$ is the fluence at voxel $\{i, j, k\}$.

7.3 Results

The results in Table 7.2 present the (interpolated) depth, measured from the surface of the skin, reached by 50% and 10% of the total integrated incident radiation.

Lamp	Healthy Skin		Psoriatic Skin	
	Depth (50%)	Depth (10%)	Depth (50%)	Depth (10%)
Broadband UVA (PUVA)	37 μm	215 μm	16 μm	65 μm
Narrowband UVB	17 μm	124 μm	14 μm	41 μm
Fluorescent UVA1	45 μm	254 μm	18 μm	83 μm
Metal Halide UVA1	46 μm	251 μm	19 μ m	85 μm
340 nm – 350 nm	33 μm	192 μm	16 μm	57 μm
350 nm – 360 nm	39 μm	220 μm	17 μm	66 μm
360 nm – 370 nm	43 μm	247 μm	18 μm	75 μm
370 nm – 380 nm	47 μm	264 μm	19 μm	88 μm
380 nm – 390 nm	49 μm	262 μm	20 μm	101 μm
390 nm – 400 nm	51 μm	257 μm	20 μm	102 μm

Table 7.2: *Depths, measured from the surface of the skin, reached by 50% and 10% of the total integrated incident radiation for both healthy and psoriatic skin for each lamp. Also shown, for the metal halide UVA1 lamp, are the depths reached by 50% and 10% of the radiation in 10 nm wide wavebands comprising the lamp's output.*

The data shown in Figure 7.4 show the proportion of incident radiation that reaches a given depth, up to 200 μm.

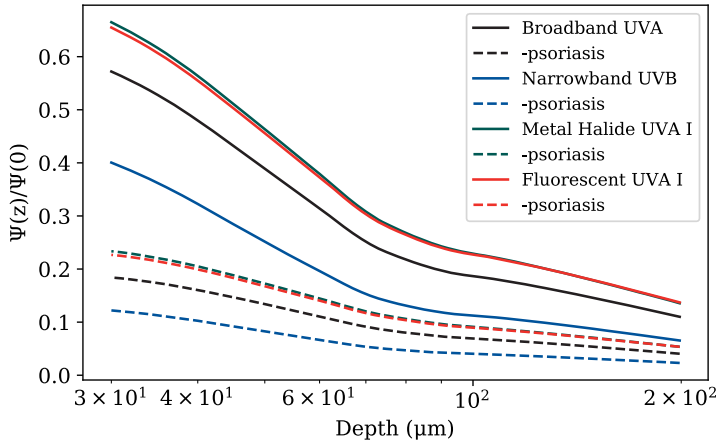

Figure 7.4: *Plot showing the proportion of incident fluence (integrated over all wavelengths) vs penetration depth for both psoriatic and healthy skin for all lamps. These plots were produced from the simulations performed and used 7.1 to produce the image. For clarity, this depth plot begins at 30 μm, excluding the stratum corneum.*

The skin as a filter

To identify whether the radiation reaching deeper into the skin is able to interact with 8-MOP-DNA complexes, the spectral content of the radiation reaching into the psoralen treated skin needed to be recovered. This is possible by analysing the raw data in terms of wavelength.

In this case, to identify the spectra of the radiation that actually reaches the basal layer, a summation over all voxels within the basal layer recovers the total irradiance incident onto those voxels,

$$\psi(\lambda) = \frac{1}{N_{\text{basal}}} \sum_{i,j,k} \psi_{i,j,k}(\lambda) \text{ for } i,j,k \in \text{basal layer} \tag{7.2}$$

where N_{basal} is the number of voxels within the basal layer.

Using results obtained from Equation 7.2, Figure 7.6 shows the theoretical spectrally resolved fluence reaching the basal layer for both the broadband UVA source and the fluorescent UVA1 source. The metal halide UVA1 source exhibits similar behaviour, but due to the irregular shape of the spectra it is harder to see this on a plot (see Figure 7.1). The same results, normalised to the incident spectra, are presented in Figure 7.7.

7.4 Discussion

Figure 7.4 shows radiation penetration up to a depth of 200 μm, so well into the dermis (with reference to Table 7.1), so all cells affected by psoriasis are accounted for within this range. These

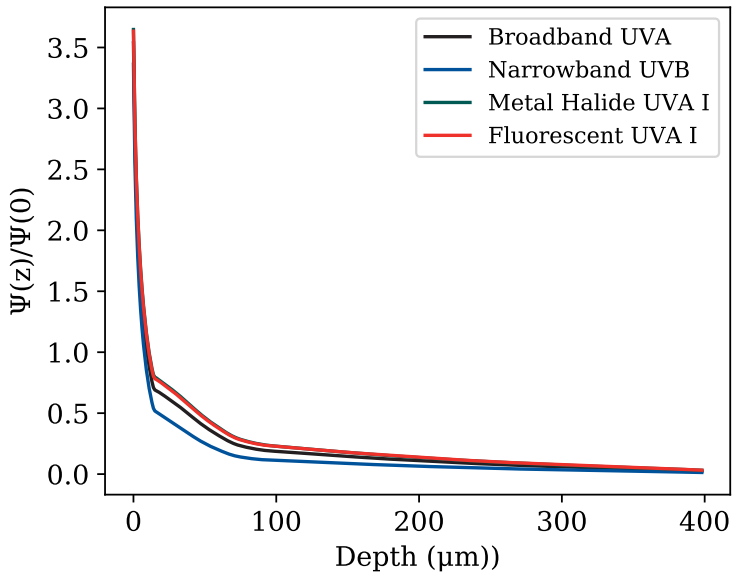

Figure 7.5: *Plot showing the proportion of incident fluence (integrated over all wavelengths) vs penetration depth for healthy skin for all lamps. This image differs from that in Figure 7.4 as this includes the stratum corneum (so effects of back scatter and total internal reflection are evident just under the surface), and the discontinuity at the boundary between the stratum corneum and living epidermis can be seen.*

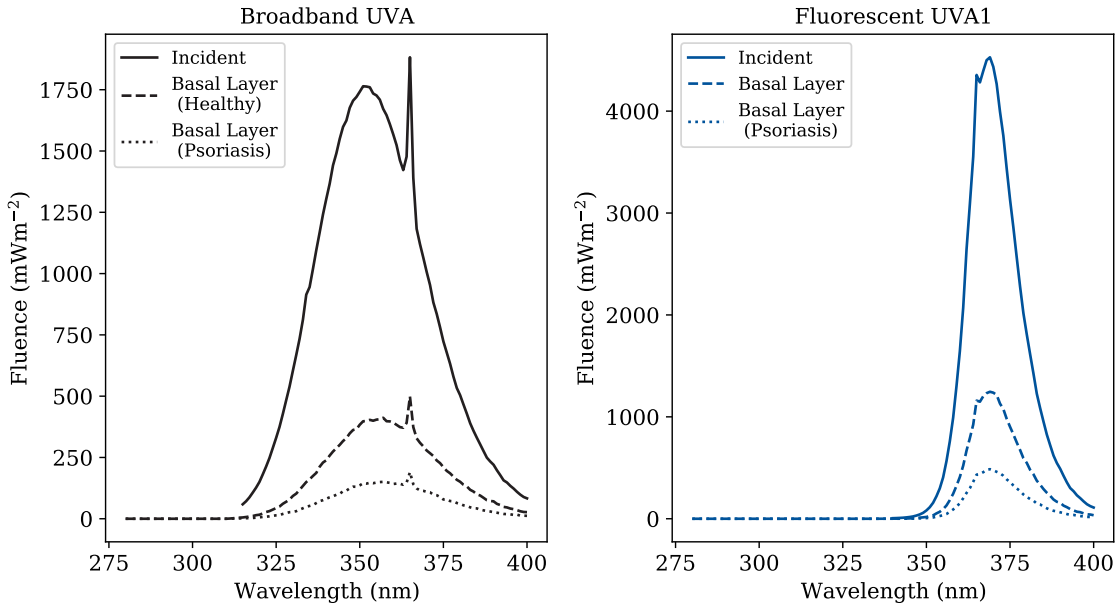

Figure 7.6: *This image shows the absolute irradiance reaching the basal layer of both healthy and psoriatic skin, with reference to the incident dose delivered. This plot was produced using the raw data and Equation 7.2.*

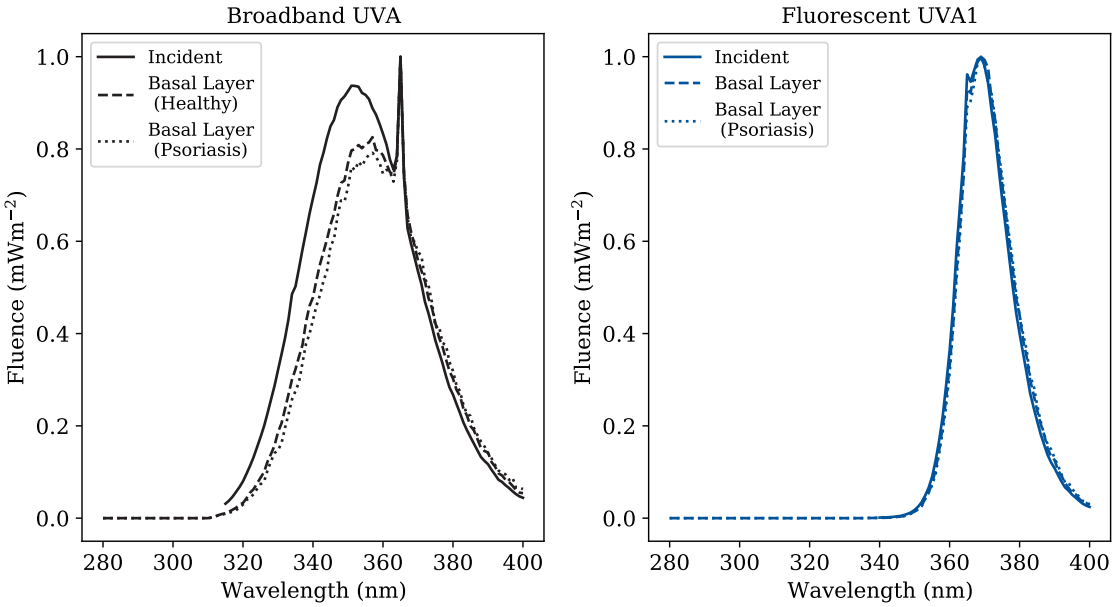

Figure 7.7: *This image shows the same data as presented in Figure 7.6, but in this case each dataset is normalised to the maximum. This is in order to illustrate the shape changes between the spectrum of the incident dose, and the radiation reaching the basal layer.*

results, along with the numbers presented in Table 7.2, clearly indicate a penetration advantage of UVA1 lamps over Broadband UVA. For clarity, the plot in Figure 7.4 begins at 30 μm, and so excludes the values of ψ_z/ψ_0 detected within the stratum corneum. Back-scattering of radiation and total internal reflection cause a build up of radiation just under the surface of the skin, which, if included, makes the difference in penetration depths harder to observe on the graph. In the stratum corneum, the skin cells are dead (so phototherapy/photochemotherapy will not have any biological effect). For completeness, a plot including the stratum corneum, and a linear depth scale, is shown in Figure 7.5.

The results presented in Table 7.2 quantify the depth penetration advantage achieved by UVA1 (both fluorescent and metal halide lamps) over that achieved by broadband UVA and NB-UVB. The advantage is smaller at 50% of incident irradiation, but larger when considering the depth of 10% of the incident irradiation. The depth at which 10% of incident UVA1 source present is 40 μm deeper than for a broadband UVA source. In addition, psoriatic tissue greatly reduced the depth reached by radiation from all lamps examined. The stratum corneum highly scatters and absorbs UVR, so thickening of this, by psoriatic scales, will greatly reduce the UVR reaching deeper layers of the skin. The results suggest that UVA1 radiation does indeed penetrate deeper than broadband UVA. However before UVA1 can be suggested as an effective treatment, it is necessary to investigate whether this UVA1 radiation will interact with cells treated with 8-MOP.

7.4.1 Absorption of UVR by psoralen

Whether the UVA1 lamp could be utilised to provide clinical benefit, beyond that achieved using standard broadband UVA photochemotherapy, depends on whether UVA1 is sufficiently absorbed by 8-MOP–DNA complexes.

To demonstrate the filtering effect of the upper layers of the skin, the results presented in Figure 7.7 have been normalised to the incident spectra. In these it is clear that the shape of the fluorescent UVA1 spectrum is mostly unchanged, whereas the broadband UVA spectrum is clearly shifted away from the shorter wavelengths.

7.4.2 Psoralen-DNA Complexes

Given the spectrum of radiation reaching the basal layer, in theory it should be possible to quantify the effectiveness of the photochemotherapy treatment as a whole, by including the effects of the photosensitiser at depth.

The absorption spectra of 8-MOP is shown in Figure 7.3. On initial examination, it seems evident that the longer UVA1 wavelengths reaching the basal layer (see Figures 7.6 and 7.7) do overlap with the 8-MOP absorption spectrum, given that 8-MOP absorption is non zero even into the visible range.

However it is not 8-MOP which causes the therapeutic effect, instead it is photoproducts associated with the dark complex of 8-MOP and DNA. It is known that both monoadducts and crosslinks contribute to the treatment of psoriasis [131]. 8-MOP-DNA complexes produce monoadducts when irradiated with visible light [131], so this alone allows a qualitatively conclusion that PUVA1 may be effective. However quantifying this proved difficult, as a comprehensive literature search did not uncover a wavelength resolved '8-MOP + DNA dark complex' spectrum for either monoadducts or crosslinks. However, the search did uncover a dataset for a similar molecule. A publicly available wavelength resolved spectrum of DNA-psoralen crosslinks does exist for another psoralen named HMT (4'-hydroxymethyl-4,5',8-trimethylpsoralen). Sastry et al. provided a detailed description of this molecule and performed the experiments from which the data presented in Figures 7.8 and 7.9 is taken [133].

The absorption spectrum of HMT is shown in Figure 7.8, trimmed to only show the region of interest from 280 nm. It is clear that, in the UVA1 region, HMT exhibits more absorption than 8-MOP, however 8-MOP absorption is non zero. From the work by Sastry et al. [133], data exist showing the actual relative yield of interstrand crosslinks produced using DNA + HMT complexes. These data are reproduced in Figure 7.9.

It is interesting to note, in reference to Figure 7.9, that the crosslink quantum yield does not follow the absorption spectrum of HMT. In fact, more cross links are found at the longer wavelengths than expected, and is noted by the authors [133]. Similarly, work by Gasparro et al. [131] also report a higher monoadduct yield than expected after irradiation of 8-MOP-DNA complexes by visible light.

Both authors report that this may be due to the fact that photoreversal of adducts is often induced by radiation of shorter wavelengths, and both theorise the higher than expected yields may be because the longer wavelength sources do not emit photons of high enough energy to induce photoreversal.

With this limited evidence, it is hard to quantitatively conclude the level of potential benefit

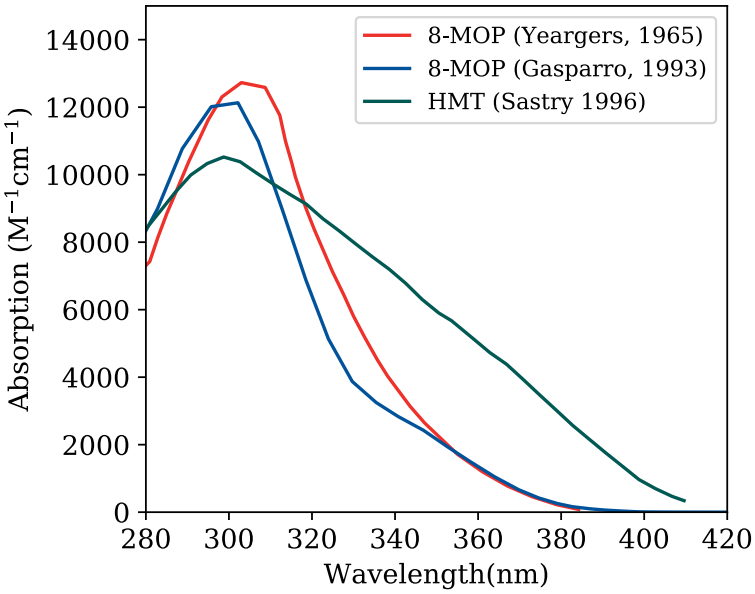

Figure 7.8: *Data from Figure 7.3 plotted alongside the absorption spectrum for HMT, reported by Sastry et al. [133]. The data range presented here has been clipped to the clinical UVB and UVA regions.*

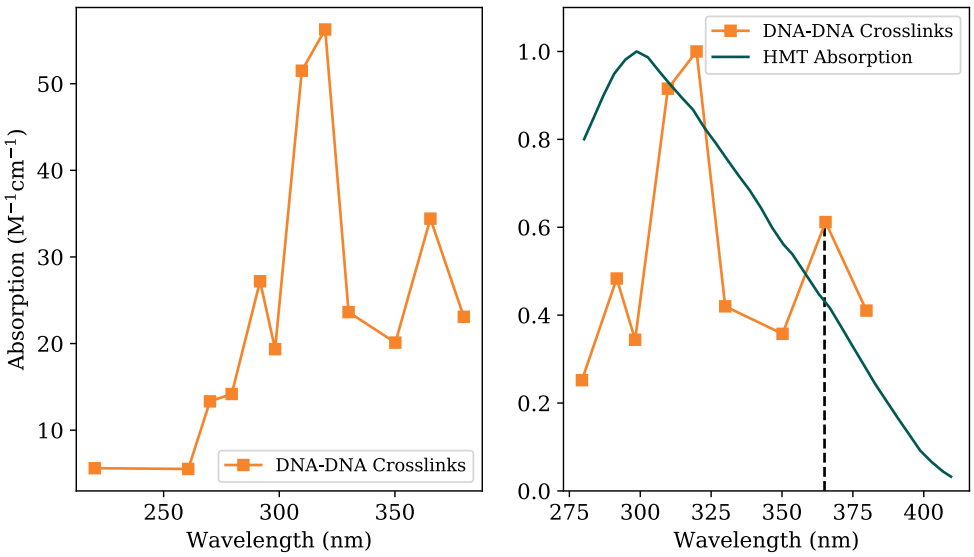

Figure 7.9: *The left panel shows the data from Sastry et al. [133], reporting DNA-DNA crosslink yield in DNA treated with HMT, and irradiated with 'monochromatic' UVR. The right panel combines this data with the absorption of HMT, and clearly shows that the quantum yield does not follow the absorption curve.*

UVA1 might afford over broadband UVA, but this evidence does suggest that the wavelengths reaching the deeper layers are capable of inducing the photoproducts required for therapeutic effect.

7.5 Conclusion

In conclusion, our results suggest that UVA1 radiation may be suitable for photochemotherapy treatment in cases where deeper depth penetration is required. The results clearly indicate that additional penetration depth is provided by UVA1 phototherapy radiation over that provided by the traditional PUVA source. It looks probable that this UVA1 radiation will interact therapeutically with 8-MOP treated skin cells, but whether this is to an extent to produce therapeutic effect remains unanswered. Based on the theoretical results presented here, clinical trials will begin in the future investigating the efficacy of PUVA1.

If a crosslink yield spectrum were available for 8-MOP, the methods described here would allow the calculation of a theoretical 8-MOP effective fluence. This would allow clinicians to predict a suitable starting exposure time for PUVA1 treatment.

The results presented here could be analysed further, using methods discussed in Chapter 4, to investigate relative CPD yields obtained during NB-UVB treatment and PUVA. This analysis could provide a theoretical explanation as to why studies report an increased cancer risk from PUVA treatment, but not in NB-UVB.

Chapter 8

Theoretical determination of the safety of far-UVC wavelengths used for disinfection

Synopsis

Ultraviolet C (UVC) radiation is known to be germicidal, and is used to sterilise equipment or rooms in hospitals or laboratories. UVC is known to be harmful to human health. However, the wavelengths involved in sterilisation were thought to be unable to penetrate skin tissue in sufficient amounts to cause erythema, and as such, some germicidal lamps were developed with the aim of being safe to use by humans without protection. Research carried out at the Photobiology Unit at Ninewells Hospital and Medical School, Dundee, found one such UVC sterilisation device caused erythema and CPD formation. It was hypothesised by the researchers that the erythema and CPD observed may be induced by small amounts of longer wavelength UVC also emitted by the device. Recently, development of novel UVC sterilisation device which filters out most wavelengths longer than 230 nm has led to questions about the safety of the novel device. Using MCRT, it appears that theoretically the majority of CPD (and so erythema) induced by the original UVC device tested was caused by small amounts of UVB and UVA present in the source spectrum.

8.1 Introduction

The current Covid-19 pandemic has highlighted a need for fast deployment of safe and effective sterilisation solutions. UVC radiation (200 nm to 280 nm) is effective for destruction of microorganisms, and is currently being investigated for effectiveness in destroying SARS-COV-2 [134], the virus responsible for the current Covid-19 pandemic. As a result being able to quickly sterilise rooms, surfaces, air, and people is of immediate interest. It is known that UVC radiation used for sterilisation can cause harm to skin and eyes [135, 136]. UVC sterilisation devices often use 254 nm radiation. These devices are unsafe for use on humans; causing adverse effects to the skin and eyes

after accidental exposure [137, 138].

Welch et al. [22] developed a UVC device capable of sterilising rooms. This device uses 224 nm UVC to kill airbourne viruses and bacteria, and uses a short pass optical filter to remove longer wavelength spectral components. As such, Welch et al. [22] have proposed the name far-UVC to describe this source. It is suggested that far-UVC would be both suitable for disinfection and safe for humans, as the UVC would not penetrate far enough into the epidermis to cause erythema or DNA damage.

However in 2014, Woods et al. [139] assessed the effect of a 222 nm UVC sterilising device (the Sterilray, Healthy Environment Solutions, Dover, NH). This study observed both erythema and direct CPD after exposures lower than the threshold for disinfection. Woods et al. [139] suggested that the small amount of longer wavelength UVR present in the devices's output may be responsible for the erythema and CPD observed.

The motivation for this work was to determine whether the erythema and CPD detected by Woods et al. [139] was caused by the far UVC radiation, or longer wavelength UVR also present in the source spectra (see Figure 8.1). If the observed erythema and DNA damage was due to longer wavelengths this may indicate that filtered far-UV sources (for example, Welch et al. [22]), may be safe for use on human skin.

8.2 Methods

For most of the simulations performed, the grid design and skin geometry is identical to that described in Chapter 5. However, in order to theoretically determine the transfer of far UVC radiation into the skin, optical properties covering the wavelength range of 200 nm to 280 nm were required. Previous to this research, all models investigated only the UVA and UVB wavebands, from 280 nm to 400 nm.

8.2.1 Irradiation source (the Sterilray)

To simulate the Sterilray device, each power packet has a wavelength randomly selected from the spectrum shown in Figure 8.1. It is assumed the output of the light guide is diffuse, so is modelled as diffuse illumination of the entire skin surface (using Equation 4.1 in Chapter 4).

8.2.2 Optical properties in the UVC

Scattering

The scattering coefficients used are shown in the left panel of Figure 8.2. For all of the scattering coefficients (stratum corneum, epidermal and dermal scattering), data is taken from van Gemert et al. [38] and extrapolated back to 200 nm.

Absorption

For the stratum corneum, epidermal and dermal scattering, data is taken directly from van Gemert et al. [38]. The published proprieties are modified to simulate Fitzpatrick skin type I using the method described in Chapter 4. Fitzpatrick skin type I was chosen, as this type skin will be the most

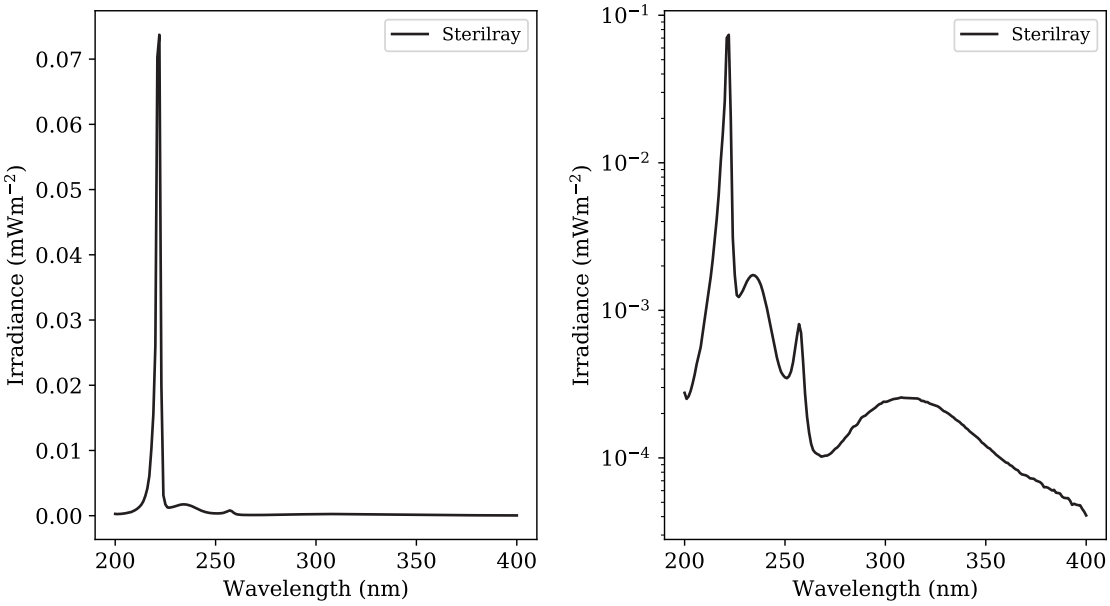

Figure 8.1: *Spectrum of the Sterilray device as tested by Woods et al. [139]. The left panel shows the spectrum on a linear plot, while the right on a log scale to highlight the non zero output of the Sterilray up to 400 nm.*

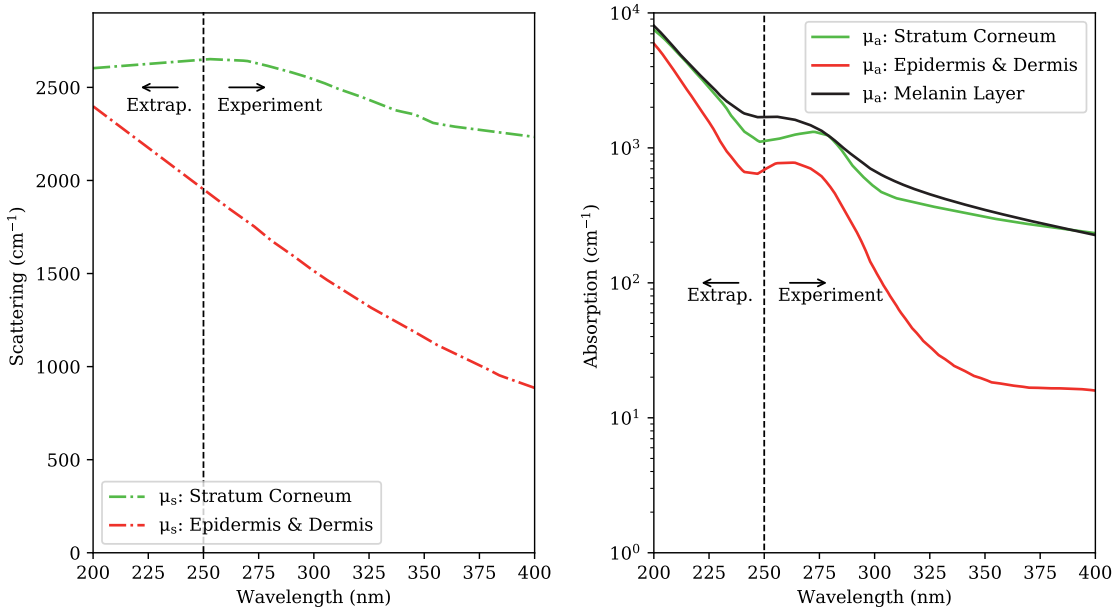

Figure 8.2: *Optical properties used in this model from 200 nm to 400 nm. The left shows scattering coefficients - these data are taken directly from van Gemert et al. [38] from 250 nm to 400 nm, and extrapolated back to 200 nm. The right panel shows absorption coefficients, these are taken directly from van Gemert et al. [38]. Both plots mark the regions of published experimental results, and published extrapolated results.*

vulnerable to DNA damage by UVR. Typically in the UV region of the electromagnetic spectrum, scattering in tissue dominates over absorption. However from the available optical properties, in the UVC region, absorption is expected to dominate in the upper layers of skin. This is in line with the reason for theorised efficacy of far-UVC, as reference [140] states that at around 200 nm, UVC is strongly absorbed by proteins (due to the high UVR absorption by peptide bonds, which are covalent bonds linking two amino acids [141]).

Other properties

In the absence of detailed properties for the UVC, the other optical properties (refractive index n and the anisotropy factor g) are assumed to take the same form as outlined in Chapter 3.

8.2.3 Data analysis

Given the high absorbance and scattering in skin in the UVC, to allow for detection of any UVC power packets on the basal layer, 10^9 power packets were simulated.

The fluence is extracted from the grid cells, using a adaptation of Equation 4.3 where, in addition to selecting the cells from the basal layer, cells are also selected from the upper epidermis (at a depth of 20 μm) and the middle epidermis (at a depth of 40 μm).

In order to extract the depth at which radiation has dropped to 50% of the incident, the depth dependent fluence is extracted using the path length counters and summed,

$$\psi_z = \sum_{\lambda} \sum_{i=1}^{50} \sum_{j=1}^{50} \psi_{i,j,k}(\lambda) \tag{8.1}$$

The result is interpolated to find the z value where

$$\frac{\psi_z(\lambda)}{\psi_0(\lambda)} = 0.5 \tag{8.2}$$

In order to extract the half value depths for 222 nm, another simulation was run, this time with a vertical voxel depth resolution of 0.1 μm.

CPD

To determine the wavelength dependent probability of producing CPD, the fluence obtained for each layer is combined with a direct CPD yield spectrum obtained from Matsunaga et al. [142] (presented in Figure 8.3). This CPD yield spectrum is obtained from naked DNA (calf thymus). This spectrum is used over Ikehata et al. [83], as results are reported from 150 nm to 365 nm (spanning most wavelengths emitted by the Sterilray). These results have been normalised to 1 at 260 nm, and as a result, no absolute CPD yields can be obtained via the method described here. In addition, the concentration of DNA in each skin layer is taken into account (using the methods from Chapter 4 to estimate DNA concentrations in the skin layers, DNA concentrations are estimated to be 0.018 M for the basal layer and 0.005 M for the upper and middle epidermis).

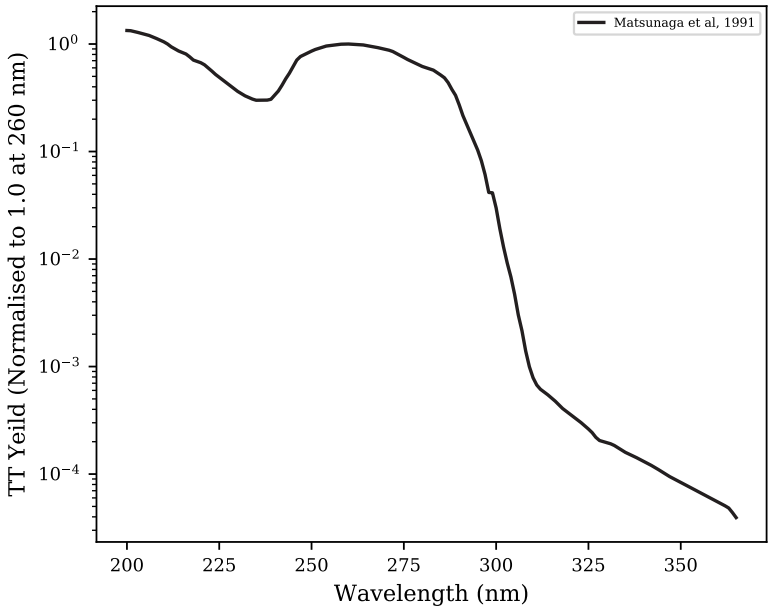

Figure 8.3: *Wavelength dependent CPD yield in naked DNA, relative to yield at 260 nm, from Matsunaga et al. [142]. This is combined with the fluence spectra obtained for each layer and used to predict the CPD yield in each layer.*

8.3 Results

The resulting fluence extracted from each layer under investigation is plotted in Figure 8.4. The half value depths of radiation at different wavelengths are presented in Table 8.1.

Wavelength	Depth
222 nm	1.65 μm
254 nm	4.5 μm
300 nm	10.5 μm

Table 8.1: *Depths at which radiation incident on the surface of the skin drops to 50% of the incident.*

8.3.1 CPD yields

In order to identify the the wavelength dependent probability of producing CPD in each layer (Figure 8.3), the results presented in Figure 8.4 are combined with the wavelength dependent probability of producing CPD (Figure 8.3).

In addition, Table 8.2 shows the percentage of total CPD produced in each layer attributed to 'far UVC' (200 nm to 230 nm), the remaining UVC (230 nm to 280 nm), and the component in the UVB & UVA (280 nm to 365 nm).

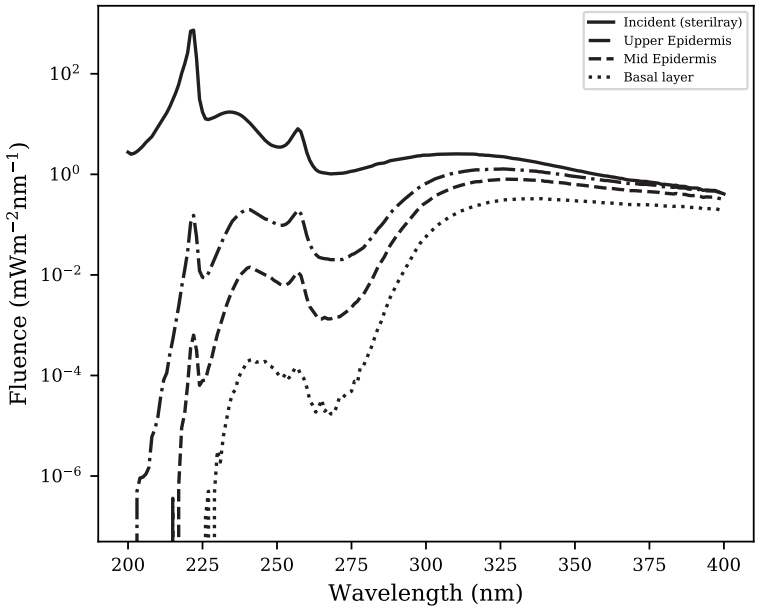

Figure 8.4: *Irradiance of the Sterilray spectrum, and MCRT simulated fluence recovered from the upper epidermis (20 µm), the middle epidermis (40 µm), and the basal layer (avg. 80 µm).*

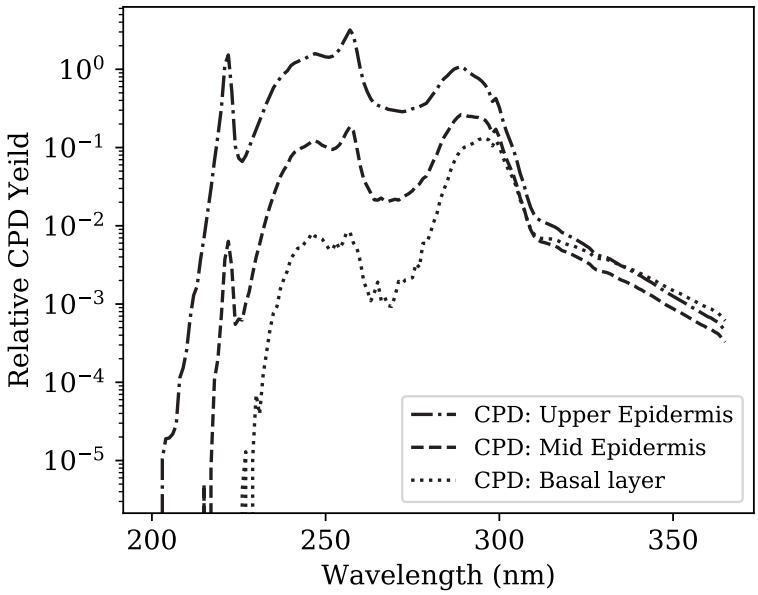

Figure 8.5: *Spectral probability of producing CPD in each layer relative to the probability of producing CPD in the upper layer of the epidermis at 260 nm. The fluence spectra shown in Figure 8.4 are combined with the wavelength dependent CPD yield shown in Figure 8.3 from Matsunaga et al. [142] and the theoretical DNA concentrations from the skin layers to produce this plot.*

Layer	Percentage of total CPD		
	200 nm to 230 nm	230 nm to 280 nm	280 nm to 365 nm
Upper epidermis (20 μm)	6.40%	69.75%	23.85%
Middle epidermis (40 μm)	0.28%	41.41%	58.31%
Basal Layer (approx. 80 μm)	0.00%	7.44%	92.56%

Table 8.2: *CPD produced by different bands of UVC (200 nm to 230 nm, and 230 nm to 280 nm) and the remaining UVR (UVA and UVB, from 280 nm to 365 nm), as a percentage of total CPD induced within that layer*

8.4 Discussion

Figure 8.4 shows that while some radiation from the 222 nm peak of the incident spectrum reached the upper and middle epidermis, none reaches the basal layer.

With reference to the incident spectra shown in Figure 8.1, only 16% of the lamp output power is emitted at wavelengths longer than 230 nm, and only 6% is emitted at wavelengths longer than 280 nm. Given this, it is important to note the lower intensity incident radiation above 275 nm makes up the majority of the radiation penetrating even to the upper epidermis.

Given that the average depth of the stratum corneum is 14.8 μm (and ranges from 10 μm to 40 μm) results from Table 8.1 and Figure 8.4 indicate that 222 nm radiation alone is unlikely to penetrate the stratum corneum in sufficient quantities to cause harmful effects. As MCRT fluence includes any back scattering effects, this can lead to a higher fluence just under the skin (due to fluence being integrated over all angles, whereas irradiance is just incident on the skin). It is not clear whether the half value depths reported in reference [140] (of 0.3 μm for 200 nm radiation and 3 μm for 250 nm) include back scatter, but if not, this would explain the slightly deeper half value depth reported for 254 nm in Table 8.1.

Figure 8.5 shows that while CPD from shorter wavelengths are expected to be found in the upper and middle epidermis, no far UVC wavelengths induce CPD in the basal layer (where CPD may have mutagenic potential).

Figure 8.5 and the results presented in Table 8.2 strongly indicate that the majority of CPD in the basal layer are not produced by far UVC (< 230 nm), and in fact the basal layer is strongly shielded from UVC wavelengths. This indicates that the CPD found in the basal layer by Woods et al. [139] are likely to have been induced by the longer wavelength UVC, and possibly UVB and UVA present in the Sterilray (which are only visible in Figure 8.1 on the log scale).

However it is not possible to conclude that that the erythema observed by Woods et al. [139] was most likely to have been induced by the longer wavelength UVB and UVA present in the Sterilray. A large proportion of the CPD in the upper and middle layers (where direct CPD are a likely a marker for erythema [5]) are induced by UVC present in the device, and as shown in Table 8.2, over 5 % of CPD in the upper layer of the epidermis (and so 5 % of the radiation inducing the erythemal response) is likely to be from the 200 nm to 230 nm band.

Research by Buonanno et al. [140, 143, 144] has found that no epidermal CPD are detectable in mouse skin under irradiation with 207 nm and 222 nm UVC, while epidermal CPD are detectable when irradiated with 254 nm UVC. The results are the same when compared to a 3D human skin model [143]. These results are in contrast to the theoretical findings presented here, where some

CPD formation would be expected in the upper living epidermis for 222 nm. However all results presented here are relative, and it may be that the very low levels of CPD predicted here would not be detected, or even form *in vivo*. Such findings highlight the need for independent clinical trials in humans.

This thesis is restricted to simulating UVR transmission through human skin. However, the methods described within this thesis could be used to build an MCRT model capable of simulating the transmission of UVC radiation through eye tissue. As it is known that germicidal UVC lamps can damage eyes [136, 137, 138], such a model could offer a useful *in silico* method to aid prediction of any harm to human eyes caused by UVC devices.

8.5 Conclusion

Overall the results do indicate that with sufficient filtering of radiation above 230 nm, a UVC sterilisation device may be safe for use on human skin. The simulations indicate that it is very unlikely that far UVC devices will cause long term harm, in the form of carcinogenic mutations in the basal layer. However the same conclusion cannot yet be made for erythema. However as CPD in the upper and mid layers of the epidermis are the cause of erythema [5], then the result presented conclude that most, but not all, erythema observed by Woods et al. are due to wavelengths longer than 230 nm. In addition, UVC has been shown to degrade the structural and mechanical properties of the stratum corneum [145], where after irradiation with UVC, fractures were more likely to occur. This indicates that regardless of CPD or erythema, studies on the long term impact of UVC irradiation on human skin are required.

As such, independent clinical trials in humans of any new devices are necessary to confirm *in vitro* and *in vivo* conclusions that wavelengths shorter than 230 nm are indeed safe for use around humans, and if so, to test safe dosage limits.

Chapter 9

Highland Sunbeds

9.1 Synopsis

In 2012 it was reported that most sunbeds in England emit UVR at levels above the recommended European safety standard [54, 146]. Highland Council have a sunbed licensing scheme, and the licence conditions include compliance to the European safety standard. In order to measure the UVR output of sunbeds, Highland Council purchased a handheld UVR meter, and requested assistance from the Photobiology Unit at Ninewells Hospital and Medical School, Dundee, in assessing the suitability of a handheld UVR meter to evaluate UVR output of commercial sunbeds. Here, the calibration method and performance of the UVR meter in comparison to methods used in previously published work is reported.

9.2 Introduction

It is known that 9/10 sunbeds in England emit UVR levels that exceed the European safety limits [54]. These state that the total erythemally effective output of a sunbed must be below 0.3 Wm^{-2}, with this comprising of no more than 0.15 Wm^{-2} contribution from UVA and no more than 0.15 Wm^{-2} from UVB [146].

9.2.1 Sunbed Licensing at Highland Council

Councils in Scotland have the option of licensing sunbed premises, however only a handful have chosen to do so. One such council is Highland Council. Licensing of sunbed premises provides revenue to the council, and in theory it should provide the customer with confidence that the sunbed premises they are using is operating within guidelines set out within the licence.

The licences are granted by Highland Council Environmental Health (HCEH), based in Fort William. Licence conditions include placement of Scottish government mandated warning posters, air conditioning and temperature regulation, a ban on access by children and young people, a separate room housing the sunbed to avoid accidental exposure to UVR, and that the total UVR output from the sunbed must comply with the European Safety standard [146, 147]. HCEH had no

way to independently verify that the sunbed complied with the standard, and this condition was satisfied via the output listed for the sunbed make and model, and also via sunbed servicing reports.

An incident reported to HCEH attributed a burn to sunbed use. The environmental health team sought a method of determining the UVR output of a sunbed to determine, independently of sunbed operators, whether the sunbed met the safety standard [146]. HCEH purchased the Gigahertz Optic X1-4 light meter, which is an 'UV Erythema Broadband Radiometer for Hazard Testing Sun Tanning Beds'[148]. After purchasing the unit, HCEH made contact with the Photobiology Unit at Ninewells Hospital and Medical School, Dundee, for assistance in assessing the suitability of the light meter for measuring the UVR output of sunbeds.

9.2.2 UVR measurement and spectroradiometry

Measuring the dose of UVR from any lamp source is difficult. It is not enough to simply measure the total power output of the source. The European safety limits are placed on the the erythemally effective radiation (Equation 1.1), not the power output from the sunbed. As described in Equation 1.1, erythemal effectiveness is wavelength dependent. To calculate the effective erythemal dose, the output power of the sunbed must be spectrally resolved somehow.

Spectroradiometry is a technique that allows the spectrum from the light to be measured. Spectroradiometry can be performed using a benchtop device, or a portable diode array detector. A common problem with UV spectroradiometry is light that falls on, and is counted by, an incorrect pixel within the detector. This is known as stray light [57].

Stray light can be minimised using a double slit spectroradiometer, an example of which is the double-grating Bentham spectroradiometer (IDR300, Bentham Instruments Ltd, Reading, UK). The Bentham spectroradiometer (the Bentham) is calibrated against the National Physical Laboratory, and accredited for clinical calibration purposes by the UK Accreditation Service. The Bentham is fixed in place within a climate controlled room, so sources must be brought to the laboratory for testing. This means it would be extremely difficult to use the Bentham for on-site sunbed measurements.

Portable diode array detectors can be used to measure the UVR output of sources *in situ* (such as sunbeds) [54, 57]. However, as these use a single slit, stray light must be accounted for. Although stray light is minimised during the design process, at small irradiance levels, stray light could potentially be the cause of a high proportion of counts measured at a given wavelength (especially in the UVB). Corrections for stray light are determined by calibrating the portable diode array against the Bentham.

Both use of the Bentham and portable diode array detectors require a skilled operator, expensive equipment, and data processing.

Another method for measuring UVR is a hand held unit giving a single reading, such as the X1-4. Such a unit is likely to also suffer from stray light problems internally, however this can be accounted for by using a reference source spectrum. Use of the incorrect reference spectrum can lead to incorrect readings from the handheld meter.

9.3 Methods

9.3.1 Calibration of X1-4

The X1-4 light meter is a lightweight, handheld meter that is designed for 'Measurement and examination of UV Hazard from UV Irradiation devices like sun-tanning beds'. It is operational between 5°C and 40°C (this is important as during on-site sunbeds measurements the room containing the sunbed can become very warm).

The detector head comprises of 3 sensors. One measures erythemally effective UVA, one measures erythemally effective UVB and UVC, and one measures UVC output.

The X1-4 lightmeter was brought to the Photobiology laboratory and calibrated in line with the UKAS standard provided by the Photobiology department, Dundee. This was achieved by taking identical measurements of a selection of UVR sources with the Bentham and the X1-4, and comparing the results.

In the climate controlled photobiology laboratory, the Bentham is switched on and left to reach operation temperature. The X1-4 collection detector head was positioned to be exactly in line vertically with the Bentham collector head, and firmly fixed in place. A vertical bank of calibration lights was set up at a distance of 30 cm from the detector heads. They were switched on and left for 5 minutes to warm up. As the bank of lights was vertical we assume the small vertical offset between the Bentham and the X1-4 does not affect the radiation collected. The X1-4 detector head is covered, and a dark reading taken. Then the head is uncovered, and an erythemally effective reading for both UVA and UVB is taken. Then the Bentham spectrum acquisition begins, which takes about 10 minutes. After this, another X1-4 reading is taken, and then the head is covered, and another dark reading is taken. The reading for the X1-4 is taken as the average of the two readings (minus the dark reading, which for the X1-4 was zero for both UVA and UVB). This process was repeated for several types of lamps used in the photobiology department. The spectra acquired from the Bentham are processed to find the erythemally effective UVA and UVB output, and the results compared to those recorded for the X1-4.

The total erythemally effective UVA and UVB compared between the results from the Bentham and the light meter results. It was found that the X1-4 required a 0.98 correction factor for total erythemally effective UVR.

It should be noted that on initial examination, the X1-4 was found to be faulty (the device showed a zero reading for UVB, no matter the lamps used). The device was returned to Gigahertz Optic for repair, and all reports here are on the repaired device.

9.3.2 Portable diode array

Although the Ocean Optics device does exhibit stray light errors in measurement, data processing techniques have been developed to account for these. This device has been used to gather data published data in the field [54, 57].

In the field, the performance of the X1-4 was compared to that of a portable diode array spectrometer (the Maya 2000 Pro Ocean Optics Spectrometer, Ocean Optics, Dunedin, FL, U.S.A.). The Ocean Optics device has been used for similar research previously [54]. The Ocean Optics device was also calibrated against the Bentham at the Photobiology laboratory in an almost identical

way to that described above for the X1-4, with the only difference being that each single spectrum recorded by the Ocean Optics comprises data from two readings, one 'long' acquisition and one 'short' acquisition. The long acquisition saturates in the UVA (the bulk, and peak, of sunbed output) but accurately captures the UVB. The 'short' reading will accurately capture the UVA without saturation, but will not gather many counts for the UVB. The results were analysed to produce a wavelength dependent calibration factor for the Ocean Optics device.

On site measurements

In order to assess the performance of the X1-4, the X1-4 was compared in on-site experiments to a portable diode array detector- the Ocean Optics USB 2000 pro.

Inspections took place taken at 5 locations in Fort William, and 6 locations in Inverness and Aviemore.

Measurements in the sunbed cabins were taken using the method described in reference [54]. In summary, the sunbed was switched on, and after 2 minutes of warm up, identical measurements using the X1-4 and the Ocean Optics spectrometer are taken at positions as that mimic the position of a human body within the cabin. Identical measurements were taken using both the X1-4 and the Ocean Optics USB spectrometer. The results from the X1-4 were recorded on sheets prepared by HCHS, and the spectra obtained from the Ocean Optics device were analysed using calibration data from the Bentham (and Equation 1.1), and then integrated across bands to find the erythemally effective UVA, UVB and total UVR doses. For each sunbed, the resulting erythemally effective output is the average of all of the measurements taken within the sunbed cabin. The results were analysed and compared to determine the suitability of the X1-4 for such on-site use.

9.4 Results

Figure 9.1 presents the erythemally effective UVR irradiance recorded by the X1-4 and those calculated by analysing the spectra obtained by the ocean optics device. Figure 9.2 presents the results divided into UVA and UVB components. On both Figure 9.1 and 9.2, the EU limit and the average reported by Tierney et al. [54] are marked.

9.5 Discussion

The results in Figure 9.1 indicate that the X1-4 reads over what is found via the Ocean Optics device by a factor of about 14%. The X1-4 consistently gives a higher reading than the Ocean Optics, indicating a source of systemic error. However with reference to Figure 9.2, the readings from the X1-4 and the Ocean Optics for UVA are remarkably close, and the difference in UVR as a whole appears to be due to differences in the UVB readings.

One possible source of error is the source spectrum library. To accurately characterise erythemally effective UVR, the X1-4 needs a reference spectrum (which is selected before use via the device interface). Given that this relies on choosing the generic 'tanning sunbed' option on the X1-4, this will lead to errors as all the lamps tested in the sunbeds have slightly different spectra. However,

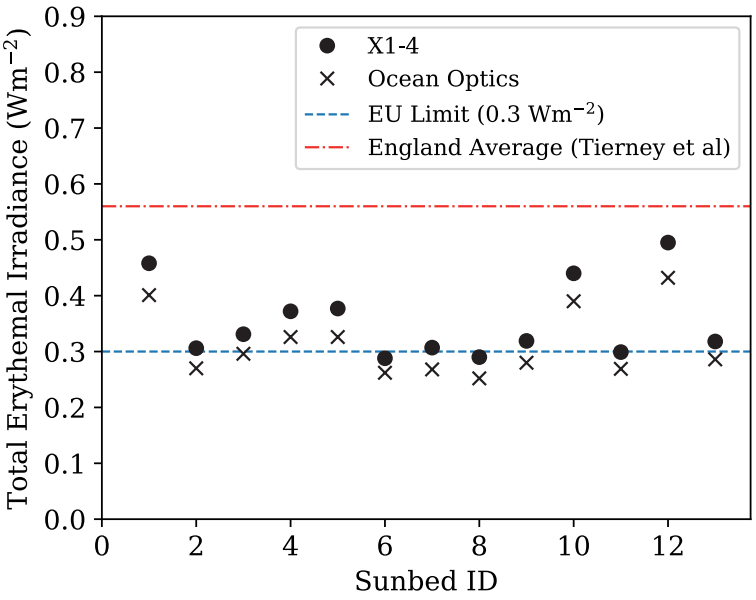

Figure 9.1: *Measured total erythemally effective UVR from each sunbed, using the X1-4 and the Ocean Optics portable diode spectroradiometer. Also shown via dashed lines are the EU limit, and the average experimentally measured by the survey of sunbeds in England undertaken by Tierney et al. [54].*

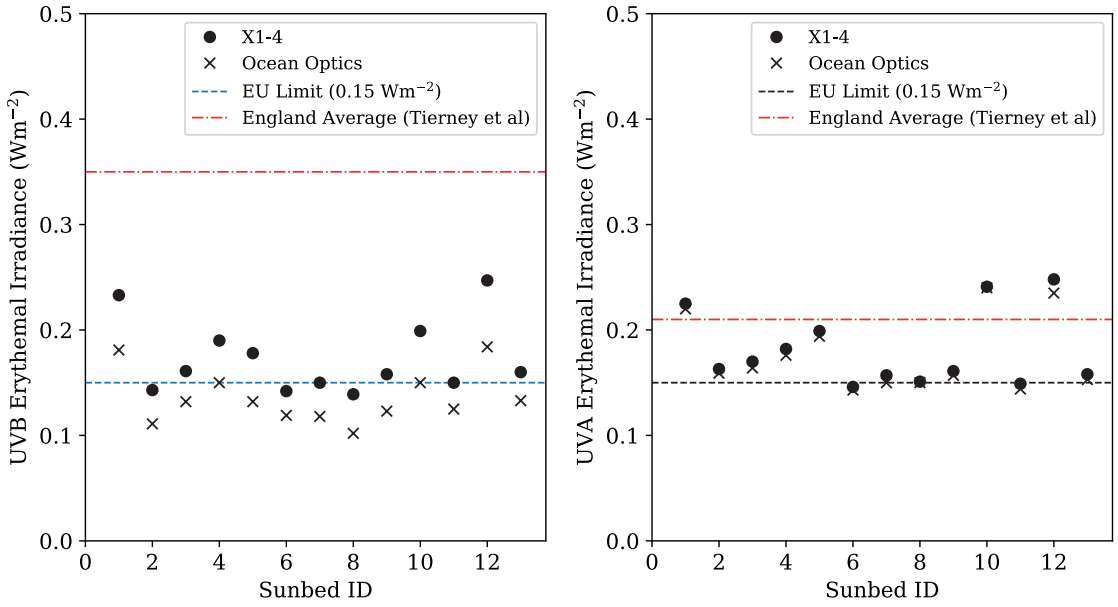

Figure 9.2: *Measured erythemally effective UVA and UVB from each sunbed. Also shown via dashed lines are the EU limit, and the average experimentally measured by the survey of sunbeds in England undertaken by Tierney et al. [54].*

given measurement difficulties with UVR, the calibrated X1-4 is likely to be a suitable tool for this sort of measurement.

All sunbeds surveyed here had total erythemal irradiance below the average reported by Tierney et al. [54] in 2012; regardless of the measurement device used. The UVB readings reported here are much lower than those reported in reference [54], however, the UVA readings are closer to the average reported in reference [54]. Without taking further measurements outside the Highland Council area it is impossible to say whether this is an effect of the licensing scheme, or if sunbeds are more generally now closer to compliance with the standard.

In taking measurements with the Ocean Optics, the acquisition and analysis process required a skilled operator. The time taken to acquire Ocean Optics readings were orders of magnitude longer than for the X1-4, all taking place in a hot, bright environment around UVR. Acquisition times for the Ocean Optics (taking 6 readings per sunbed) thus require the operator to be in the same room as the sunbed for up to 15 minutes. In contrast, the X1-4 is much easier to use, as there is no significant acquisition time (readings are taken as soon as the reading stabilises; which was within seconds) and taking the 6 readings at different positions within the sunbed cabin took less than 2 minutes. However no matter the device used, proper personal protective equipment must be worn (including high SPF sunscreen reapplied before each visit, goggles, a face shield, and long sleeved clothing, and gloves).

9.5.1 Sunbed Premises

All premises visited were hotel or gym chains, or independent beauty salons (no tanning salon chains). During visits to the hotels and gyms, there was no discussion with managers about the sunbed, or the licensing process. However, the independent salon owners were keen to discuss sunbed use, sunbed maintenance, the biological effects of UVR, and expressed concern about customer's safety.

For example, most sunbed premises use a token system to ensure the sunbed is only switched on for short periods of time. Several operators said they are aware that some customers 'bank' tokens, in order to circumvent the time-limited sunbed operation period. It is impossible to say without further research how long the average customer actually spends on a sunbed. Such research may be of value in order to compare the risks of long term harm due to to recommended use to the risks of actual customer behaviour.

One salon was found to have a sunbed with a particularly high erythemally effective UVB reading. The owner said that bed was particularly popular with psoriasis sufferers, and she offered them priority. The extent of such 'self medication' of this type within the UK is unknown (though it has been investigated in the US [149]). Investigating this, and potential impacts, may be of use to phototherapy providers. Many salon owners asked questions about the dangers of UVR, specifically about photoageing and risks of skin cancers. After this, several salon owners volunteered the information that sunbed engineers give advice on increasing the output of their bed beyond the rated performance, and advice on preparing for an enforcement visit (such as retaining broken starters for the sunbed lamps, and swapping these into the place of working starters when the enforcement visit occurs). This lead to the question as to how the sunbed engineers actually measured the output of the sunbeds (which was part of their safety checks), and investigating this further may be of interest from a public health perspective.

9.6 Conclusion

In summary, given good agreement with results obtained via the established protocol, the X1-4 is likely to be suitable as a device to measure the UVR output of a sunbed. Given the speed at which measurements can be taken, the X1-4 is likely to be a safer device for the operator to use than a spectroradiometer, as less time is required to take the measurements; so there is less preventable UVR exposure.

For the X1-4 to be used by a Health & Safety officer (without specific radiation safety background) to measure sunbed UVR output, training would be required in non ionising radiation safety. In addition, it would be difficult to state whether readings from the X1-4 could be considered an accurate enough measurement method for legal enforcement action, if this was required. The X1-4 would require regular calibration tests with a qualified standards laboratory, such as the Photobiology Unit. The performance of the X1-4 could potentially be improved by identifying the ideal reference spectrum for a given sunbed, and this could only be achieved by developing some sort of reference library of commonly used sunbed lamps within sunbed units.

Chapter 10

Conclusion

10.1 Summary

The aim of this project was to develop a MCRT model capable of simulating the transport of ultraviolet radiation (UVR) through the upper layers of human skin, in order to quantify biological affects caused by UVR penetrating into skin.

Chapter 1 provided an introduction to the structure of human skin, and the biological consequences of exposure to UVR radiation. The chapter goes on to derive the equation of radiative transfer, and makes the case for Monte Carlo radiation transfer MCRT as a suitable method to solve radiation transfer through turbid media.

Chapter 2 detailed the coding implementation of MCRT as used throughout this thesis, including random sampling, interactions (scattering and absorption), the 3D voxellised grid, and the use of path length counters to estimate physical quantities. Chapter 2 also provides the validation technique used throughout this work to ensure the MCRT code provided expected results for known input parameters.

Chapter 3 described in full the MCRT model used throughout this thesis, including geometry and optical properties used to simulate the upper layers of the skin. This chapter also details how different irradiation sources are simulated, and in general details the approach taken to setting up an MCRT simulation of UVR transport through skin.

Chapter 4 detailed implementation of the code to quantify direct DNA within the basal layer of skin (in skin types I & II). Here, the results indicated that about 6 minutes on a sunbed would cause the same amount of damage as 10 minutes in Mediterranean sun, and that the majority of CPD found in the basal layer of sunbed irradiated skin are caused by the UVA component of sunbed irradiation. The development and implementation of this model was the precursor to most of the subsequent work presented in this thesis.

Chapter 5 extended the work within Chapter 4 to cover darker skin types. This was achieved by using published experimental work as a basis around which to design simulations. In doing this, the code written for the previous chapter was altered, and more abstractions included, to make future changes easier to implement within the existing code. In this chapter, experimentally determined layer dependent melanin concentrations were applied in the code, along with experimental irradiation sources. The results found from simulation were mostly within the 95% confidence interval reported

by experiment (with only the upper epidermal results lying just outside). Simulations were repeated using solar, instead of solar simulated, radiation, and this predicts that solar simulators slightly overestimate the protection afforded by melanin when compared to solar irradiation.

Chapter 6 extended the code as described in Chapter 3 by adding a layer of sunscreen to the surface of the skin, and investigating the resulting reduction on CPD yield in the basal layer. The chapter begins by reproducing the results of existing online sunscreen simulators using a very basic Monte Carlo transmission code. Then, this is applied to a voxellised grid, which is eventually added to the surface of the skin model. Then, as in Chapter 5, experimental work was used as a basis to design simulations.

Chapter 7 described how the MCRT code was implemented to determine whether UVA1 radiation could be used in conjunction with psoralen in the treatment of palmoplantar pustular psoriasis. The results indicated that this combination may have potential to work, and a clinical trial is planned.

Chapter 8 investigated a UVC sterilisation device to determine whether experimentally reported CPD yield were likely due to the shorter, UVC wavelengths, or longer UVC/UVB wavelengths also present in the device. The chapter concluded that it was likely CPD in the basal layer were induced by longer wavelengths (so a device that filters these was likely to be safe). However the theoretical study reported here could not conclude which wavebands induced the reported erythema.

Chapter 9 presents results from practical work, where the performance of a handheld UVR meter was assessed for suitability to measure UVR output of commercial sunbeds in operational locations (such as beauty salons and gyms). The conclusion is that it is likely the device would be of use if suitable training was given to the operator.

10.2 Concluding remarks

One issue with computational models such as the ones presented here, is that even if the physics of the system is well represented by the model used, the output of the simulations are completely dependent on the parameters input to the model (so called 'nonsense in, nonsense out'). As such, in order to assess the quality of results, validation against experimental results is a useful and important step, where possible.

Within this thesis, this was achieved by designing simulations to match experimental protocols, and comparing results. However, while simulations that reproduce experimental results offer an important validation step, they do not advance research in photobiology. One advantage of simulations is the ability to go beyond what can easily be achieved experimentally. This is why working closely with clinicians and scientists within the Photobiology Unit at Ninewells Hospital and Medical School, Dundee, was invaluable, as this provided the insight into exactly what required further investigation.

In order to produce an MCRT model of UV radiation transfer through skin, the key parameters input to the model are the optical properties for the skin layers, and the geometry of these skin layers. There is good data available for skin layer geometry, covering many different skin sites and skin types. However, the availability of optical properties for skin in the UV is poor. Several of the optical properties used throughout this model (e.g. for the stratum corneum, and the epidermis) were taken from results published in the 1960's to the 1980's. Results throughout the thesis for the UVA point consistently indicate that the model overestimates the amount of longer wavelength

UVA radiation penetrating into the skin, which indicates that either, or both, of the scattering and absorption properties used were underestimated. Some of the UVC optical properties used in Chapter 8 were taken from published, but extrapolated data. Comprehensive literature reviews yielded few more recent optical properties to use. Some exist, but often these would include only one or two datapoints in the UVR (e.g. the refractive index in Equation 3.1 [48]).

It would be beneficial to the field to complete a literature review of UV optical properties for use in MCRT (or other mathematical modelling approaches), either limited to human skin, or to tissue in general. A comprehensive literature review would highlight where data is lacking, and may suggest which up to date techniques could be applied to obtain useful data. This would lead to better wavelength resolution for the optical properties, and hopefully lead to more effective MCRT models.

Ideally, the optical properties for an individual patient could be obtained, and entered into the simulation in order to predict UVR dose required for a given treatment from a given lamp, leading to truly personalised *in silico* predictions.

10.3 Future Work

The MCRT code developed for this project is now reasonably robust. At the beginning of this work, it took well over a year to get code that could simulate DNA damage in human skin. With each subsequent application, the code was improved, speed was increased, and bugs detected and removed. The simulation work for one of the later chapters (UVC) was completed in under three weeks, including research into optical properties in the UVC. This code is now developed well enough to be close to being something more of a tool than a research project in itself. It could be used by photobiological researchers to investigate specific situations. For example, the model developed here could be used to provide theoretical explanations for example as to why NB-UVB does not seem to cause cancer. Another example would be investigating phototherapy across different skin types, and body sites (e.g. PUVA on darker psoriatic skin), potentially aiding dermatologists.

Another application of this code could be to work in parallel, rather than apart, from *in vivo* researchers, with the aim of reducing animal testing in the future. One potential downside to *in silico* investigations such as these, may be that previously unknown phenomena would be effectively impossible to investigate or observe as they would in an *in vivo* study. By working alongside *in vivo* experiments, the *in silico* results could be directly compared and suitability as a replacement assessed. For example, murine skin is widely used in photobiological research. Lab mouse breeds are likely to have much more homogeneous optical properties of the tissue across individuals than humans. As such, an MCRT model of mouse skin could be built, and improved upon as more data were obtained. This may provide a route to validate the *in silico* model, and reduce animal testing in the future.

Another, future direction of the work presented here could be *in silico* phototoxicity prediction. The foundations of this can be found in Chapter 7, which investigates how UVR from different phototherapy lamps interacts with psoralen. One point made in the discussion is that absorption does not equate to photobiological action. It is not necessarily tissue or compounds that interact with UVR, but rather tissue-compound complexes. If this work could be reproduced for other drugs or compounds currently under *in vivo* investigation (human or animal), then the extent to which

this code can predict phototoxicity could be assessed. This may be a route to achieving a small reduction in testing on animals or humans within biological and pharmaceutical research.

Other future applications include extending the model to try to predict the most beneficial phototherapy treatment for a patient, given the site of their disease. This potential application of *in silico* personalised medicine could be achieved quickly, and may lead to improved patient outcomes.

Another application of the model could be to investigate phototherapy induced damage in blood cells. In fact, the model can, as it stands, predict the DNA damage from any supplied UVR source to any cell in the epidermis, basal layer, and upper dermis.

A barrier to this work being used as a tool, as is, is that the code is written in Fortran 90, a language that few researchers (outside the specialities astrophysics, meteorology, or other high performance computing applications) are familiar with. However, this could be overcome easily by providing a graphical user interface, or even an easy to use command line interface. To simplify the user experience further, cloud computing capabilities could be utilised. MCRT is an ideal application for cloud computing approach; as costs could communicated to the end user up front, and the actual MCRT code would be maintained and executed on the cloud, removing the need for the end user to have a computer dedicated to these simulations.

10.4 Conclusion

Starting from code originally developed for Astronomy research [36], an MCRT model capable of simulating UVR transmission through the upper layers of skin tissue has been developed. This code is publicly available in the repository at `https://doi.org/10.5281/zenodo.5651209`. This model has been adapted for several different applications as outlined in this thesis, including simulating DNA damage in different skin types, photoprotection by sunscreens, efficacy of phototherapy treatments, and safety implications around the use of UVC lamps. At the opening of this thesis, the statistician George Box was quoted; "*All models are wrong, but some are useful*", and this thesis aims to place the model presented within in the latter category.

Bibliography

[1] D.L. Narayanan, R.N. Saladi, and J.L. Fox. Ultraviolet radiation and skin cancer. *International Journal of Dermatology*, 49:9778–986, 2010.

[2] U. Leiter and C. Garbe. Epidemiology of Melanoma and Nonmelanoma Skin Cancer—The Role of Sunlight. In *Sunlight, Vitamin D and Skin Cancer*, pages 89–103. Springer New York, New York, NY, 2008.

[3] H.S. Black, F.R. deGruijl, P.D. Forbes, J.E. Cleaver, H.N. Ananthaswamy, E.C. deFabo, S.E. Ullrich, and R.M. Tyrrell. Photocarcinogenesis: an overview. *Journal of Photochemistry and Photobiology B: Biology*, 40(1):29–47, 8 1997.

[4] Cancer Research UK. Non-melanoma skin cancer statistics https://www.cancerresearchuk.org (accessed February 2020).

[5] A.R. Young, G.I. Harrison, C.A. Chadwick, O. Nikaido, J. Ramsden, and C.S. Potten. The Similarity of Action Spectra for Thymine Dimers in Human Epidermis and Erythema Suggests that DNA is the Chromophore for Erythema. *Journal of Investigative Dermatology*, 111(6):982–988, 12 1998.

[6] Kenneth Wood and RJ Reynolds. A model for the scattered light contribution and polarization of the diffuse hα galactic background. *The Astrophysical Journal*, 525(2):799, 1999.

[7] C.L. Campbell, C. Christison, C.T.A. Brown, K. Wood, R.M. Valentine, and H. Moseley. 3D Monte Carlo radiation transfer modelling of photodynamic therapy. volume 9531, page 1H. International Society for Optics and Photonics, 6 2015.

[8] C.L. Campbell, K. Wood, R.M. Valentine, C.T.A. Brown, and H. Moseley. Monte Carlo modelling of daylight activated photodynamic therapy. *Physics in Medicine and Biology*, 60(10):4059–4073, 5 2015.

[9] R.D. Mosteller. Simplified calculation of body-surface area. *The New England journal of medicine*, 317(17):1098, 1987.

[10] KENNETH M HALPRIN. Epidermal "turnover time"—a re-examination. *British Journal of Dermatology*, 86(1):14–19, 1972.

[11] Miranda A Farage, Kenneth W Miller, Peter Elsner, and Howard I Maibach. Characteristics of the aging skin. *Advances in wound care*, 2(1):5–10, 2013.

[12] D. Sliney. Balancing the Risk of Eye Irritation from UV-C with Infection from Bioaerosols. *Photochemistry and Photobiology*, 89(4):770–776, 7 2013.

[13] CIE. CIE Standard S009/E-2002 Photobiological Safety of Lamps and Lamp Systems. 2002.

[14] M.M. Zempila, J.H.G.M. van Geffen, M. Taylor, I. Fountoulakis, M.E. Koukouli, M. van Weele, R.J. van der A, A. Bais, C. Meleti, and D. Balis. TEMIS UV product validation using NILU-UV ground-based measurements in Thessaloniki, Greece. *Atmospheric Chemistry and Physics*, 17(11):7157–7174, 6 2017.

[15] A.R. Webb, H. Slaper, P. Koepke, and A.W. Schmalwieser. Know Your Standard: Clarifying the CIE Erythema Action Spectrum. *Photochemistry and Photobiology*, 87(2):483–486, 3 2011.

[16] R. Bouillon, J. Eisman, M. Garabedian, M. Holick, J. Kleinschmidt, T. Suda, I. Terenetskaya, and A. Webb. Action spectrum for the production of previtamin D3 in human skin. *UDC*, 612:481–486, 2006.

[17] R.B. Setlow. The wavelengths in sunlight effective in producing skin cancer: a theoretical analysis. *Proceedings of the National Academy of Sciences*, 71(9):3363–3366, 1974.

[18] T.B. Fitzpatrick and M.A. Pathak. Part IV: Basic Considerations of the Psoralens: Historical Aspects of Methoxsalen and Other Furocoumarins. *Journal of Investigative Dermatology*, 32(2):229–231, 2 1959.

[19] M.M. Nathaniel. Benefits of Sunlight: A Bright Spot for Human Health. *Environmental Health Perspectives*, 116(4):A160–A167, 4 2008.

[20] M. Mowbray, S. McLintock, R. Weerakoon, N. Lomatschinsky, S. Jones, A. G. Rossi, and R.B. Weller. Enzyme-independent NO stores in human skin: Quantification and influence of UV radiation. *Journal of Investigative Dermatology*, 129(4):834–842, 4 2009.

[21] Asta Juzeniene and Johan Moan. Beneficial effects of uv radiation other than via vitamin d production. *Dermato-endocrinology*, 4(2):109–117, 2012.

[22] D. Welch, M. Buonanno, V. Grilj, I. Shuryak, C. Crickmore, A.W. B., G. Randers-Pehrson, G.W. Johnson, and D.J. Brenner. Far-UVC light: A new tool to control the spread of airborne-mediated microbial diseases. *Scientific Reports*, 8(1), 12 2018.

[23] Transport theory and the diffusion equation. In I.J. Bigio and S. Fantini, editors, *Quantitative Biomedical Optics: Theory, Methods, and Applications*, Cambridge Texts in Biomedical Engineering, pages 277–316. Cambridge University Press, Cambridge, 2016.

[24] N. Metropolis. The Beginning of the Monte Carlo Method. *Los Alamos Science*, 15:125–130, 1987.

[25] S. Agostinelli, J. Allison, K. Amako, J. Apostolakis, H. Araujo, P. Arce, M. Asai, D. Axen, S. Banerjee, G. Barrand, F. Behner, L. Bellagamba, J. Boudreau, L. Broglia, A. Brunengo,

H. Burkhardt, S. Chauvie, J. Chuma, R. Chytracek, G. Cooperman, G. Cosmo, P. Degtyarenko, A. Dell'Acqua, G. Depaola, D. Dietrich, R. Enami, A. Feliciello, C. Ferguson, H. Fesefeldt, G. Folger, F. Foppiano, A. Forti, S. Garelli, S. Giani, R. Giannitrapani, D. Gibin, J.J. Gómez Cadenas, I. González, G. Gracia Abril, G. Greeniaus, W. Greiner, V. Grichine, A. Grossheim, S. Guatelli, P. Gumplinger, R. Hamatsu, K. Hashimoto, H. Hasui, A. Heikkinen, A. Howard, V. Ivanchenko, A. Johnson, F.W. Jones, J. Kallenbach, N. Kanaya, M. Kawabata, Y. Kawabata, M. Kawaguti, S. Kelner, P. Kent, A. Kimura, T. Kodama, R. Kokoulin, M. Kossov, H. Kurashige, E. Lamanna, T. Lampén, V. Lara, V. Lefebure, F. Lei, M. Liendl, W. Lockman, F. Longo, S. Magni, M. Maire, E. Medernach, K. Minamimoto, P. Mora de Freitas, Y. Morita, K. Murakami, M. Nagamatu, R. Nartallo, P. Nieminen, T. Nishimura, K. Ohtsubo, M. Okamura, S. O'Neale, Y. Oohata, K. Paech, J. Perl, A. Pfeiffer, M.G. Pia, F. Ranjard, A. Rybin, S. Sadilov, E. Di Salvo, G. Santin, T. Sasaki, N. Savvas, Y. Sawada, S. Scherer, S. Sei, V. Sirotenko, D. Smith, N. Starkov, H. Stoecker, J. Sulkimo, M. Takahata, S. Tanaka, E. Tcherniaev, E. Safai Tehrani, M. Tropeano, P. Truscott, H. Uno, L. Urban, P. Urban, M. Verderi, A. Walkden, W. Wander, H. Weber, J.P. Wellisch, T. Wenaus, D.C. Williams, D. Wright, T. Yamada, H. Yoshida, and D. Zschiesche. Geant4—a simulation toolkit. *"Nuclear Instruments and Methods in Physics Research Section A: Accelerators, Spectrometers, Detectors and Associated Equipment"*, 506(3):250 – 303, 2003.

[26] B.C. Wilson and G. Adam. A Monte Carlo model for the absorption and flux distributions of light in tissue. *Medical Physics*, 10(6):824–830, 11 1983.

[27] S. Wang, J. Zhao, H. Lui, Q. He, J. Bai, and H. Zeng. Monte Carlo simulation of in vivo Raman spectral measurements of human skin with a multi-layered tissue optical model. *Journal of Biophotonics*, 7(9):703–712, 2014.

[28] D.L. McLeish. *Monte Carlo simulation and finance*, volume 276. John Wiley & Sons, 2011.

[29] N. Silver. FiveThirtyEight, https://data.fivethirtyeight.com/ (accessed February 2020).

[30] R. Verity, L.C. Okell, I. Dorigatti, P. Winskill, C. Whittaker, N. Imai, G. Cuomo-Dannenburg, H. Thompson, P.G.T. Walker, H. Fu, A. Dighe, J.T. Griffin, M. Baguelin, S. Bhatia, A. Boonyasiri, A. Cori, Z. Cucunubá, R. FitzJohn, K. Gaythorpe, W. Green, A. Hamlet, W. Hinsley, D. Laydon, G. Nedjati-Gilani, S. Riley, S. van Elsland, E. Volz, H. Wang, Y. Wang, X. Xi, C.A. Donnelly, A.C. Ghani, and N.M. Ferguson. Estimates of the severity of coronavirus disease 2019: a model-based analysis. *The Lancet. Infectious diseases*, 6 2020.

[31] L. Wang, S.L. Jacques, and L. Zheng. MCML_Monte Carlo modeling of light transport in multi layered tissues. *Computer Methods and Programs in Biomedicine*, 47(2):131–146, 1995.

[32] I.R.M. Barnard, P. Tierney, C.L. Campbell, L. McMillan, H. Moseley, E. Eadie, C.T.A. Brown, and K. Wood. Quantifying Direct DNA Damage in the Basal Layer of Skin Exposed to UV Radiation from Sunbeds. *Photochemistry and Photobiology*.

[33] I.R.M. Barnard, E. Eadie, L. McMillan, H. Moseley, T. Brown, K. Wood, and R. Dawe. Could psoralen plus ultraviolet A1 ("PUVA1") work? Depth penetration achieved by phototherapy lamps. *British Journal of Dermatology*, 9 2019.

[34] S.L. Jacques, C.A. Alter, and A.S. Prahl. Angular dependence of HeNe laser light scattering by human dermis. *Lasers Life Sci*, 1(4):309–333, 1987.

[35] D.A. Boas, J.P. Culver, J.J. Stott, and A.K. Dunn. Three dimensional Monte Carlo code for photon migration through complex heterogeneous media including the adult human head. *Optics Express*, 10(3):159, 2 2002.

[36] K. Wood. Lecture Notes, Monte Carlo Radiation Transfer Techniques, School of Physics & Astronomy (University of St Andrews), available at http://www-star.st-and.ac.uk/ kw25/teaching/mcrt/mcrt.html (accessed 2016-2020), 2015.

[37] W.H. Press, S.A. Teukolsky, B.P. Flannery, and W.T. Vetterling. *Numerical recipes in Fortran 77: volume 1, Fortran numerical recipes: the art of scientific computing*. Cambridge University Press, 1992.

[38] M.J.C. Van Gemert, S.L. Jacques, H.J.C.M. Sterenborg, and W.M. Star. Skin Optics. *IEEE Transactions on Biomedical Emgineering*, 36(12):1146–1154, 1989.

[39] L.V. Wang and H. Wu. *Biomedical optics: principles and imaging*. John Wiley & Sons, 2012.

[40] L.B. Lucy. Computing radiative equilibria with Monte Carlo techniques. *Astron. Astrophys*, 344:282–288, 1999.

[41] S.L. Jacques, R. Joseph, and G. Gofstein. How photobleaching affects dosimetry and fluorescence monitoring of PDT in turbid media. *SPIE Optical Methods for Tumor Treatment and Detection*, 1881:168, 1993.

[42] A.E. Karsten and J.E. Smit. Modeling and verification of melanin concentration on human skin type. *Photochemistry and Photobiology*, 88(2):469–474, 3 2012.

[43] T.B. Fitzpatrick. The validity and practicality of sun-reactive skin types I through VI. *Archives of Dermatology*, 124(6):869–871, 1988.

[44] J. Sandby-Møller, T. Poulsen, and H.C. Wulf. Epidermal Thickness at Different Body Sites: Relationship to Age, Gender, Pigmentation, Blood Content, Skin Type and Smoking Habits. *Acta Dermato-Venereologica*, 83(6):410–413, 2003.

[45] S.L. Jacques. Skin Optics, https://omlc.org/news/jan98/skinoptics.html (accessed 2016-2018), 1998.

[46] A.N. Bashkatov, E.A. Genina, and V.V. Tuchin. Optical properties of skin, subcutaneous, and muscle tissues: A review. *Journal of Innovative Optical Health Sciences*, 4(1):9–38, 1 2011.

[47] T. Lister, P.A. Wright, and P.H. Chappell. Optical properties of human skin. *Journal of Biomedical Optics*, 17(9):0909011, 9 2012.

[48] H. Ding, J.Q. Lu, W.A. Wooden, P.J. Kragel, and X.H. Hu. Refractive indices of human skin tissues at eight wavelengths and estimated dispersion relations between 300 and 1600 nm. *Physics in Medicine and Biology*, 51(6):1479–1489, 3 2006.

[49] U.B. Jensen, S. Lowell, and F.M. Watt. The spatial relationship between stem cells and their progeny in the basal layer of human epidermis: a new view based on whole-mount labelling and lineage analysis. *Development*, 126(11):2409–2418, 1999.

[50] D.M. Owens and F.M. Watt. Contribution of stem cells and differentiated cells to epidermal tumours. *Nature Reviews Cancer*, 3(6):444–451, 6 2003.

[51] M. Brenner and V.J. Hearing. The Protective Role of Melanin Against UV Damage in Human Skin. *Photochem. Photobio.*, 84:539–549, 2007.

[52] S. Premi, S. Wallisch, C.M. Mano, A.B. Weiner, A. Bacchiocchi, K. Wakamatsu, E.J.H. Bechara, R. Halaban, T. Douki, and D.E. Brash. Chemiexcitation of melanin derivatives induces DNA photoproducts long after UV exposure. *Science*, 247(6224):842–847, 2015.

[53] J.A. Iglesias-Guitian, C. Aliaga, A. Jarabo, and D. Gutierrez. A Biophysically-Based Model of the Optical Properties of Skin Aging. In *Computer Graphics Forum*, volume 34, pages 45–55. John Wiley & Sons, Ltd, 5 2015.

[54] P. Tierney, J. Ferguson, S. Ibbotson, R. Dawe, E. Eadie, and H. Moseley. Nine out of 10 sunbeds in England emit ultraviolet radiation levels that exceed current safety limits. *British Journal of Dermatology*, 168(3):602–608, 3 2013.

[55] Scientific Committee on Emerging and European Commission Newly Identified Health Risks. Preliminary Opinion on Biological Effects of Ultraviolet Radiation Relevant to Health with Particular Reference to Sun Beds for Cosmetic Purposes, retrieved from https://ec.europa.eu/health/scientific_committees/scheer/docs/scheer_o_003.pdf. *European Commission Brussels, Belgium*, 2015.

[56] P. Tierney, F.R. de Gruijl, S. Ibbotson, and H. Moseley. Predicted increased risk of squamous cell carcinoma induction associated with sunbed exposure habits. *British Journal of Dermatology*, 173(1):201–208, 7 2015.

[57] H. Oliver, J. Ferguson, and H. Moseley. Quantitative risk assessment of sunbeds: Impact of new high power lamps. *British Journal of Dermatology*, 157(2):350–356, 8 2007.

[58] A. Swerdlow, J.S.C. English, R.M. Mackie, C.J. O'Doherty, J.A.A. Hunter, J. Clark, and D.J. Hole. Fluorescent lights, ultraviolet lamps, and risk of cutaneous melanoma. *British Medical Journal*, 297(1), 9 1988.

[59] S.D. Walter, L.D. Marrett, L. From, C. Hertzman, H.S. Shannon, and P. Roy. The association of cutaneous malignant melanoma with the use of sunbeds and sunlamps. *American Journal of Epidemiology*, 131(2):232–243, 1990.

[60] J. Westerdahl, H. Olsson, A. Masback, C. Ingvar, N. Jonsson, L. Brandt, P.E. Jonsson, and T. Moller. Use of Sunbeds or Sunlamps and Malignant Melanoma in Southern Sweden. *American Journal of Epidemiology*, 140(8), 1994.

[61] A. Østerlind, M.A. Tucker, B.J. Stone, and O.M. Jensen. The Danish case-control study of cutaneous malignant melanoma II. Importance of UV-light exposure. *Int. J. Cancer*, 42:319–324, 1988.

[62] R.M. Mackie, T. Freudenberger, and T.C. Aitchison. Preventive Medicine: Personal risk-factor chart for cutaneous melanoma. *The Lancet*, pages 487–490, 8 1989.

[63] M. Boniol, P. Autier, P. Boyle, and S. Gandini. Cutaneous melanoma attributable to sunbed use: systematic review and meta-analysis. *BMJ (Clinical research ed.)*, 345:e4757, 7 2012.

[64] J.L.M Hawk. Sunbeds. *Radiation Protection Dosimetry*, 91(1-3):143–145, 9 2000.

[65] P. Autier. Perspectives in melanoma prevention: The case of sunbeds. *European Journal of Cancer*, 2004.

[66] Z. Amir, A. Wright, E.E. Kernohan, and G. Hart. Attitudes, beliefs and behaviour regarding the use of sunbeds amongst healthcare workers in Bradford. *European journal of cancer care*, 9(2):76—79, 6 2000.

[67] H. Moseley, M. Davidson, and J. Ferguson. A hazard assessment of artificial tanning units. *Photodermatology Photoimmunology and Photomedicine*, 14(2):79–87, 1998.

[68] Sunbed Association https://www.sunbedassociation.org.uk/UV_Tanning/FAQs.aspx#safe (accessed February 2020).

[69] D.E. Brash. Roles of the transcription factor p53 in keratinocyte carcinomas. *British Journal of Dermatology*, 154(Suppl.1):9–10, 2006.

[70] S. Mouret, C. Baudouin, M. Charveron, A. Favier, J. Cadet, and T. Douki. Cyclobutane pyrimidine dimers are predominant DNA lesions in whole human skin exposed to UVA radiation. *PNAS*, 103(37):13765–13770, 2006.

[71] J. D'Orazio, S. Jarrett, A. Amaro-Ortiz, and T. Scott. UV radiation and the skin. *International Journal of Molecular Sciences*, 14:12222–12248, 2013.

[72] G.J. Delinasios, M. Karbaschi, M.S. Cooke, and A.R. Young. Vitamin E inhibits the UVAI induction of "light" and "dark" cyclobutane pyrimidine dimers, and oxidatively generated DNA damage, in keratinocytes. *Scientific Reports*, 8(1):423, 12 2018.

[73] D.S. Goodsell. The molecular perspective: ultraviolet light and pyrimidine dimers. *The oncologist*, 6(3):298–9, 6 2001.

[74] T. Lindahl and R.D. Wood. Quality Control by DNA Repair. *Science*, 286(5446):1897–1905, 12 1999.

[75] F.J. Geske, A.C. Nelson, R. Lieberman, R. Strange, T. Sun, and L.E. Gerschenson. DNA repair is activated in early stages of p53-induced apoptosis. *Call Death and Differentiation*, 7:393–401, 2000.

[76] C.A. Chadwick, C.S. Potten, O. Nikaido, T. Matsunaga, C. Proby, and A.R. Young. The detection of cyclobutane thymine dimers, (6-4) photolesions and the Dewar photoisomers in sections of UV-irradiated human skin using specific antibodies, and the demonstration of depth penetration effects. *Journal of Photochemistry and Photobiology, B: Biology*, 1995.

[77] R.E. Bird and C. Riordan. Simple Solar Spectral Model for Direct and Diffuse Irradiance on Horizontal and Tilted Planes at Earth's Surface for Cloudless Atmospheres. *Journal of Climate and Applied Meteorology*, 25:87–97, 1986.

[78] Bird and Hulstrom's Solar Irradiance Model http://www.instesre.org/Solar/BirdModelNew.htm (accessed 2016-2020).

[79] S. Mouret, C. Philippe, J. Gracia-Chantegrel, A. Banyasz, S. Karpati, D. Markovitsi, and T. Douki. UVA-induced cyclobutane pyrimidine dimers in DNA: A direct photochemical mechanism? *Organic and Biomolecular Chemistry*, 8(7):1706–1711, 2010.

[80] B. Mohlenhoff, M. Romeo, M. Diem, and B.R. Wood. Mie-type scattering and non-Beer-Lambert absorption behavior of human cells in infrared microspectroscopy. *Biophysical Journal*, 88(5):3635–3640, 2005.

[81] Fiona M Watt and Howard Green. Involucrin synthesis is correlated with cell size in human epidermal cultures. *The Journal of cell biology*, 90(3):738–742, 1981.

[82] A. Banyasz, T. Douki, R. Improta, T. Gustavsson, D. Onidas, I. Vayá, M. Perron, and D. Markovitsi. Electronic excited states responsible for dimer formation upon UV absorption directly by thymine strands: Joint experimental and theoretical study. *Journal of the American Chemical Society*, 134(36):14834–14845, 9 2012.

[83] H. Ikehata, T. Mori, Y. Kamei, T. Douki, J. Cadet, and M. Yamamoto. Wavelength- and Tissue-dependent Variations in the Mutagenicity of Cyclobutane Pyrimidine Dimers in Mouse Skin. *Photochemistry and Photobiology*, 96(1):94–104, 1 2020.

[84] A. Woollons, C. Kipp, A.R. Young, C. Petit-Frère, C.F. Arlett, M.H.L. Green, and P.H. Clingen. The 0.8% ultraviolet B content of an ultraviolet A sunlamp induces 75% of cyclobutane pyrimidine dimers in human keratinocytes in vitro. *British Journal of Dermatology*, 1999.

[85] A.R. Young, J. Narbutt, G.I. Harrison, K.P. Lawrence, M. Bell, C. O'Connor, P. Olson, K. Grys, K.A. Baczynska, M. Rogowski-Tylman, H.C. Wulf, A. Lesiak, and P.A. Philipsen. Optimal sunscreen use, during a sun holiday with a very high ultraviolet index, allows vitamin D synthesis without sunburn. *British Journal of Dermatology*, page bjd.17888, 5 2019.

[86] R.M Halder and S. Bridgeman-Shah. Skin cancer in african americans. *Cancer*, 75(S2):667–673, 1995.

[87] M. Norval, P. Kellett, and C.Y. Wright. The incidence and body site of skin cancers in the population groups of South Africa. *Photodermatology, photoimmunology & photomedicine*, 30(5):262–265, 2014.

[88] T. Cestari and K. Buster. Photoprotection in specific populations: Children and people of color. *Journal of the American Academy of Dermatology*, 76(3):S110–S121, 2017.

[89] D. Fajuyigbe and A.R. Young. The impact of skin colour on human photobiological responses. *Pigment Cell and Melanoma Research*, 29(6):607–618, 11 2016.

[90] D. Fajuyigbe, S.M. Lwin, B.L. Diffey, R. Baker, D.J. Tobin, R.P.E. Sarkany, and A.R. Young. Melanin distribution in human epidermis affords localized protection against DNA photodamage and concurs with skin cancer incidence difference in extreme phototypes. *The FASEB Journal*, 32, 2018.

[91] S. Del Bino, S. Ito, J. Sok, Y. Nakanishi, P. Bastien, K. Wakamatsu, and F. Bernerd. Chemical analysis of constitutive pigmentation of human epidermis reveals constant eumelanin to pheomelanin ratio. *Pigment Cell and Melanoma Research*, 28(6):707–717, 11 2015.

[92] U. Osterwalder and B. Herzog. The long way towards the ideal sunscreen - Where we stand and what still needs to be done. *Photochemical and Photobiological Sciences*, 9:470, 2010.

[93] L. Ferrero, M. Pissavini, S. Marguerie, and L. Zastrow. Sunscreen in vitro spectroscopy: application to UVA protection assessment and correlation with in vivo persistent pigment darkening. *International Journal of Cosmetic Science*, 24(2):63–70, 2 2002.

[94] Boots the Chemist Ltd. The revised guidelines to the practical measurement of UVA/UVB ratios according to the Boots star rating system, accessed via https://cdnmedia.eurofins.com/apac/media/601375/boots-star.pdf (and other publications citing same guidelines), 2008.

[95] International Organization for Standardization. Cosmetics- Sun protection test methods- In vivo determination of the sun protection factor (SPF) (ISO 24444:2019), retrieved from https://www.iso.org/standard/72250.html. Technical report, 2019.

[96] A. Chardon, I. Cretois, and C. Hourseau. Skin colour typology and suntanning pathways. *International Journal of Cosmetic Science*, 13(4):191–208, 8 1991.

[97] B. Herzog and U. Osterwalder. Simulation of sunscreen performance. In *Pure and Applied Chemistry*, volume 87, pages 937–951, 2015.

[98] B. Diffey and U. Osterwalder. Labelled sunscreen SPFs may overestimate protection in natural sunlight. *Photochemical & Photobiological Sciences*, 16(10):1519–1523, 2017.

[99] A.R. Young, J. Boles, B. Herzog, U. Osterwalder, and W. Baschong. A Sunscreen's labeled sun protection factor may overestimate protection at temperate latitudes: A human in vivo study. *Journal of Investigative Dermatology*, 130(10):2457–2462, 2010.

[100] R.M. Sayre, J. Stanfield, A.J. Bush, and D.L. Lott. Sunscreen standards tested with differently filtered solar simulators. *Photodermatol Photoimmunol Photomed*, 17:278–283, 2001.

[101] CIE International Commission on Illumination. Erythema reference action spectrum and standard erythema dose. Vienna, Austria, 1998.

[102] L. Ferrero, M. Pissavini, and O. Doucet. How a calculated model of sunscreen film geometry can explain in vitro and in vivo SPF variation. *Photochemical and Photobiological Sciences*, 9:540, 2010.

[103] B. Herzog, A. Schultheiss, and J. Giesinger. On the Validity of Beer–Lambert Law and its Significance for Sunscreens. *Photochemistry and Photobiology*, 94(2):384–389, 3 2018.

[104] M. Sohn, A. Hêche, B. Herzog, and G. Imanidis. Film thickness frequency distribution of different vehicles determines sunscreen efficacy. *Journal of Biomedical Optics*, 19(11), 2014.

[105] J.J. O'Neill. Effect of Film Irregularities on Sunscreen Efficacy. *Journal of Pharmaceutical Sciences*, 73(7):888–891, 7 1984.

[106] S. Brown and B.L. Diffey. The effect of applied thickness on sunscreen protection: in vivo and in vitro studies. *Photochemistry and Photobiology*, 44(4):509–513, 10 1986.

[107] BASF Care Creations Sunscreen Simulator. https://www.sunscreensimulator.basf.com/ Sunscreen_Simulator/login (accessed 2018-2020).

[108] DSM's Sunscreen Optimizer. https://www.sunscreen-optimizer.com/index.html.

[109] Mike Brown. EU Anex VI & FDA UV Filter History (personal communication), 2017.

[110] A.R. Young, J. Greenaway, G.I. Harrison, K.P. Lawrence, R. Sarkany, T. Douki, F. Boyer, G. Josse, E. Questel, C. Monteil, and A.B. Rossi. Sub-optimal application of a high SPF sunscreen prevents epidermal DNA damage in vivo. *Acta Dermato-Venereologica*, 98(9):880–887, 2018.

[111] M.A. Lowes, M. Suárez-Fariñas, and J.G. Krueger. Immunology of psoriasis. *Annual Review of Immunology*, 32:227–255, 2014.

[112] R. Roelandts. The history of phototherapy: Something new under the sun? *Journal of the American Academy of Dermatology*, 46(6):926–930, 6 2002.

[113] H. Hönigsmann. History of phototherapy in dermatology. *Photochemical and Photobiological Sciences*, 12(1):16–21, 2013.

[114] H. Cameron, S. Yule, H. Moseley, R.S. Dawe, and J. Ferguson. Taking treatment to the patient: development of a home TL-01 ultraviolet B phototherapy service. *British Journal of Dermatology*, 147(5):957–965, 11 2002.

[115] H. Cameron, S. Yule, R.S. Dawe, S.H. Ibbotson, H. Moseley, and J. Ferguson. Review of an established UK home phototherapy service 1998–2011: improving access to a cost-effective treatment for chronic skin disease. *Public Health*, 128(4):317–324, 2014.

[116] British Association of Dermatologists. Phototherapy: Patient Information Leaflet, 2018.

[117] L.A. Schneider, R. Hinrichs, and K. Scharffetter-Kochanek. Phototherapy and photochemotherapy. *Clinics in dermatology*, 26.5:464–476, 1 2008.

[118] R.M.R. Hearn, A.C. Kerr, K.F. Rahim, J. Ferguson, and R.S. Dawe. Incidence of skin cancers in 3867 patients treated with narrow-band ultraviolet B phototherapy. *British Journal of Dermatology*, 159(4):931–935, 10 2008.

[119] H. Hönigsmann. Phototherapy for psoriasis. *Clinical and Experimental Dermatology*, 26(4):343–350, 2001.

[120] M. Kallassy, N. Martel, O. Damour, H. Yamasaki, and H. Nakazawa. Growth Arrest of Immortalized Human Keratinocytes and Suppression of Telomerase Activity by p21 WAF1 Gene Expression. *Molecular Carcinogenisis*, 21:26–36, 1998.

[121] S. Beissert and T. Schwarz. Mechanisms involved in ultraviolet light-induced immunosuppression. In *Journal of Investigative Dermatology Symposium Proceedings*, 1999.

[122] S.H. Ibbotson. A perspective on the use of NB-UVB Phototherapy vs. PUVA photochemotherapy. *Frontiers in Medicine*, 5, 2018.

[123] S. Abdallah, M. Salem, M. Ahmad, E.T. Barakat, C. Mohsen, Z.M. Morcos, and A.A. Ali. Bath psoralen + ultraviolet A photochemotherapy vs. narrow band-ultraviolet B in psoriasis: a comparison of clinical outcome and effect on circulating T-helper and T-suppressor/cytotoxic cells Conflicts of interest. *Photodermatology,Photoimmunology & Photomedicine*, 26:235–242.

[124] A.C. Kerr, J. Ferguson, S.K. Attili, P.E. Beattie, A.J. Coleman, R.S. Dawe, B. Eberlein, V. Goulden, S.H. Ibbotson, H.DuP. Menage, H. Moseley, L. Novakovic, S.L. Walker, J.A. Woods, A.R. Young, and R.P.E. Sarkany. Ultraviolet A1 phototherapy: A British Photodermatology Group workshop report. *Clinical and Experimental Dermatology*, 37(3):219–226, 4 2012.

[125] N.R. York, H.T. Jacobe, and H. Jacobe. UVA1 phototherapy: a review of mechanism and therapeutic application. *Clinical Dermatology*, 49:623–630, 2010.

[126] A. Woźniacka, K. Malinowska, and A. Sysa-Jędrzejowska. UVA1 phototherapy in dermatological treatment. *Advances in Dermatology and Allergology XXVIII*, 1:53–58, 2011.

[127] A. Robinson, A.S. Van Voorhees, S. Hsu, N.J. Korman, M.G. Lebwohl, B.F. Bebo, and R.E. Kalb. ATreatment of pustular psoriasis: From the medical board of the National Psoriasis Foundation. *Journal of the American Academy of Dermatology*, pages 279–288, 2012.

[128] L. Su, X. Xu, L. Tang, N. Yu, and Y. Ding. UVA1 phototherapy in the treatment of palmoplantar pustulosis: a pilot prospective study. *Lasers in Medical Science*, 31(8):1641–1643, 11 2016.

[129] T. C. Ling, T.H. Clayton, J. Crawley, L.S. Exton, V. Goulden, S. Ibbotson, K. McKenna, M.F. Mohd Mustapa, L.E. Rhodes, R. Sarkany, and R.S. Dawe. British Association of Dermatologists and British Photodermatology Group guidelines for the safe and effective use of psoralen-ultraviolet A therapy 2015. *British Journal of Dermatology*, 174(1):24–55, 1 2016.

[130] E. Yeargers and L. Augenstein. Absorption and emission spectra of psoralen and 8-methoxypsoralen in powders and solutions. *The Journal of investigative dermatology*, 44(3):181–187, 1965.

[131] F.P. Gasparro, P. Gattolin, G.A. Olack, L.I. Deckelbaum, and B.E. Sumpio. The excitation of 8-methoxypsoralen with visible light reversed phase HPLC quantitation of monoadducts and cross-links. *Photochemistry and Photobiology*, 57(6):1007–1010, 1993.

[132] M. Grundmann-Kollmann, M. Podda, L. Bräutigam, K. Hardt-Weinelt, R.J. Ludwig, G. Geisslinger, R. Kaufmann, and I. Tegeder. Spatial distribution of 8-methoxypsoralen penetration into human skin after systemic or topical administration. *British Journal of Clinical Pharmacology*, 54(5):535–539, 2002.

[133] S.S. Sastry, B.M. Ross, and A. P'arraga. Cross-linking of DNA-binding Proteins to DNA with Psoralen and Psoralen Furan-side Monoadducts. *The Journal of Biological Chemistry*, 272(6):3715–3723, 1997.

[134] T.J. Walsh, V. Petraitis, and W.J. Kowalski. 2020 COVID-19 Coronavirus Ultraviolet Susceptibility. Technical report, 2020.

[135] R.B. Setlow, E. Grist, K. Thompson, and A.D. Woodhead. Wavelengths effective in induction of malignant melanoma. *Proceedings of the National Academy of Sciences*, 90(14):6666–6670, 1993.

[136] D. Balasubramanian. Ultraviolet radiation and cataract. *Journal of Ocular Pharmacology and Therapeutics*, 16(3):285–297, 2000.

[137] A. Trevisan, S. Piovesan, A. Leonardi, M. Bertocco, P. Nicolosi, Maria G. Pelizzo, and A. Angelini. Unusual high exposure to ultraviolet-c radiation. *Photochemistry and photobiology*, 82(4):1077–1079, 2006.

[138] S. Zaffina, V. Camisa, M. Lembo, M.G. Vinci, M.R.and Tucci, M. Borra, and V. Napolitano, A.and Cannatà. Accidental exposure to uv radiation produced by germicidal lamp: case report and risk assessment. *Photochemistry and photobiology*, 88(4):1001–1004, 2012.

[139] J.A. Woods, A. Evans, P.D. Forbes, P.J. Coates, J. Gardner, R.M. Valentine, S.H. Ibbotson, J. Ferguson, C. Fricker, and H. Moseley. The effect of 222-nm UVC phototesting on healthy volunteer skin: A pilot study. *Photodermatology Photoimmunology and Photomedicine*, 31(3):159–166, 5 2015.

[140] M. Buonanno, G. Randers-Pehrson, A.W. Bigelow, S. Trivedi, Franklin D. Lowy, H.M. Spotnitz, S.M. Hammer, and D.J. Brenner. 207-nm UV Light - A Promising Tool for Safe Low-Cost Reduction of Surgical Site Infections. I: In Vitro Studies. *PLoS ONE*, 8(10), 10 2013.

[141] S. Kreusch, S. Schwedler, B. Tautkus, G.A. Cumme, and A. Horn. UV measurements in microplates suitable for high-throughput protein determination. *Analytical Biochemistry*, 313:208–215, 2003.

[142] T. Matsunaga, K. Hieda, and O. Nikaido. Wavelength dependent formation of thymine monochromatic ultraviolet light ranging from 150 to 365 nm. Technical Report 3, 1991.

[143] M. Buonanno, B. Ponnaiya, D. Welch, M. Stanislauskas, G. Randers-Pehrson, L. Smilenov, F.D. Lowy, D.M. Owens, and D.J. Brenner. Germicidal Efficacy and Mammalian Skin Safety of 222-nm UV Light. *Radiation Research*, 187(4):493–501, 4 2017.

[144] M. Buonanno, M. Stanislauskas, B. Ponnaiya, A.W. Bigelow, G. Randers-Pehrson, Y. Xu, I. Shuryak, L. Smilenov, D.M. Owens, and D.J. Brenner. 207-nm UV light - A promising tool for safe low-cost reduction of surgical site infections. II: In-vivo safety studies. *PLoS ONE*, 11(6), 6 2016.

[145] Z.W. Lipsky and G.K. German. Ultraviolet light degrades the mechanical and structural properties of human stratum corneum. *Journal of the Mechanical Behavior of Biomedical Materials*, 100, 12 2019.

[146] Scientific Committee on Consumer Products SCCP. Opinion on Biological effects of ultraviolet radiation relevant to health with particular reference to sunbeds for cosmetic purposes. Technical report, 2006.

[147] Highland Council. Ultra-violet sunbed Sun Tanning Conditions of Licence (https://www.highland.gov.uk/directory_record/738761/ultra-violet_sunbed), 2019.

[148] Gigahertz Optik. X1-4 Erythema Broadband Radiometer for Hazard Testing Sun Tanning Beds, https://www.gigahertz-optik.de/en-us/product/X14 (accessed 2017-2020).

[149] K.P. Radack, M.E. Farhangian, K.L. Anderson, and S.R. Feldman. A Review of the Use of Tanning Beds as a Dermatological Treatment. *Dermatology and Therapy*, 5(1):37–51, 3 2015.